

# 1 Comparative assessment of TROPOMI and OMI formaldehyde 2 observations and validation against MAX-DOAS network column 3 measurements

4 Isabelle De Smedt<sup>1</sup>, Gaia Pinardi<sup>1</sup>, Corinne Vigouroux<sup>1</sup>, Steven Compernelle<sup>1</sup>, Alkis Bais<sup>2</sup>, Nuria  
5 Benavent<sup>3</sup>, Folkert Boersma<sup>4,5</sup>, Ka-Lok Chan<sup>6</sup>, Sebastian Donner<sup>7</sup>, Kai-Uwe Eichmann<sup>8</sup>, Pascal  
6 Hedelt<sup>6</sup>, François Hendrick<sup>1</sup>, Hitoshi Irie<sup>9</sup>, Vinod Kumar<sup>7</sup>, Jean-Christopher Lambert<sup>1</sup>, Bavo  
7 Langerock<sup>1</sup>, Christophe Lerot<sup>1</sup>, Cheng Liu<sup>10</sup>, Diego Loyola<sup>6</sup>, Ankie Pitters<sup>4</sup>, Andreas Richter<sup>8</sup>,  
8 Claudia Rivera Cárdenas<sup>11</sup>, Fabian Romahn<sup>6</sup>, Robert George Ryan<sup>12,13</sup>, Vinayak Sinha<sup>14</sup>, Nicolas  
9 Theys<sup>1</sup>, Jonas Vlietinck<sup>1</sup>, Thomas Wagner<sup>7</sup>, Ting Wang<sup>15</sup>, Huan Yu<sup>1</sup>, Michel Van Roozendael<sup>1</sup>.

10 *Correspondence to:* Isabelle De Smedt ([isabelle.desmedt@aeronomie.be](mailto:isabelle.desmedt@aeronomie.be))

- 11 1. Royal Belgian Institute for Space Aeronomy (BIRA-IASB), Ringlaan 3, 1180 Uccle, Belgium.  
12 2. Laboratory of Atmospheric Physics, Aristotle University of Thessaloniki (AUTH), Thessaloniki, Greece.  
13 3. Department of Atmospheric Chemistry and Climate, Institute of Physical Chemistry Rocasolano (CSIC), Madrid,  
14 Spain.  
15 4. Royal Netherlands Meteorological Institute (KNMI), De Bilt, the Netherlands.  
16 5. Meteorology and Air Quality group, Wageningen University, the Netherlands.  
17 6. Institut für Methodik der Fernerkundung (IMF), Deutsches Zentrum für Luft und Raumfahrt (DLR),  
18 Oberpfaffenhofen, Germany.  
19 7. Max-Planck-Institut für Chemie (MPI-C), Mainz, Germany.  
20 8. Institute of Environmental Physics, University of Bremen (IUP-B), Bremen, Germany.  
21 9. Center for Environmental Remote Sensing, Chiba University (Chiba U), Chiba, Japan  
22 10. Department of Precision Machinery and Precision Instrumentation, University of Science and Technology of  
23 China, Hefei, China.  
24 11. Centro de Ciencias de la Atmósfera, Universidad Nacional Autónoma de México (UNAM), Mexico City, Mexico  
25 12. School of Earth Sciences, The University of Melbourne, Melbourne, Australia  
26 13. ARC Centre of Excellence for Climate System Science, Sydney, Australia  
27 14. Department of Earth and Environmental Sciences, Indian Institute of Science Education and Research (IISER),  
28 Mohali, India  
29 15. Institute of Atmospheric Physics, Chinese Academy of Sciences (CAS), Beijing, China  
30

31 **Abstract.** The TROPOspheric Monitoring Instrument (TROPOMI), launched in October 2017 on board the Sentinel-  
32 5 Precursor (S5P) satellite, monitors the composition of the Earth's atmosphere at an unprecedented horizontal  
33 resolution as fine as  $3.5 \times 5.5 \text{ km}^2$ . This paper assesses the performances of the TROPOMI formaldehyde (HCHO)  
34 operational product compared to its predecessor, the OMI HCHO QA4ECV product, at different spatial and temporal  
35 scales. The parallel development of the two algorithms favored the consistency of the products, which facilitates the  
36 production of long-term combined time series. The main difference between the two satellite products is related to the  
37 use of different cloud algorithms, leading to a positive bias of OMI compared to TROPOMI of up to 30% in Tropical  
38 regions. We show that after switching off the explicit correction for cloud effects, the two datasets come into an  
39 excellent agreement. For medium to large HCHO vertical columns (larger than  $5 \times 10^{15} \text{ molec.cm}^{-2}$ ) the median bias  
40 between OMI and TROPOMI HCHO columns is not larger than 10% ( $< 0.4 \times 10^{15} \text{ molec.cm}^{-2}$ ). For lower columns,  
41 OMI observations present a remaining positive bias of about 20% ( $< 0.8 \times 10^{15} \text{ molec.cm}^{-2}$ ) compared to TROPOMI in  
42 mid-latitude regions. Here, we also use a global network of 18 MAX-DOAS instruments to validate both satellite

43 sensors for a large range of HCHO columns. This work complements the study by Vigouroux et al. (2020) where a  
44 global FTIR network is used to validate the TROPOMI HCHO operational product. Consistent with the FTIR  
45 validation study, we find that for elevated HCHO columns, TROPOMI data are systematically low (-25% for HCHO  
46 columns larger than  $8 \times 10^{15}$  molec.cm<sup>-2</sup>), while no significant bias is found for medium range column values. We  
47 further show that OMI and TROPOMI data present equivalent biases for large HCHO levels. However, TROPOMI  
48 significantly improves the precision of the HCHO observations at short temporal scales, and for low HCHO columns.  
49 We show that compared to OMI, the precision of the TROPOMI HCHO columns is improved by 25% for individual  
50 pixels, and up to a factor of 3 when considering daily averages in 20km-radius circles. The validation precision  
51 obtained with daily TROPOMI observations is comparable to the one obtained with monthly OMI observations. To  
52 illustrate the improved performances of TROPOMI in capturing weak HCHO signals, we present clear detection of  
53 HCHO column enhancements related to shipping emissions in the Indian Ocean. This is achieved by averaging data  
54 over a much shorter period (3 months) than required with previous sensors (5 years), and opens new perspectives to  
55 study shipping emissions of VOCs and related atmospheric chemical interactions.

## 56 **1 Introduction**

57 Satellite observations of tropospheric formaldehyde (HCHO) columns have been used for years to support air quality  
58 and chemistry-climate related studies from the regional to the global scale. Formaldehyde is an intermediate gas in  
59 almost all oxidation chains of non-methane volatile organic compounds (NMVOC), leading to the production of  
60 carbon monoxide (CO), and eventually carbon dioxide (CO<sub>2</sub>). NMVOCs are, together with nitrogen oxides (NO<sub>x</sub>),  
61 CO and methane (CH<sub>4</sub>), among the most important precursors of tropospheric ozone. NMVOCs also produce  
62 secondary organic aerosols and influence the concentrations of hydroxyl radical (OH), the main tropospheric oxidant.  
63 The major HCHO source in the remote atmosphere is CH<sub>4</sub> oxidation. Over the continents, the oxidation of other  
64 NMVOCs emitted from vegetation, fires, traffic and industrial sources results in important and localised enhancements  
65 of the HCHO levels. Because of its short lifetime (of the order of a few hours), HCHO in the boundary layer can be  
66 related to the release of a large number of short-lived volatile hydrocarbons. Furthermore, HCHO observations provide  
67 information on the chemical oxidation processes in the atmosphere, including CO chemical production from CH<sub>4</sub> and  
68 NMVOC, the oxidation of isoprene into HCHO, which allows quantification of midday OH (Wells et al., Nature,  
69 2019), and the tropospheric ozone production regimes that depend on the HCHO to NO<sub>2</sub> ratios (Jin et al., 2020).

70 Satellite observations of formaldehyde columns in the troposphere have been extensively reported in the literature  
71 from a number of nadir UV sensors, e.g.: Global Ozone Monitoring Experiment (GOME; Chance et al., 2000; Palmer  
72 et al., 2001; De Smedt et al., 2008), SCanning Imaging Absorption spectroMeter for Atmospheric CHartographyY  
73 (SCIAMACHY; Wittrock et al., 2006; De Smedt et al., 2008; 2010), Ozone Monitoring Instrument (OMI; González  
74 Abad et al., 2015; De Smedt et al., 2015; 2018; Kaiser et al. 2018; Levelt et al., 2018), Global Ozone Monitoring  
75 Experiment-2 (GOME-2; De Smedt et al., 2012; 2015; Vrekoussis et al., 2010; Hewson et al., 2013; Hassinen et al.,  
76 2016), and Ozone Mapping and Profiler Suite (OMPS; Li et al., 2015; González Abad et al., 2016). They are used in  
77 many studies related to air quality and climate change (e.g. Stavrou et al., 2014; 2015; 2016; 2018; Fortems-Cheiney  
78 et al., 2012; Marais et al., 2012; Mahajan et al., 2015; Choi et al., 2015; Zhu et al., 2016; Chan Miller et al., 2017; Jin

79 et al., 2017; Barkley et al., 2017; Cao et al., 2018; Khan et al., 2018; Surl et al., 2018; Shen et al. 2019; Su et al.; 2019;  
80 Zyrichidou et al., 2019; Jin et al., 2020; Souri et al., 2020; Wells et al., 2020; Franco et al., 2021; Opacka et al., 2021).  
81 Launched on board of the European Copernicus Sentinel-5 Precursor (S5P) satellite on 13 October 2017, the  
82 TROPospheric Monitoring Instrument (TROPOMI, Veefkind et al., 2012) is designed for the daily monitoring of the  
83 troposphere at the global scale. Compared to its predecessor OMI, its spatial resolution is about 16 times better with  
84 at least the same signal to noise ratio per ground pixel. The improved TROPOMI capabilities for the observation of  
85 HCHO have been illustrated for the detection of fire plumes and their transport (Alvarado et al., 2020; Theys et al.  
86 2020), and the detection of rapid changes in anthropogenic emissions related to the COVID crisis in China and India  
87 (Levelt et al., 2021; Sun et al. 2021). The TROPOMI observations extend the historical time series of midday  
88 observations performed using OMI. Both datasets are used in combination for long-term trend studies (Li et al., 2020).  
89 It is therefore important to evaluate their level of agreement and to report on the best practices to combine datasets  
90 from different sensors.

91 The TROPOMI vertical column product requirements specify a single measurement precision of  $12 \times 10^{15}$  molec.cm<sup>2</sup>,  
92  $4 \times 10^{15}$  molec.cm<sup>2</sup> at 20km spatial resolution, and a systematic uncertainty lower than 40%-80% (ESA, 2014). The  
93 Copernicus user requirements, primarily defined for NMVOC measurements, are more stringent. For the  
94 environmental air quality theme, the required maximum uncertainty is defined as 60% or  $1.3 \times 10^{15}$  molec.cm<sup>2</sup> (least  
95 stringent), at the spatial resolution of 20km and with a revisit time of 2 hours. The space and time resolution are less  
96 stringent for the climate theme (30% or  $1.3 \times 10^{15}$  molec.cm<sup>2</sup>, 50km, 3 days) (Bovensmann et al., 2011; Langen et al.,  
97 2017).

98 Given these rather strict product requirements and the diversity of the NMVOC species, lifetimes and sources  
99 (biogenic, biomass burning or anthropogenic), a validation approach addressing a large variety of conditions  
100 worldwide (tropical, temperate and boreal forests, urban and sub-urban areas) is needed, as well as continuous  
101 measurements in order to obtain good statistics and capture the seasonal variations. Vigouroux et al. (2020) validated  
102 the operational TROPOMI HCHO product using a global network of Fourier Transform Infrared (FTIR) instruments.  
103 The study concluded that overall the HCHO product fulfils the requirements of the TROPOMI mission. Compared to  
104 the FTIR data, the TROPOMI HCHO columns present a negative bias over high concentrations sites (-31% for HCHO  
105 columns larger than  $8 \times 10^{15}$  molec.cm<sup>2</sup>) and a positive bias for clean sites (+26% for HCHO columns lower than  $2.5$   
106  $\times 10^{15}$  molec.cm<sup>2</sup>). Based on clean sites, an upper limit of  $1.3 \times 10^{15}$  molec.cm<sup>2</sup> was estimated for the deviation of daily  
107 observations at a spatial resolution of 20km. It was also pointed out that this level of random uncertainty, although  
108 reaching the Copernicus user requirements, is about twice as large as the expected theoretical noise (individual pixel  
109 precision divided by the square root of the number of observations). However, Vigouroux et al. (2020) do not address  
110 the consistency of TROPOMI HCHO with other satellite products and MAX-DOAS HCHO observations.

111 The present paper is a follow-up of De Smedt et al. (2018), where the HCHO retrieval algorithm applied to both OMI  
112 and TROPOMI sensors was presented. Here we concentrate on a global study of three years of HCHO observations  
113 with TROPOMI, and we analyse their consistency with OMI data. Throughout the paper, we discuss the improved  
114 capabilities of TROPOMI for the detection of HCHO at different temporal and spatial scales, from background  
115 conditions to high emissions. We start with a few illustrations of the TROPOMI capabilities for HCHO monitoring

116 from space (sect. 3). We then provide a detailed comparison with the OMI QA4ECV HCHO dataset (sect. 4). In sect.  
117 5, a global network of MAX-DOAS instruments is used to validate the OMI and TROPOMI HCHO datasets. Finally,  
118 in sect. 6, we illustrate the enhanced capability of TROPOMI for the detection of very small HCHO emissions with  
119 the identification of a signal over shipping lanes in the Indian Ocean.

## 120 **2 HCHO Datasets**

### 121 **2.1 OMI instrument and QA4ECV HCHO product**

122 The Aura satellite was launched in July 2004, in a low-Earth polar orbit crossing the equator at 13:30 LT. On board  
123 Aura, the Ozone Monitoring Instrument (OMI) is a nadir viewing imaging spectrometer that measures the solar  
124 radiation backscattered by the Earth's atmosphere and surface over the wavelength range from 270 to 500 nm (Levelt  
125 et al., 2006). Operational Level 2 (L2) products include vertical columns of O<sub>3</sub>, SO<sub>2</sub>, NO<sub>2</sub>, HCHO, BrO, OCIO, as  
126 well as cloud and aerosol information. OMI has a 2600 km wide swath (divided into 60 across-track positions or  
127 rows), providing near-daily global coverage. However, due to a detector row anomaly that occurred after a few years  
128 of operation, an increasing number of rows had to be filtered out leading to gradual degradation of the coverage. The  
129 OMI ground pixel size varies from 13x24 km<sup>2</sup> at nadir to 28x150 km<sup>2</sup> at the edges of the swath.

130 The OMI QA4ECV HCHO product was developed by a European consortium (BIRA, IUP, MPIC, KNMI, WUR) (De  
131 Smedt et al., 2017, <http://doi.org/10.18758/71021031>) in the framework of the EU-FP7 QA4ECV project. A detailed  
132 step-by-step study was performed for HCHO and NO<sub>2</sub> retrievals as part of a community effort to homogenize GOME,  
133 SCIAMACHY, GOME-2 and OMI, leading to state-of-the art European products ([www.qa4ecv.eu](http://www.qa4ecv.eu)). For this study,  
134 we use the version 1.2 of the OMI HCHO dataset that is now spanning 15 years (2005-2020; Boersma et al., 2018;  
135 Lorente et al., 2017; Nightingale et al., 2018; Zara et al., 2018). Note that within QA4ECV, a homogenized dataset of  
136 NO<sub>2</sub> and HCHO MAX-DOAS reference measurements (QA4ECV MAXDOAS) was also developed for satellite  
137 validation (see sect. 2.4 and sect. 5).

### 138 **2.2 TROPOMI instrument and the HCHO operational product**

139 On board the S5P platform, which - like Aura - flies in a low-Earth afternoon polar orbit with a local overpass time of  
140 13:30, the TROPOMI instrument is based on an imaging spectrometer measuring in the ultraviolet (UV), visible (VIS),  
141 near-infrared (NIR), and shortwave infrared (SWIR) spectral regions (Veeffkind et al., 2012). Operational L2 products  
142 include vertical columns of O<sub>3</sub>, SO<sub>2</sub>, NO<sub>2</sub>, HCHO, CO and CH<sub>4</sub>, as well as cloud and aerosol information. TROPOMI  
143 has a 2600 km wide swath (divided into 450 across-track positions or rows), providing near-daily global coverage.  
144 The spatial resolution at nadir, originally of 3.5x7 km<sup>2</sup> (across-track x along-track) has been refined to 3.5x5.5 km<sup>2</sup>  
145 on 6 August 2019, by a change in the along-track integration time. The size of the pixels remains more or less constant  
146 towards the edges of the swath (the largest pixels are ~14 km wide) (L1b ATBD, L1b readme file).

147 The retrieval algorithm of the TROPOMI HCHO L2 product is directly inherited from the QA4ECV OMI algorithm  
148 with the aim to create a consistent time series of early afternoon observations. For this study, we use a modified version  
149 of the TROPOMI level-2 HCHO operational data product, which starts in April 2018 (phase E2, RPRO+OFFL,

150 product versions 1.1.[5-8]+2.1.3, doi: 10.5270/S5P-tjlxfd2). Product versions are described in the [Product Readme](#)  
151 [File](#).

### 152 2.3 HCHO Retrieval algorithm for OMI and TROPOMI

153 The HCHO retrieval algorithm was fully described in De Smedt et al. (2018), and the successive adaptations of the  
154 algorithm are reported in the S5P product ATBD. Here we only provide a short description of the algorithm, which is  
155 based on a 3-steps DOAS method. First, the fit of the slant columns ( $N_s$ ) is performed in the UV part of the spectra,  
156 in the fitting interval 328.5–359 nm. The HCHO cross-section is from Meller and Moortgat (2000). All cross-sections  
157 have been pre-convolved for every row separately with an instrumental slit function adjusted after TROPOMI launch.  
158 For the OMI product, the slit function of each row is adjusted daily and the cross-sections are reconvolved accordingly.  
159 The DOAS reference spectrum is updated daily with an average of Earth radiances measured in the Equatorial Pacific  
160 region from the previous day. The fit therefore results in a differential slant column, corresponding to the HCHO  
161 excess over sources compared to the remote background. In a second step, the conversion from slant to tropospheric  
162 vertical columns ( $N_v$ ) is performed using a look up table of vertically resolved air mass factors ( $M$ ) calculated at 340  
163 nm with the radiative transfer model VLIDORT v2.6 (Spurr, 2008). Entries for each ground pixel are the observation  
164 geometry, the surface elevation and reflectivity, as well as clouds treated as reflecting surfaces, and a priori  
165 tropospheric HCHO profiles. The surface albedo is taken from the monthly OMI albedo climatology at the spatial  
166 resolution of  $1^\circ \times 1^\circ$  (minimum LER, Kleipool et al., 2008). A priori vertical profiles are provided by the TM5-MP  
167 daily analysis, at the spatial resolution of  $1^\circ \times 1^\circ$  (Williams et al., 2017). A cloud correction based on the independent  
168 pixel approximation (Boersma et al., 2004) is applied for cloud fractions (CF) larger than 0.1. Finally, to correct for  
169 any remaining global offset and possible stripes arising between the rows, a background correction is performed based  
170 on the HCHO slant columns in the Pacific Ocean ( $N_{s,0}$ ). For the TROPOMI operational product,  $N_{s,0}$  is based on the  
171 four previous days. For this study, and for the OMI product, we perform the correction on the current day in order to  
172 further reduce the stripes. To compensate for a background HCHO level in the Equatorial Pacific (due to the methane  
173 oxidation), a vertical column of HCHO ( $N_{v,0}^{CTM}$ ) is taken from the TM5 model in the reference region. The resulting  
174 tropospheric HCHO vertical column can be written as follows:

$$N_v = \frac{N_s - N_{s,0}}{M} + \frac{M_0}{M} N_{v,0}^{CTM}, \quad (2-1)$$

175 with  $M_0$  the air mass factor in the reference sector. Intermediate quantities and auxiliary data are all stored in the L2  
176 files (see the product user manual for TROPOMI and OMI). Several diagnostic variables are provided together with  
177 the measurements. The column averaging kernels and the a priori profiles are given for each observation. The  
178 tropospheric column uncertainty is resolved into its random (precision) and systematic components (accuracy), and is  
179 provided for every individual pixel.

180 The main difference between the OMI and TROPOMI algorithms lies in the cloud product that is used to compute air  
181 mass factors. While the QA4ECV OMI product is based on the  $O_2-O_2$  absorption feature around 477 nm, and considers  
182 a fixed cloud albedo of 0.8 (version 2.0, Veeffkind et al., 2016), the TROPOMI product uses the S5P operational cloud  
183 product in CRB (Cloud as Reflecting Boundary) mode (OCRA/ROCINN-CRB; Loyola et al., 2018). The S5P

184 ROCINN algorithm is based on the O<sub>2</sub> A-band around 760 nm and simultaneously retrieves cloud height and cloud  
185 albedo. Systematic differences between the cloud parameters will result in differences in the air mass factors,  
186 influencing the comparisons. To mitigate the impact of this difference between OMI and TROPOMI, we also switch  
187 off the cloud correction by replacing the cloud-corrected AMF by an equivalent clear-sky AMF ( $M_{clear}$ , no cloud  
188 correction applied) also provided in the L2 product. Based on equation (2-1), the following simple transformation can  
189 be applied:

$$N_{v\_clear} = \frac{M}{M_{clear}} N_v \quad (2-2)$$

190 Note that this transformation has an effect on observations with cloud fractions comprised between 0.1 and 0.4. Indeed,  
191 no cloud correction is applied for CF<0.1 and observations with CF>0.4 are filtered out from the analysis.

## 192 2.4 MAX-DOAS datasets

193 Multi-axis DOAS (MAX-DOAS) instruments retrieve the abundance of atmospheric trace species in the lowermost  
194 troposphere (Hönninger et al., 2004; Wagner et al., 2004; Wittrock et al., 2004; Heckel et al., 2005). Based on DOAS  
195 analyses (Platt and Stutz, 2008) of the scattered sky light under different viewing elevations, high sensitivity close to  
196 the surface is obtained for the smallest elevation angles, whereas measurements at higher elevations provide  
197 information on the rest of the column. MAX-DOAS measurements have been used in several studies to validate  
198 satellite HCHO columns (Vigouroux et al., 2009; Franco et al., 2015; De Smedt et al., 2015; Chan et al., 2019; 2020;  
199 Ryan et al., 2020; Kumar et al. 2020). However, a global network of MAX-DOAS instruments has not been used yet  
200 for the validation of HCHO columns from space.

201 Ground-based data used in this study are presented in Table 1. Apart from the QA4ECV MAX-DOAS dataset, which  
202 relies on harmonized HCHO retrievals (Pinaridi et al., 2013; QA4ECV [D3.8](#) and [D3.9](#),  
203 <http://www.qa4ecv.eu/sites/default/files>), the MAX-DOAS data sets used here were generated by instrument principal  
204 investigators using non-harmonised settings. The conversion to vertical columns and/or vertical profiles relies on  
205 methods of various complexity levels. Table 1 includes details about the retrieval strategy adopted by the different  
206 teams. These include:

- 207 • GA: Geometrical approximation, the vertical column is determined using a single-scattering approximation  
208 adequate for moderately high elevation angles  $\alpha$  (typically 30°) so that a simple geometrical air-mass factor  
209 ( $AMF \approx SCD/VCD = 1/\sin(\alpha)$ ) (Hönninger et al., 2004; Brinksma et al., 2008; Ma et al., 2013) can be used,
- 210 • QA4ECV: the vertical column is calculated using tropospheric AMFs based on climatological profiles and  
211 aerosol loads as developed during the QA4ECV project ([QA4ECV\\_MAXDOAS\\_readmefile](#)). These data are  
212 less sensitive to relative azimuth angle than the purely geometric approximation presented above,
- 213 • OEM: Vertical profile algorithms using an Optimal Estimation Method (Rodgers, 2000): these make use of a-  
214 priori vertical profiles and associated uncertainties (Friess et al., 2006; Clémer et al 2010; Hendrick et al., 2014;  
215 Gielen et al., 2017; Wang et al., 2019a; Friedrich et al., 2019; Bösch et al., 2018),

216 • PP: Vertical profile algorithms based on parameterized profile shape functions: these make use of analytical  
 217 expressions to represent the trace gas profile using a limited number of parameters (Irie et al., 2009; 2011; Li et  
 218 al., 2010; Vlemmix et al., 2010; Wagner et al., 2011; Beirle et al., 2019).

219 Both OEM and parameterized profiling approaches provide vertical profiles of aerosols and HCHO with good  
 220 sensitivity in the 0-4 km altitude range, in which 1 to 3 independent pieces of information in the vertical dimension  
 221 are available (Vlemmix et al., 2015; Friess et al., 2016; 2019). Recent intercomparison studies (Vlemmix et al., 2015;  
 222 Friess et al., 2019; Tirpitz et al., 2021) show that both OEM and parameterized inversion approaches lead to consistent  
 223 results in terms of tropospheric vertical columns but to larger differences in terms of profiles. The accuracy of the  
 224 MAX-DOAS technique depends on the SCD retrieval noise, the uncertainty of the HCHO absorption cross-sections,  
 225 the choice of the a-priori profile shape and the uncertainty of the tropospheric AMF calculation. MAX-DOAS HCHO  
 226 slant columns from several instruments have been compared during international large-scale campaigns (CINDI-1 and  
 227 2, e.g. Pinardi et al., 2013; Kreher et al., 2020) showing relatively large median differences and larger noise compared  
 228 to other slant column products comparisons (e.g. NO<sub>2</sub>). For HCHO, the slant column precision depends strongly on  
 229 the signal-to-noise performance of the DOAS instrument with significantly better results for low-noise research-grade  
 230 MAX-DOAS instruments (Pinardi et al., 2013; Kreher et al., 2020). The estimated total uncertainty on HCHO VCD  
 231 is of the order of 30% to 60% in polluted conditions. This includes both random (~5% to 30% depending on  
 232 instrumental signal-to-noise ratio) and systematic (20%) slant column contributions (Pinardi et al., 2013).

233 **Table 1: MAX-DOAS HCHO datasets included in the validation exercise. GA stands for geometrical approximation, OEM**  
 234 **for Optimal Estimation Method and PP for Parametrized Profiling.**

Station, Country (lat/long)	Owner/ Group	Instrument Type	Retrieval Type	Reference
De Bilt, The Netherlands (52.10°N, 5.18°E)	KNMI	miniDOAS / Airyx	SCD and VCD from QA4ECV	Vlemmix et al., 2010 QA4ECV
Cabauw, The Netherlands (51.97°N, 4.93°E)	KNMI	miniDOAS/ Hoffmann	SCD and VCD from QA4ECV	QA4ECV
Uccle, Belgium (50.78° N, 4.35° E)	BIRA-IASB	Custom-built MAX-DOAS	VCD and profiles from OEM	Dimitropoulou et al, 2020
Xianghe, China (39.75° N, 116.96° E)	BIRA-IASB	Custom-built MAX-DOAS	VCD and profiles from OEM	Hendrick et al., 2014; Vlemmix et al., 2015
Mainz, Germany (50°N, 8.2°E)	MPIC	Custom-built MAX-DOAS	SCD and VCD from QA4ECV	Wang et al., 2017 QA4ECV
Munich, Germany (48,13_N, 11.58°E)	LMU	Airyx 2D MAX-DOAS	VCD and profiles from OEM	Chan et al. 2020
Mohali, India (30.67°N, 76.74°E)	IISER/MPIC	Custom-built MAX-DOAS	SCD and VCD from QA4ECV	Kumar et al., 2020 QA4ECV
Thessaloniki, Greece (40.63°N, 22.96°E)	AUTH	Phaethon	SCD and VCD from QA4ECV	Drosoglou et al., 2017 QA4ECV
Madrid, Spain (40.3°N, 3.7°W)	CSIC	MAX-DOAS	VCD and profiles from OEM	Benavent, et al., 2019.
Fukue, Japan (36.8°N, 128.7°E)	ChibaU	CHIBA-U MAX- DOAS	VCD and profiles from PP	Irie et al., 2011; 2012; 2015; 2019.

<b>Chiba, Japan</b> (35.63°N, 140.10°E)	ChibaU	CHIBA-U MAX-DOAS	VCD and profiles from PP	Irie et al., 2011; 2012; 2015; 2019.
<b>Kasuga, Japan</b> (33.52°N, 130.48°E)	ChibaU	CHIBA-U MAX-DOAS	VCD and profiles from PP	Irie et al., 2011; 2012; 2015; 2019.
<b>Pantnagar, India</b> (29°N, 79.47°E)	ChibaU	CHIBA-U MAX-DOAS	VCD and profiles from PP	Irie et al., 2011; 2012; 2015; 2019.
<b>Phimai, Thailand</b> (15.18°N, 102.56°E)	ChibaU	CHIBA-U MAX-DOAS	VCD and profiles from PP	Irie et al., 2011; 2012; 2015; 2019.
<b>Xianghe, China</b> (39.75° N, 116.96° E)	USTC	MAX-DOAS	VCD from OEM	
<b>Beijing CAMS, China,</b> (39.95°N, 116.32°E)	USTC	MAX-DOAS	VCD from GA	
<b>UNAM, Mexico</b> (19.33°N, 99.18°W)	UNAM	MAX-DOAS	VCD and profiles from OEM Eastwards pointing	Rivera Cardenas et al., 2021 Arellano et al., 2016
<b>BroadMeadows, Australia</b> (-37.7°, 144.9°)	Melbourne University ABM	Airyx	VCD from OEM	Ryan et al. 2018; 2020.

## 235 2.5 Data Use and Method

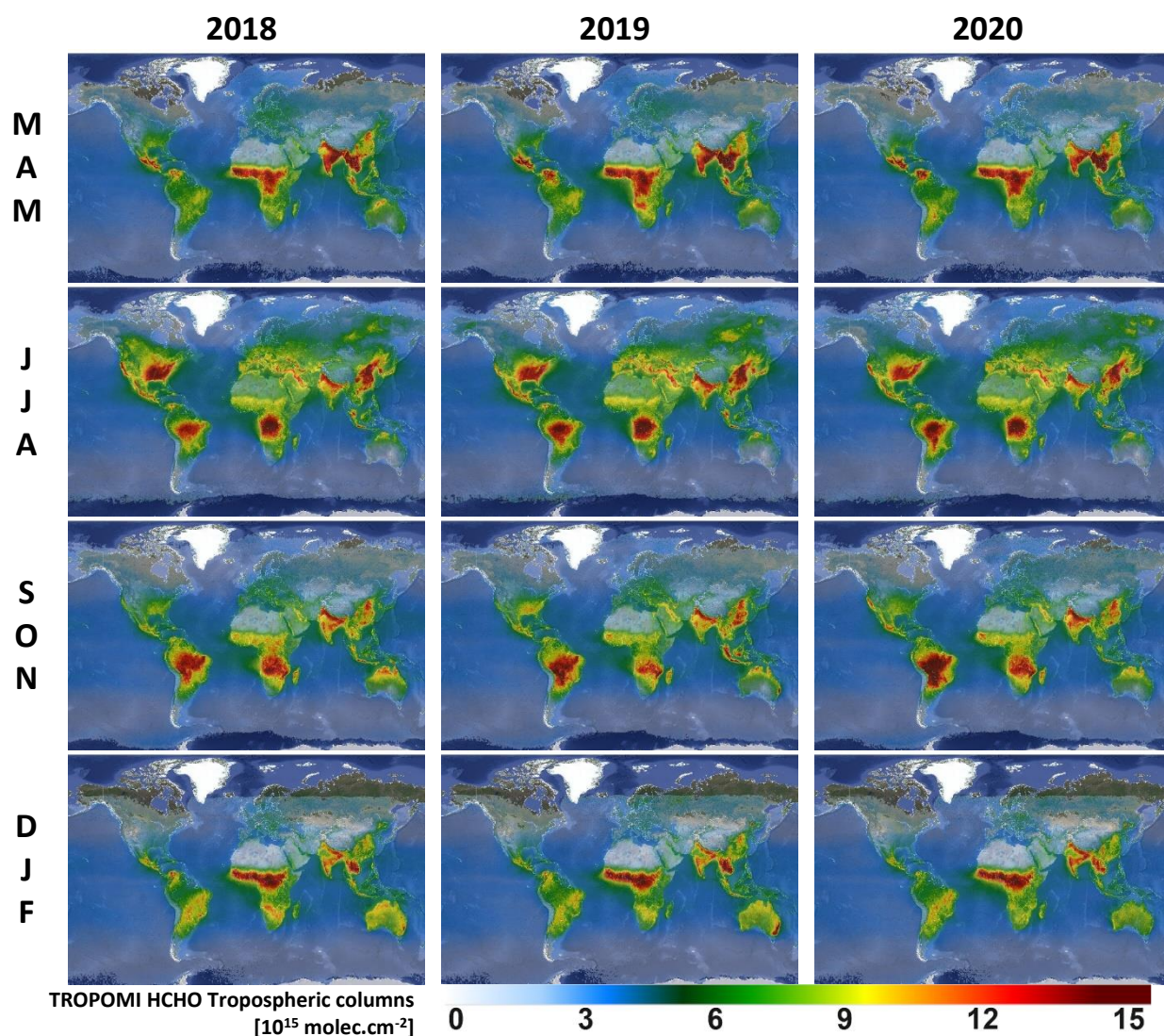
236 For this study, unless specified otherwise, we filter the satellite data based on the quality assurance values (QA)  
237 ([Product Readme File](#)). QA>0.5 filters out most observations presenting an error flag or a solar zenith angle larger  
238 than 70°, a cloud radiance fraction (CRF) at 340 nm larger than 0.6, an air mass factor smaller than 0.1, surface  
239 reflectivity larger than 0.2, or an activated snow/ice flag. It should be noted that, in the first versions of the operational  
240 product, the QA values were not correctly assigned over snow/ice regions, above 75° of SZA, and sometimes over  
241 cloudy scenes. This issue has been corrected from version 2.1.3 (July 2020). For this study, we therefore reassigned  
242 QA values using the above-mentioned filters.

243 We calculated daily gridded data at a resolution of 0.05°x0.05° in latitude/longitude, both for OMI and TROPOMI,  
244 using the [Harp atmospheric toolbox](#). Throughout the paper, daily and monthly averages are obtained from daily grids.  
245 For each day, we require the region to be filled with a least 50% of valid grid cells, with a minimum of 10 TROPOMI  
246 observations (2 OMI observations).

247 For the satellite/satellite and the satellite/ground-based comparisons, we calculate the median of the absolute  
248 differences (absolute bias) and the median of the relative differences (relative bias) in each region or station (relative  
249 either to TROPOMI in the case of sat./sat. or to the MAX-DOAS columns in the case of sat./ground-based). The  
250 corresponding median absolute-value deviations (MAD) of the absolute and relative differences are a robust estimate  
251 of the combined observation and comparison variability. The MAD is defined as the median of the absolute-value  
252 deviations from the data's median:

$$MAD = k \cdot \text{median}(\text{abs}(\text{Diff}_i - \text{median}(\text{Diff}_i))) \quad (2-3)$$

253 where the factor k=1.4826 is used to ensure a correspondence with the 1-sigma standard deviation for normal  
254 distribution. The bias is considered as statistically significant if it exceeds  $\text{ErrB}=2 \cdot \text{MAD}/\sqrt{N}$ , where N is the  
255 number of collocated pairs (days or months). We also derive correlation, slope and offset of the linear regression using  
256 the robust Teil-Shein estimator (Sen, 1968) as done in Vigouroux et al. (2020).

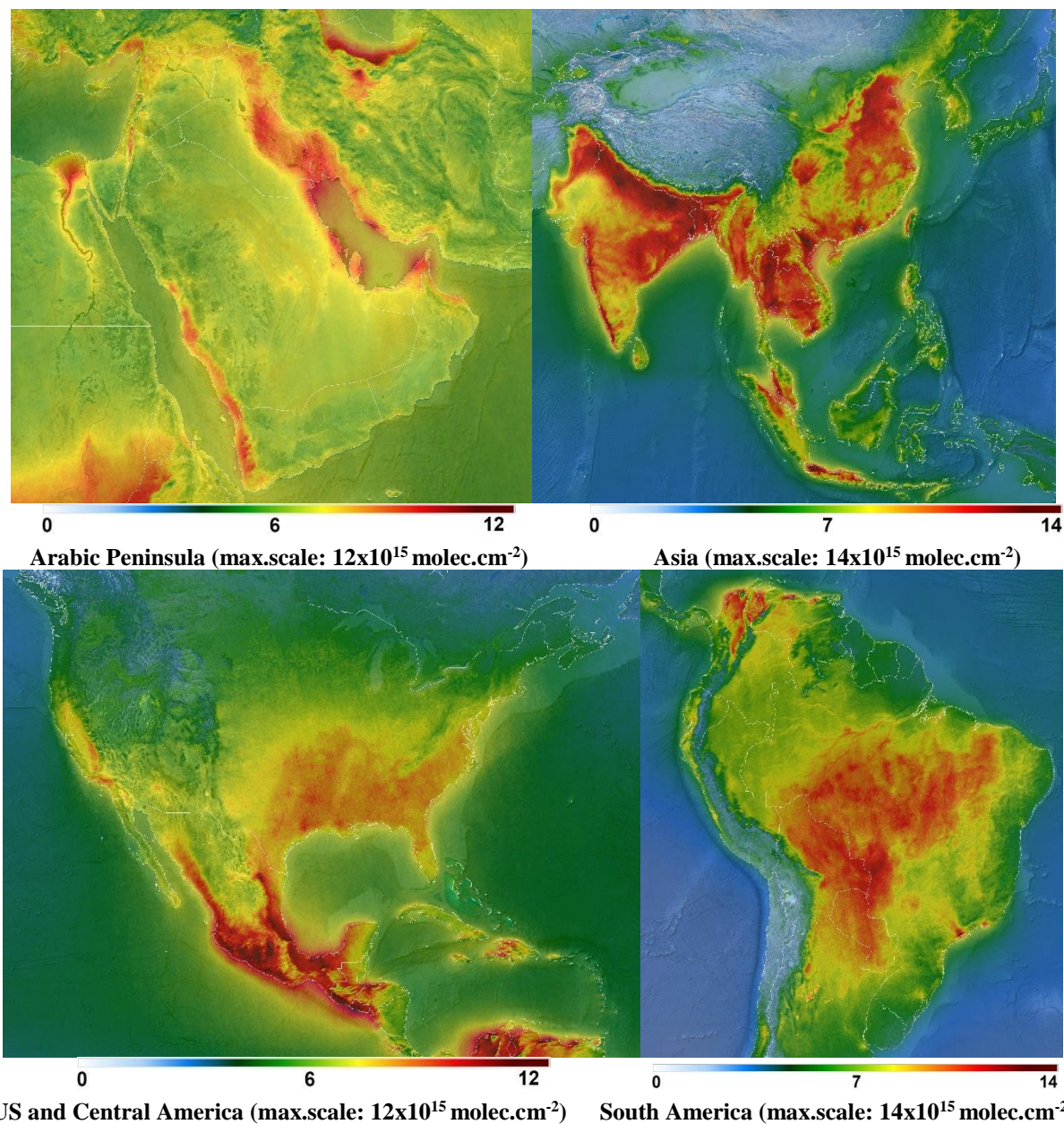


258 **Figure 1: Seasonal maps of TROPOMI HCHO tropospheric columns during the three first years of measurements (March**  
 259 **2018 – February 2021), on a spatial grid of  $0.05^\circ$  in latitude and longitude. Observations are filtered using the  $qa\_values > 0.5$ .**  
 260 **(max.scale:  $15 \times 10^{15}$  molec. $\text{cm}^{-2}$ ). Modified Copernicus Sentinel-5P satellite data, OFFL L2 HCHO product, BIRA-**  
 261 **IASB/DLR/ESA/EU.**

262 As an illustration of the data product, Figure 1 displays the global seasonal distribution of tropospheric HCHO columns  
 263 derived from TROPOMI observations between March 2018 and February 2021. The overall seasonality of the HCHO  
 264 columns is largely driven by the emissions of NMVOCs from the vegetation and by the interannual variability of  
 265 surface temperatures and solar radiation. As can be seen, in South Eastern US for example, the seasonal amplitude is  
 266 very important and dominated by biogenic emissions during summertime. On top of biogenic emissions, wildfires  
 267 present a large variability. Since 2018, many fire events occurred worldwide and can be traced e.g. in HCHO columns  
 268 during summer 2018 and 2020 in Western US, or during summer 2019 in Siberia. After a decrease of about 10 years  
 269 (De Smedt et al., 2015), South America experienced two intense fire seasons in 2019 and 2020. The year 2020 was  
 270 also marked by the huge Australian and Californian wildfires, respectively, in January and October 2020, detectable

271 in the seasonal maps. In comparison to biogenic and pyrogenic emissions of natural origin, the contribution due to  
272 anthropogenic NMVOC emissions to the total HCHO columns is generally lower. Although their oxidation is also  
273 enhanced by sunlight, anthropogenic emissions show less seasonality than natural emissions, and their detection is  
274 therefore generally easier in annual maps. This is illustrated in Figure 2, which presents 3-year averages of HCHO  
275 columns over Asia, the Arabic Peninsula, the US and Central and South America, providing detailed information  
276 about the spatial distribution of HCHO at the regional and urban scale. Europe and Africa are shown in the supplement  
277 (fig.S1). Note that the colour scale has been adapted to the regions. Large urban areas are clearly visible in the HCHO  
278 distribution in Asia, the Middle East and South America. With a lower magnitude, US cities are also clearly detectable,  
279 such as Houston, Dallas or Los Angeles. HCHO levels are noticeably lower in Europe, but some urban areas are  
280 visible in the Southern countries.

281 The quality of the TROPOMI observations also allows observing HCHO columns on a much shorter time scale with  
282 an unprecedented definition. Daily observations of fire plumes are a clear step forward in the satellite remote sensing  
283 of HCHO. They can be observed over much longer distances than before, thanks to the daily global coverage, coupled  
284 with the finer spatial resolution and the improved signal to noise ratio, allowing the detection of lower columns  
285 transported further away (Alvarado et al. 2020; Theys et al. 2020). Not only wildfires, but also important  
286 anthropogenic emission plumes can be observed on a daily basis, for example on the Eastern coast of Saudi Arabia.  
287 A few illustrations are given in fig.S2. The TROPOMI performances for the observations of HCHO are discussed  
288 more quantitatively along the paper in terms of precision and bias, as a function of the HCHO levels, and of the  
289 temporal and spatial scales.



291 **Figure 2: Multi-annual regional maps of TROPOMI HCHO tropospheric columns (March 2018 – February 2021), on a**  
 292 **spatial grid of 0.05° in latitude and longitude. Observations are filtered using the qa\_values>0.5. Modified Copernicus**  
 293 **Sentinel-5P satellite data, OFFL L2 HCHO product, BIRA-IASB/DLR/ESA/EU.**

#### 294 **4 Comparison between OMI and TROPOMI measurements**

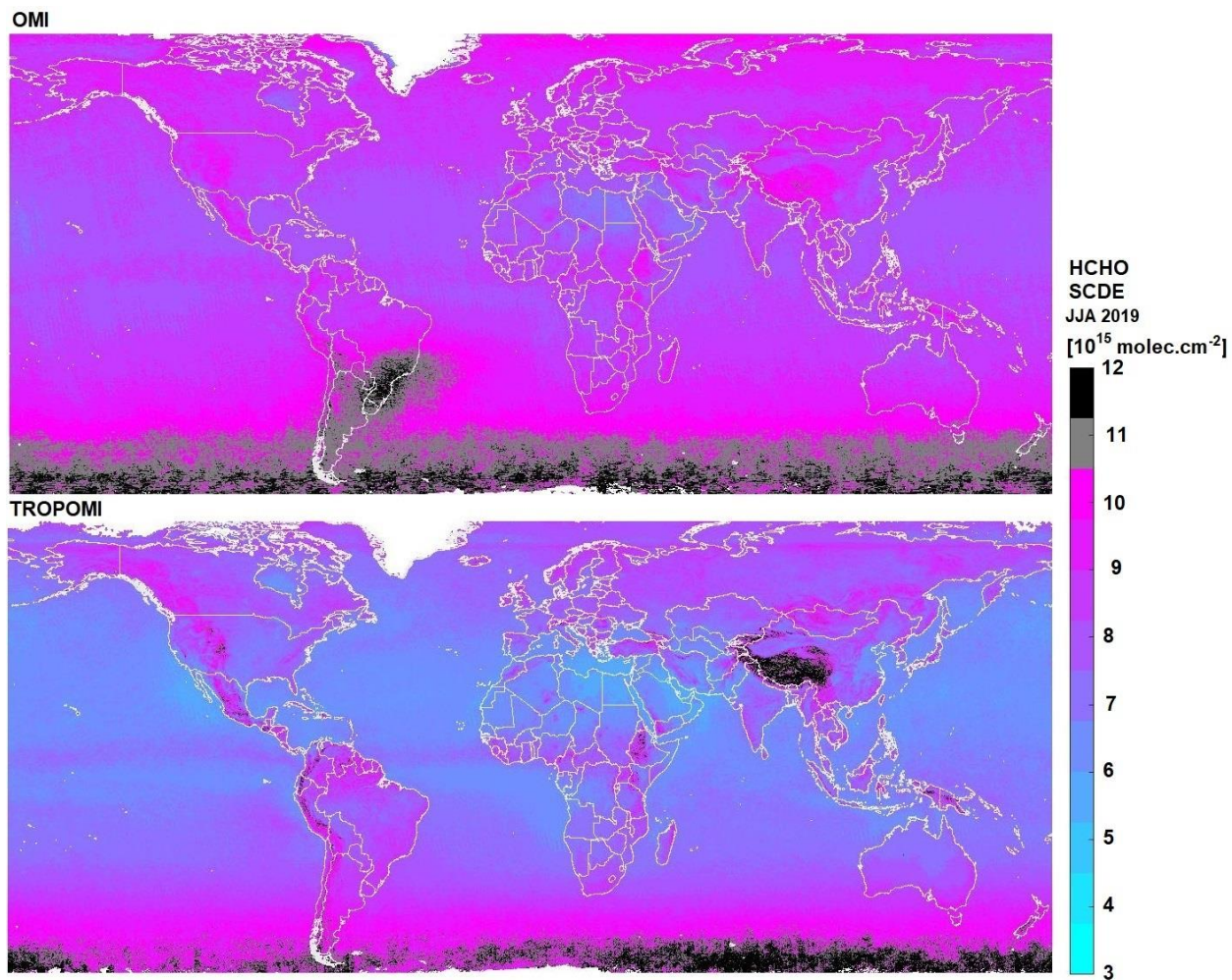
295 In this section, we evaluate the consistency between OMI and TROPOMI HCHO tropospheric columns. In addition,  
 296 we present the gain in precision obtained with TROPOMI. The analysis relies on 32 months of simultaneous  
 297 measurements from April 2018 to December 2020, allowing for a meaningful comparison at different scales. We first

298 compare the precision obtained on individual measurements, and then proceed with a comparison of the precisions  
299 achieved when averaging data at different spatial and temporal scales.

#### 300 **4.1 HCHO slant column precision**

301 The random uncertainty of the tropospheric HCHO column is dominated by the error on the fitted slant column  
302 densities (SCDE) which is directly related to the signal to noise ratio (SNR) of the measurement. From this point of  
303 view, TROPOMI performs significantly better than previously launched nadir UV-VIS satellite instruments. In the  
304 spectral range of HCHO retrievals (328.5-359 nm), the SNR of the TROPOMI spectra exceeds pre-flight requirements  
305 that were based on OMI specifications (Kleipool et al., 2018; Ludewig et al., 2020).

306 Figure 3 presents global maps of SCDE averaged over 3 months during summer 2019, from OMI and TROPOMI.  
307 From the improved SNR of TROPOMI in the UV range, TROPOMI HCHO SCDEs of individual observations are  
308 about 25% lower than OMI ones. Over remote areas, the TROPOMI SCDE is about  $6 \times 10^{15}$  molec.cm<sup>-2</sup>, while it is  
309  $8 \times 10^{15}$  molec.cm<sup>-2</sup> for OMI. Slant column density errors are also improved over emission areas and at larger SZA.  
310 Contrary to OMI, the effect of the South Atlantic Anomaly is absent in TROPOMI SCDE. This probably results from  
311 a better shielding of the instrument against extra-terrestrial high energy radiation. The implemented iterative spike  
312 algorithm (De Smedt et al., 2018) is also more efficient because of the lower noise level of the instrument. Note  
313 however that over mountains, TROPOMI SCDE are higher than OMI ones. The most obvious effect is observed over  
314 the Himalayans, but other chains such as the Andes or the Rocky mountains are also affected. This effect has been  
315 identified as a scene inhomogeneity effect (Richter et al., 2018; 2020). The effect is also visible along the borders of  
316 bright lakes or white surfaces. OMI retrievals are also affected by scene inhomogeneity effects, but the larger size of  
317 the ground pixels and the larger mean SCDE values make its detection more difficult. We note that in the 3-year  
318 averaged maps of the HCHO tropospheric columns, some collocated artefacts appear (Figure 2, e.g. the white sands  
319 in the US, Tuz Golu lake in Turkey or Lake Mackay in Australia). Most of the snow/ice scenes are eliminated by the  
320 quality assurance values. The observations could however be better filtered over mountains and along the lake borders,  
321 or even corrected during the fit of the slant columns as demonstrated for NO<sub>2</sub> and glyoxal (Lerot et al., 2021, in prep.).  
322 The relatively coarse albedo climatology also needs to be updated with a TROPOMI-based product, better defined in  
323 space and time (Loyola et al., 2020).

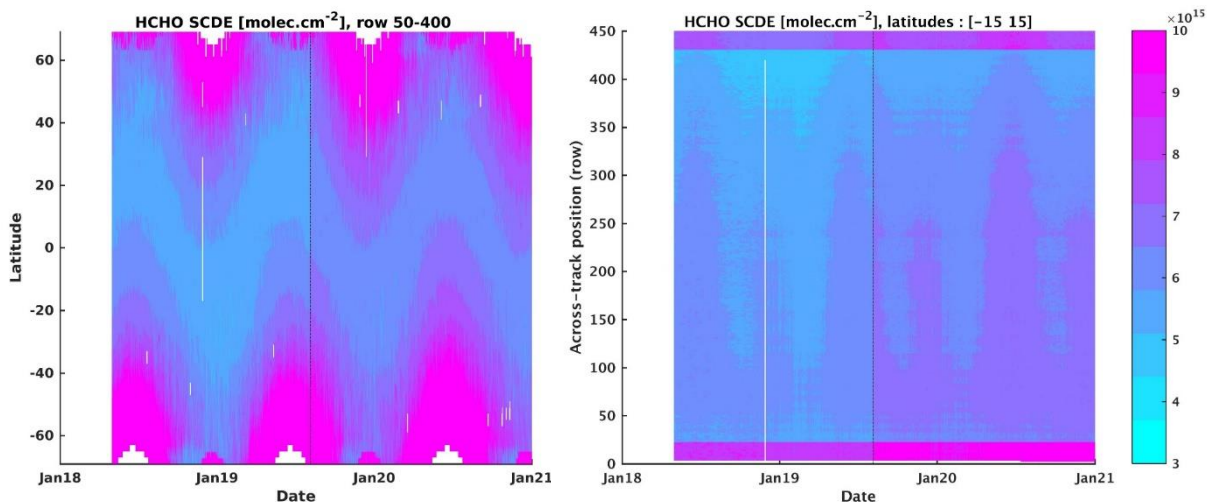


324  
325 **Figure 3: Average HCHO slant column density fitting error (SCDE) retrieved from OMI (upper panel) and TROPOMI**  
326 **(lower panel) in JJA 2019, on a spatial grid of 0.05° in latitude and longitude.**

327 The OMI SCDEs have been very stable over the years, showing a limited increase of about 5% between 2005 and  
328 2019 (De Smedt et al., 2018). However, the number of valid OMI observations has decreased by about 30% during  
329 the same period (-50% at large SZA) due to the row anomaly. In order to evaluate the stability of the TROPOMI  
330 HCHO retrievals during the three first years, Figure 4 presents the time series of the TROPOMI HCHO slant column  
331 errors in the remote Pacific Ocean as a function of latitude and instrumental rows. As expected, we observe an increase  
332 of the noise for large SZAs, and for the 25 first and last rows of the scan, which have a different detector binning ([L1b](#)  
333 [ATBD](#)). The fact that the algorithm makes use of daily updated radiances as reference for the DOAS fit allows for  
334 very stable results in time and across the rows. Only the change in pixel size in August 2019 ([L1b readme file](#)) resulted  
335 in a moderate step increase of the SCDE of about 15%. These values are compared to the observed standard deviation  
336 of the slant columns in the same regions (see fig.S3). We observe a very good agreement between the SCDEs and the  
337 standard deviation, indicating that they give a good representation of the random errors.

338 The reported uncertainty on the tropospheric vertical columns due to random errors corresponds to the SCDE divided  
339 by the AMF for each observation. In the Equatorial Pacific, the TROPOMI vertical column precision is about  $5 \times 10^{15}$

340 molec.cm<sup>-2</sup>, while it is 7x10<sup>15</sup> molec.cm<sup>-2</sup> for OMI. It is larger over continental emissions, where the AMFs are  
 341 generally smaller than 1.

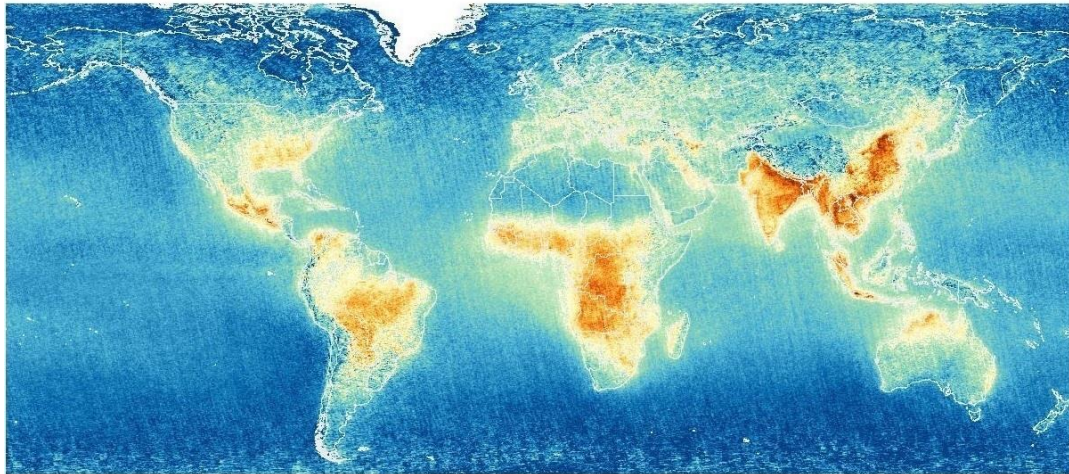


342 **Figure 4: TROPOMI HCHO slant column density errors (SCDE) as a function of the latitude (left column) or the detector**  
 343 **row (right column). The step increase on 6th August 2019 reflects the change in the TROPOMI pixel size (indicated with**  
 344 **the black line).**

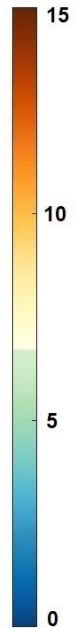
#### 345 4.2 HCHO tropospheric columns

346 Figure 5 presents the yearly averaged OMI and TROPOMI HCHO vertical columns ( $N_{v\_clear}$ ) for 2019. Even at this  
 347 level of averaging, the lower noise level of TROPOMI is very clear, especially for low to medium HCHO levels. We  
 348 observe an overall good agreement of the columns both in magnitude and in their spatial distribution. Differences of  
 349 TROPOMI and OMI yearly averages range from +2x10<sup>15</sup> molec.cm<sup>-2</sup> over Tropics to -2x10<sup>15</sup> molec.cm<sup>-2</sup> over mid-  
 350 latitude regions. Differences tend to increase with latitudes. However, as the quality of the TROPOMI observations is  
 351 improved at large solar zenith angles, more data in winter months are kept in the TROPOMI dataset, which can  
 352 influence yearly averaged columns at those latitudes. In order to provide quantitative comparisons, we calculated daily  
 353 and monthly averaged columns in 35 regions covering a broad range of emission levels and observation conditions  
 354 (large black boxes on Figure 5). As the regions are large, many observations are included (on average 500/day for  
 355 OMI, 12500/day for TROPOMI). To obtain daily and monthly comparison pairs, we keep coincident days of  
 356 observations and follow the methodology presented in sect. 2.5.

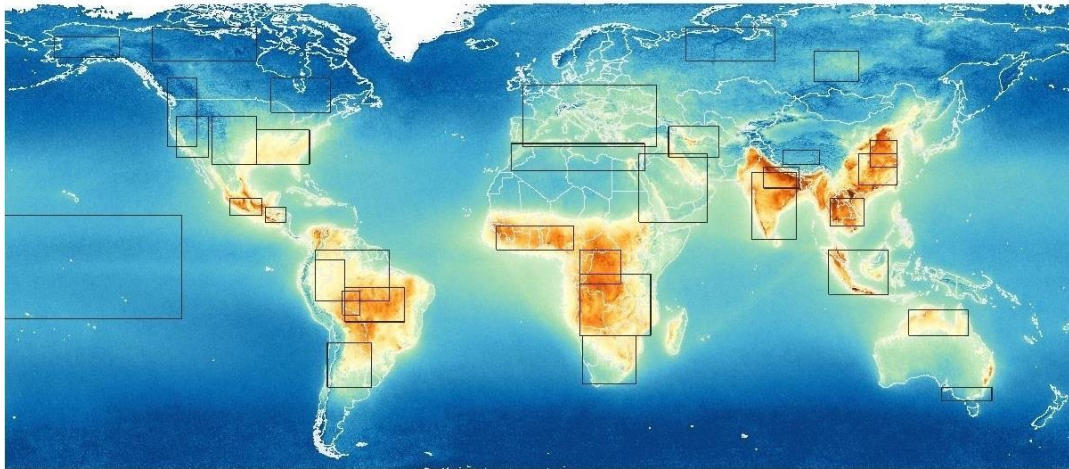
OMI



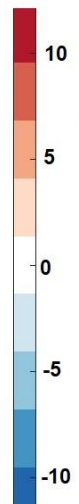
HCHO  
VCD  
2019  
[ $10^{16}$  molec. $\text{cm}^{-2}$ ]



TROPOMI



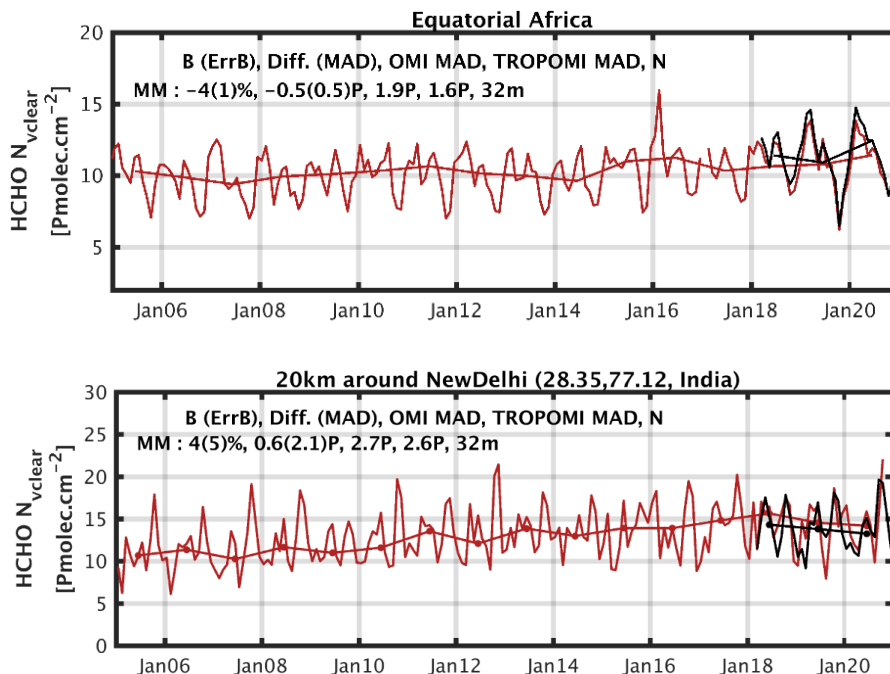
OMI-TROPOMI



357

358 Figure 5: Average HCHO tropospheric column ( $N_{v\_clear}$ ) retrieved from OMI (first line) and TROPOMI (second line) in  
359 2019. Limits of the regions selected for the comparisons are shown on the TROPOMI map. Differences between OMI and  
360 TROPOMI maps are shown on the last panel. The same grid is used for both dataset ( $0.05^\circ$ ). Data are filtered using the  
361 product quality flags. The large black boxes on the TROPOMI maps represent the regions used in the comparisons (see  
362 Figure 6 and Figure 7).

363 An example of a time series over Equatorial Africa is presented on the first panel of Figure 6, where monthly averaged  
 364  $N_{v\_clear}$  are shown, and comparison numbers are provided in the inset. In the Equatorial African region, the seasonal  
 365 cycle is marked by two peaks during the dry seasons and two minima during the wet seasons. In 2019, the minimum  
 366 was particularly low, observed in both the OMI and TROPOMI timeseries, while the maxima tend to increase over  
 367 the years. More examples of time series can be found in fig.S4. In all the regions, the seasonal and interannual  
 368 variability of the HCHO columns are observed very consistently with OMI and TROPOMI.



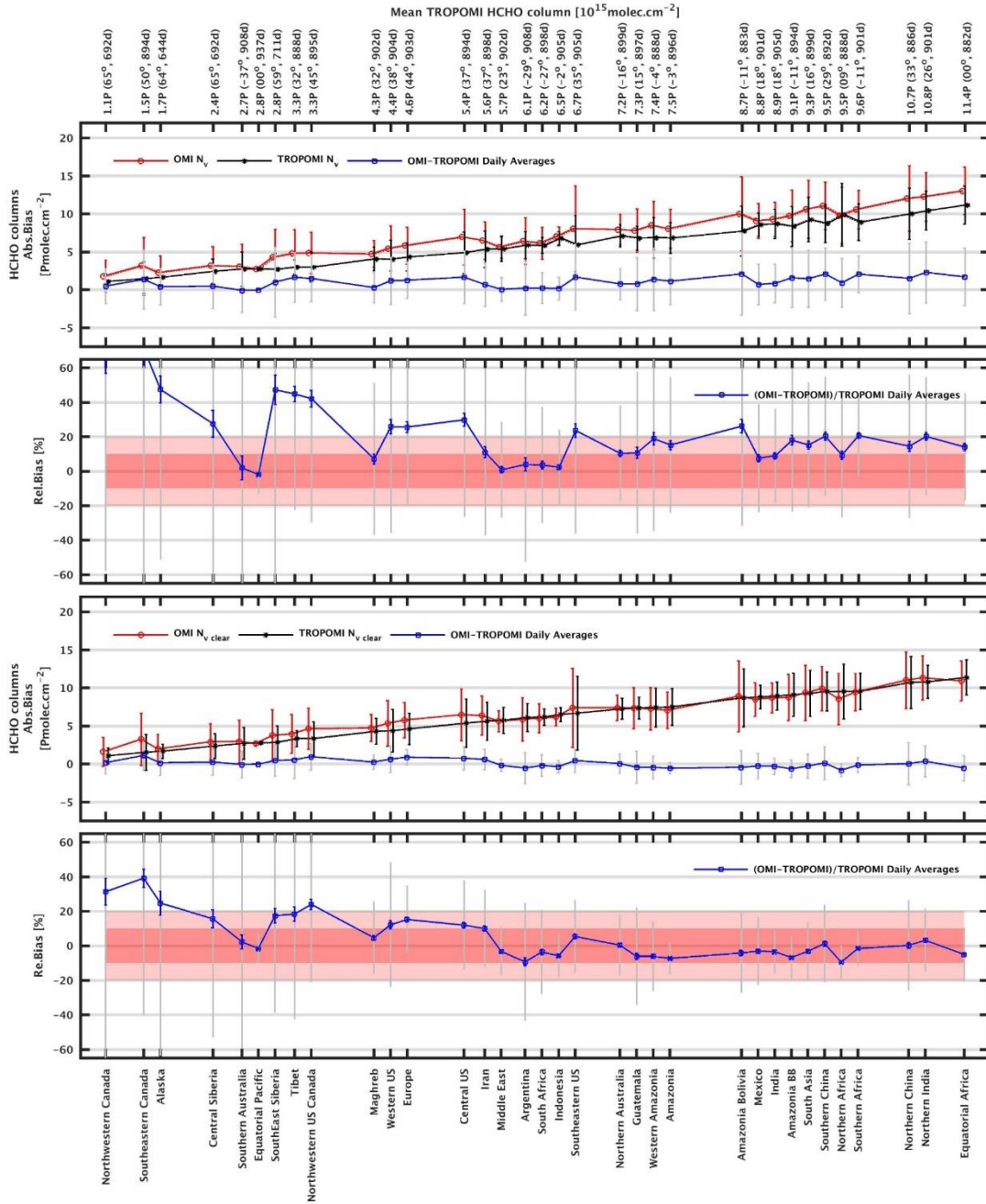
369 **Figure 6: Examples of monthly and yearly averaged HCHO columns ( $N_{v\_clear}$ ) retrieved from OMI (Oct.2004-Dec.2020, in**  
 370 **red) and TROPOMI (2018-Dec.2020, in black) at two different spatial scales selected for the comparison: a large region of**  
 371 **Equatorial Africa, and a circle of 20km-radius over New Delhi in India. Absolute and relative biases between OMI and**  
 372 **TROPOMI HCHO monthly averaged columns are given in inset, as well as the median deviations of the OMI and**  
 373 **TROPOMI averaged columns. [Pmolec.cm<sup>-2</sup> = 1x10<sup>15</sup> molec.cm<sup>-2</sup>].**

374 Figure 7 presents the absolute and relative biases between OMI and TROPOMI HCHO tropospheric columns for all  
 375 regions. Numbers are provided for daily averaged columns applying a cloud correction ( $N_v$ ) or not ( $N_{v\_clear}$ ). Regions  
 376 are sorted as a function of the averaged TROPOMI HCHO column. At this large spatial scale, the regions over  
 377 Equatorial Africa, Northern China and Northern India present the largest annual columns worldwide, with median  
 378 levels larger than  $10 \times 10^{15}$  molec.cm<sup>-2</sup>. Tropical regions in South America, Africa and Asia present elevated levels of  
 379 HCHO as well, with annual averaged columns larger than  $8 \times 10^{15}$  molec.cm<sup>-2</sup>.

380 Looking at  $N_v$  comparisons, it appears that the OMI HCHO columns present a positive bias compared to TROPOMI  
 381 from  $17 \pm 2.5\%$  for the columns larger than  $5 \times 10^{15}$  molec.cm<sup>-2</sup>, to  $30 \pm 5\%$  for the lower columns. This bias exceeds  
 382 50% in Northern latitudes ( $>45^\circ$ ) and low-emissions ( $<2 \times 10^{15}$  molec.cm<sup>-2</sup>) regions of Canada and Alaska. However,  
 383 when comparing  $N_{v\_clear}$ , the biases are strongly reduced below 10% in all regions where the HCHO levels are larger  
 384 than  $5 \times 10^{15}$  molec.cm<sup>-2</sup>, and the TROPOMI columns are found to be slightly larger than OMI on average ( $-3 \pm 1.2\%$ ).  
 385 In mid-Northern-latitudes/moderate emissions ( $2-5 \times 10^{15}$  molec.cm<sup>-2</sup>) regions such as Europe, Central and Western

386 US, North Western Canada, Siberia or Tibet, OMI columns present a remaining bias of about  $15\pm 3\%$ , while in the  
387 regions of Canada and Alaska, a larger bias of about  $+30\pm 7\%$  remains. Note that we observe biases lower than 10%  
388 in the Maghreb and Southern Australia regions, despite their relatively low columns or low latitudes.  
389 We conclude that biases up to 30% related to the cloud correction are observed over Tropical regions where the clouds  
390 are the highest in altitude (Africa, South America, South Asia), and a smaller but systematic effect, up to 15%, is  
391 observed over mid-latitude polluted regions such as China, India, US or Europe. We also note that the differences  
392 between  $N_v$  and  $N_{v\_clear}$  are mainly significant for the OMI HCHO columns. It has been reported that the cloud  
393 pressures retrieved from TROPOMI and from OMI present a bias (OMI clouds are higher in altitude, Compernelle et  
394 al., 2020). This translates into OMI cloud-corrected air mass factors generally smaller than TROPOMI AMFs by 5 to  
395 30%, depending on the cloud altitude, and therefore in a positive bias of the OMI HCHO VCD compared to the  
396 TROPOMI product. It is therefore important to keep in mind that the use of different cloud products may introduce  
397 inconsistencies, which may be resolved by using clear HCHO VCDs ( $N_{v\_clear}$ ).  
398 Figure 8 shows the linear regression between OMI and TROPOMI monthly averaged columns, considering all regions  
399 together. The relation between OMI and TROPOMI is provided for  $N_v$  and  $N_{v\_clear}$ . This shows that switching off the  
400 cloud correction in the OMI and TROPOMI HCHO products allows to significantly improve not only the slope (from  
401 0.87 to 0.92) and the intercept (from 1.52 to  $0.48 \times 10^{15}$  molec.cm<sup>-2</sup>), but also the data scatter, i.e. the Pearson R  
402 correlation (from 0.74 to 0.98). When considering large-scale comparisons, the agreement between OMI and  
403 TROPOMI  $N_{v\_clear}$  is therefore very satisfactory.

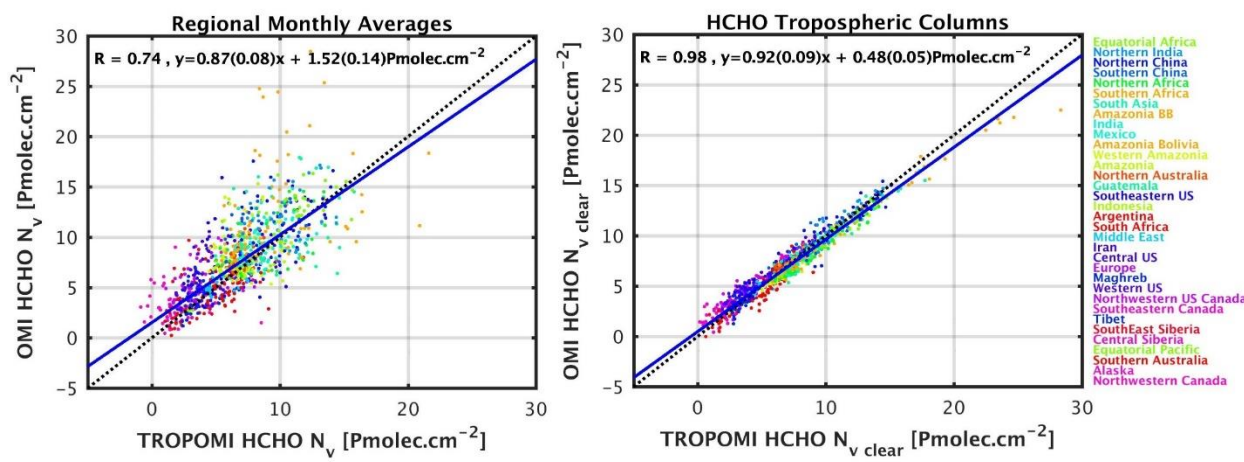
404



405

406 **Figure 7: Absolute and relative biases between OMI and TROPOMI HCHO daily averaged tropospheric columns using**  
 407 **cloud corrected AMF ( $N_v$ , two upper panels) or clear sky AMF ( $N_{v,clear}$ , two bottom panels) for the large regions**  
 408 **represented on Figure 5. Regions are sorted as a function of the median TROPOMI HCHO column. Values of the averaged**  
 409 **HCHO columns are provided on the top axis, as well as the numbers of common days taken for the comparison and the**  
 410 **latitude of the region. The median OMI (red) and TROPOMI (black) columns are plotted together with the absolute**  
 411 **differences (in blue). Error bars represent the median deviations of the columns, or the median absolute deviations of the**

412 differences (MAD, in grey). Statistical ErrB are also plotted for the relative bias (in blue). Pink areas indicate 10% and  
 413 20% bias. [ $\text{Pmolec.cm}^{-2} = 1 \times 10^{15} \text{ molec.cm}^{-2}$ ].



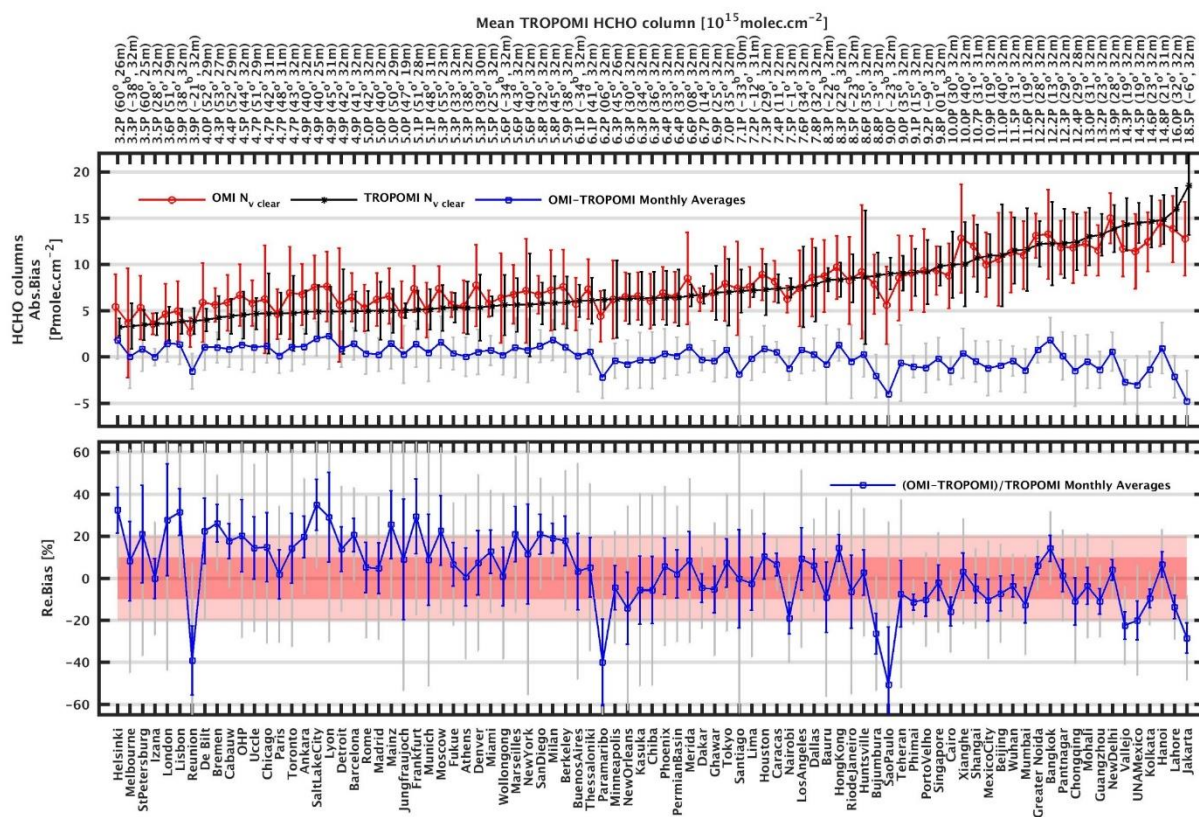
414  
 415 **Figure 8: Scatter plots of OMI versus TROPOMI columns for the monthly means of collocated data. Results are shown for**  
 416  **$N_v$  (left panel) and  $N_{v,clear}$  (right panel). The correlation, slope and intercept of a linear regression using the robust Tei-**  
 417 **Shein estimator are given as inset and plotted as a blue line. Black dotted line is the 1:1 line. The color indicates the latitude**  
 418 **of the region. [ $\text{Pmolec.cm}^{-2} = 1 \times 10^{15} \text{ molec.cm}^{-2}$ ].**

419 When averaging data over large regions, the dispersion due to random uncertainties is greatly reduced compared to  
 420 individual observations. As summarized in Table 2, the median absolute deviations of the monthly averaged columns  
 421 are equivalent for OMI and TROPOMI ( $1.8 \times 10^{15} \text{ molec.cm}^{-2}$ ), while the MAD of their differences are significantly  
 422 lower ( $0.5 \times 10^{15} \text{ molec.cm}^{-2}$ ). This indicates that at this spatiotemporal resolution, the natural variability dominates the  
 423 dispersion of the averaged observations. Looking at the daily averaged columns, the TROPOMI median deviation is  
 424 lower than for OMI (2.2/2.7), but still larger than the MAD of their differences (1.5).

425 The improved spatial resolution of TROPOMI should allow for a better detection of localized HCHO columns. To  
 426 address this question, we performed the same comparisons as for the large regions, but looking at smaller areas of  
 427 20km radius around cities. Figure 9 presents the absolute and relative biases of the monthly averaged HCHO columns  
 428 ( $N_{v,clear}$ ) for a large number of cities. At this spatial scale, Jakarta is the location with the largest median HCHO level  
 429 ( $>18 \times 10^{15} \text{ molec.cm}^{-2}$  over the 2018-2020 period). Indian, Chinese and other Asian cities follow, as well as Mexico,  
 430 Monterrey or Kinshasa ( $>12 \times 10^{15} \text{ molec.cm}^{-2}$ ). Sao Paulo, Tehran and Cairo present also noticeably elevated HCHO  
 431 levels ( $>9 \times 10^{15} \text{ molec.cm}^{-2}$ ). An example over New Delhi is presented on the second panel of Figure 6 and more  
 432 examples can be found in fig.S5.

433 When comparing OMI and TROPOMI  $N_{v,clear}$  around the cities, the same general behaviour as in the large regions  
 434 can be observed. OMI presents a positive bias ( $20 \pm 15\%$ ) compared to TROPOMI for low to medium HCHO levels,  
 435 while for medium to large levels, the agreement is very good on average ( $-1 \pm 10\%$ ). There are nevertheless a few  
 436 exceptions where TROPOMI HCHO columns are significantly larger than the OMI ones. This is the case at La  
 437 Reunion, Paramaribo, Nairobi, Bujumbura, Sao Paulo, Monterrey, Mexico, or Jakarta. Those cities are located along  
 438 marine coasts or lakes, at higher altitude, or are surrounded by mountains. In those cases, the finer spatial resolution  
 439 of TROPOMI clearly improves the detection of the HCHO signal. For most other locations, however, the impact of  
 440 the improved spatial resolution of TROPOMI on the HCHO columns is not detectable in the column magnitudes,

441 when compared to OMI observations. This is likely related to the nature of the HCHO production that mostly is  
 442 secondary from the oxidation of NMVOCs with various lifetimes (Stavrakou et al. 2015; Bauwens et al., 2016). Except  
 443 for regions where the topography presents sharp discontinuities, this causes a natural spread of the HCHO columns at  
 444 a scale larger than the TROPOMI spatial resolution.  
 445 Note however that at this spatial resolution (20km radius), the level of noise is larger than for the regional averages  
 446 and the TROPOMI averaged columns are significantly more stable than the OMI ones, as evidenced by their median  
 447 deviations (see Table 2). On a daily basis, the OMI columns present a dispersion of  $7.8 \times 10^{15}$  molec.cm<sup>-2</sup>, while the  
 448 TROPOMI dispersion is about twice smaller ( $3.7 \times 10^{15}$  molec.cm<sup>-2</sup>). In this case, the MAD of the differences ( $7.1 \times 10^{15}$   
 449 molec.cm<sup>-2</sup>) is dominated by the noise on OMI observations. Note that these estimates still include the natural  
 450 variability of the columns themselves. If an area of 20-km radius in the remote Equatorial Pacific is considered, the  
 451 observations represent constant background values and the seasonal variability is further reduced. In such conditions,  
 452 the dispersion of the OMI daily observations is  $3.5 \times 10^{15}$  molec.cm<sup>-2</sup>, while only  $1 \times 10^{15}$  molec.cm<sup>-2</sup> for TROPOMI.  
 453 We show in the next section that validation with ground-based measurements brings further information on the satellite  
 454 column precision.



456 **Figure 9: Absolute and relative biases between OMI and TROPOMI HCHO monthly averaged tropospheric columns using**  
 457 **clear sky AMF ( $N_{v,clear}$ ) within 20km-radius circles around selected cities, sorted as a function of the median TROPOMI**  
 458 **HCHO column. Value of the averaged HCHO columns are provided on the top axis, as well as the numbers of months taken**  
 459 **for the comparison, and the latitude of the region. The median OMI (red) and TROPOMI (black) columns are plotted**  
 460 **together with the absolute differences (in blue). Error bars represent the median absolute deviations (MAD) of the columns**  
 461 **and of the differences (in grey). Statistical ErrB are also plotted for the relative bias (in blue). Pink areas indicate 10% and**  
 462 **20% bias. [Pmolec.cm<sup>-2</sup> =  $1 \times 10^{15}$  molec.cm<sup>-2</sup>].**

463 **Table 2: Median absolute deviation of the OMI and TROPOMI daily and monthly averaged columns ( $N_{v\_clear}$ ), in large**  
 464 **regions and in 20km-radius area. MAD of differences between OMI and TROPOMI columns are also given in the last**  
 465 **column.**

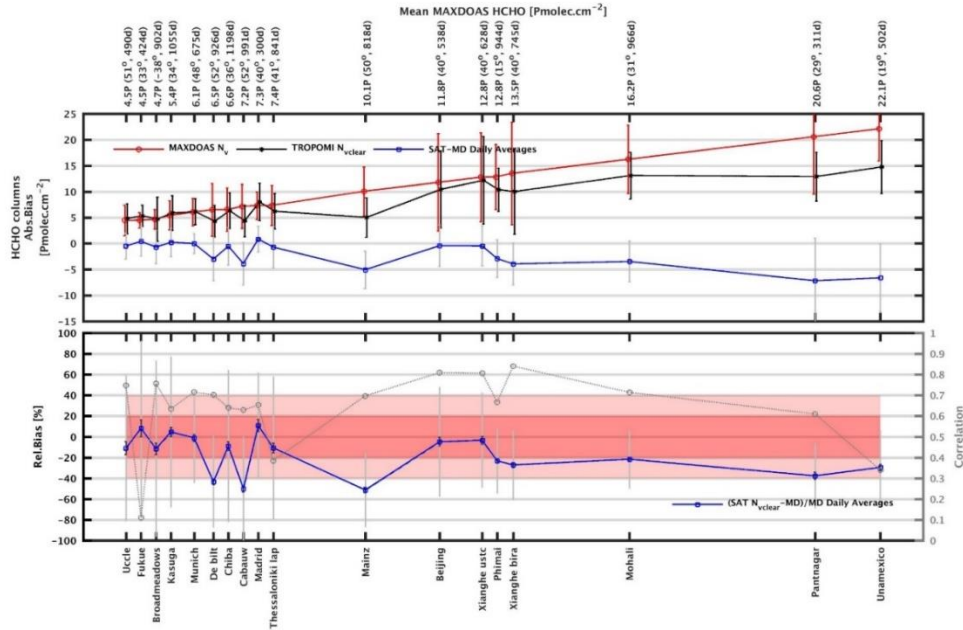
Dispersion	OMI MAD [ $10^{15}$ molec.cm <sup>-2</sup> ]	TROPOMI MAD [ $10^{15}$ molec.cm <sup>-2</sup> ]	OMI-TROPOMI MAD [ $10^{15}$ molec.cm <sup>-2</sup> ]
Monthly Regional	1.8	1.8	0.5
Daily Regional	2.7	2.2	1.6
Monthly 20km	3.3	2.5	2.4
Daily 20km	7.8	3.7	7.1
Daily 20km in the Equatorial Pacific	3.5	1.0	3.7

## 466 5 Validation with a global MAX-DOAS network

467 Here, we present a validation exercise based on a network of 18 ground-based MAX-DOAS instruments. This effort  
 468 complements the study of Vigouroux et al. (2020), which relied on a network of FTIR instruments. Compared to the  
 469 FTIR instruments, the MAX-DOAS provide a higher sensitivity in the boundary layer, where the bulk of HCHO is  
 470 located. The MAX-DOAS network covers stations where the level of HCHO is significant, from medium to very large  
 471 HCHO columns, while the FTIR network includes a larger number of remote stations. In this study, we validate in  
 472 parallel the OMI and TROPOMI datasets. We first focus on a direct comparison of the satellite and MAX-DOAS  
 473 tropospheric columns. The effect of the vertical smoothing is investigated in the next subsection for three stations.

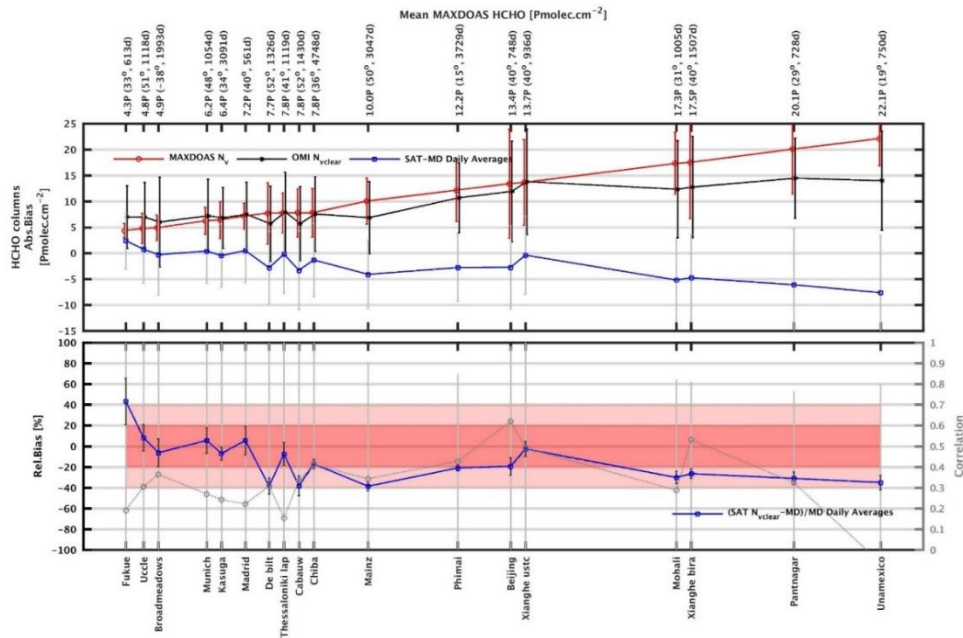
### 474 5.1 Direct comparisons of tropospheric columns

475 For each station in Table 1, we consider daily averages of the satellite columns in a radius of 20km around the  
 476 instruments. We average MAX-DOAS columns between 11h and 16h local time. We keep coincident days of  
 477 observations (OMI/MAX-DOAS, TROPOMI/MAX-DOAS) to obtain daily and monthly comparison pairs. Note that  
 478 the time periods used for the comparison are not the same for OMI and TROPOMI, and vary between the stations. To  
 479 obtain the validation results, we follow the methodology presented in Vigouroux et al. (2020) (see sect. 2.5).



480

481 **Figure 10: Absolute (top, blue line) and relative biases (bottom) between MAX-DOAS and TROPOMI HCHO daily**  
 482 **averaged tropospheric columns in a circle of 20km-radius around the stations. Regions are sorted as a function of the**  
 483 **median MAX-DOAS HCHO column. In the upper plot, the median MAX-DOAS (red) and TROPOMI (black) columns are**  
 484 **plotted together with the differences. Error bars (in grey) represent the median absolute deviations (MAD) of the columns**  
 485 **and of the differences. Statistical ErrB are also plotted for the relative bias (in blue). Pink areas indicate 20% and 40%**  
 486 **bias. The correlation between the daily observations are given in the lower plot (grey circles). [Pmolec.cm<sup>-2</sup> = 1x10<sup>15</sup>**  
 487 **molec.cm<sup>-2</sup>].**



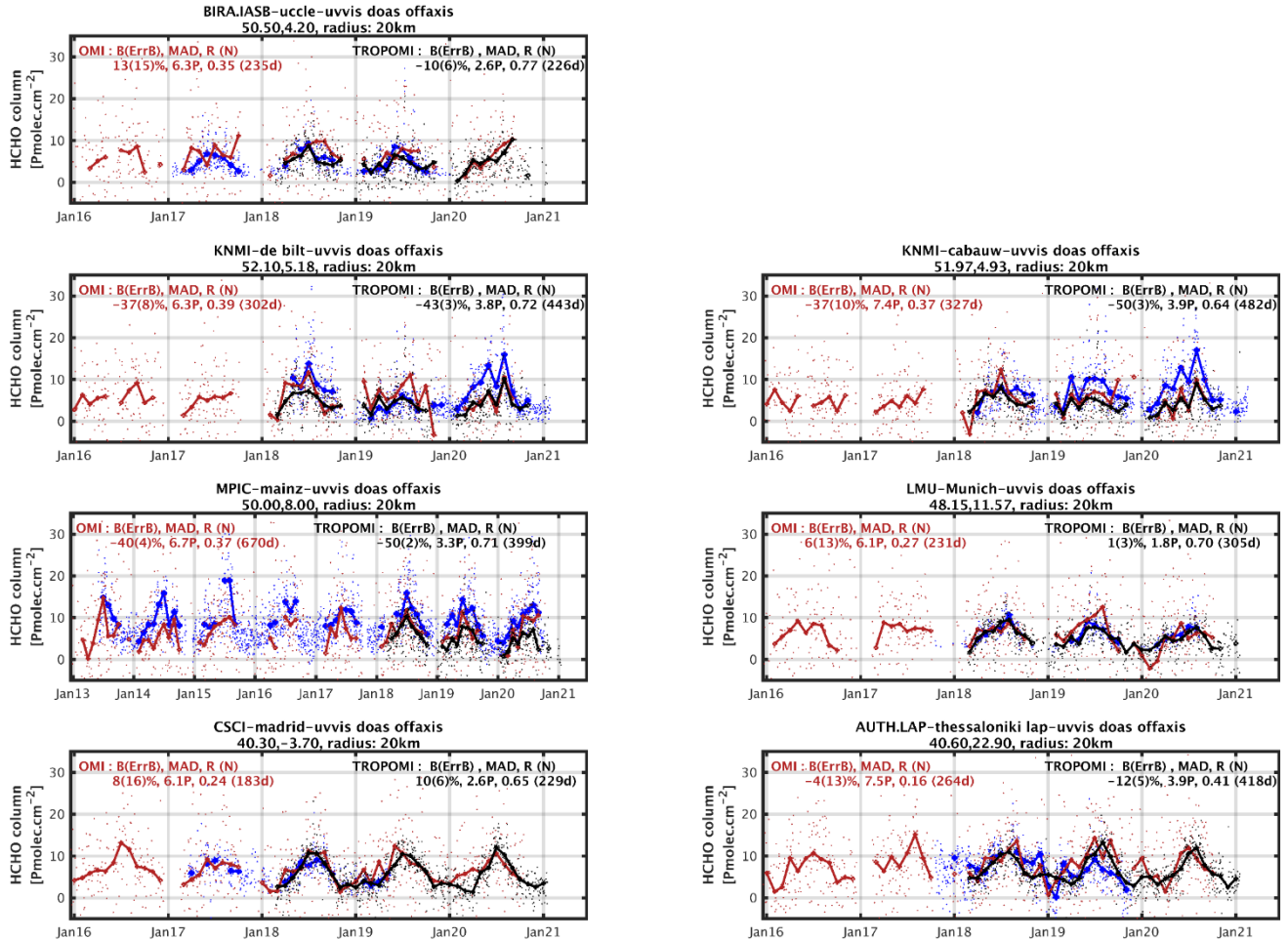
488

489 **Figure 11: same as Figure 10 for MAX-DOAS and OMI HCHO daily averaged.**

490

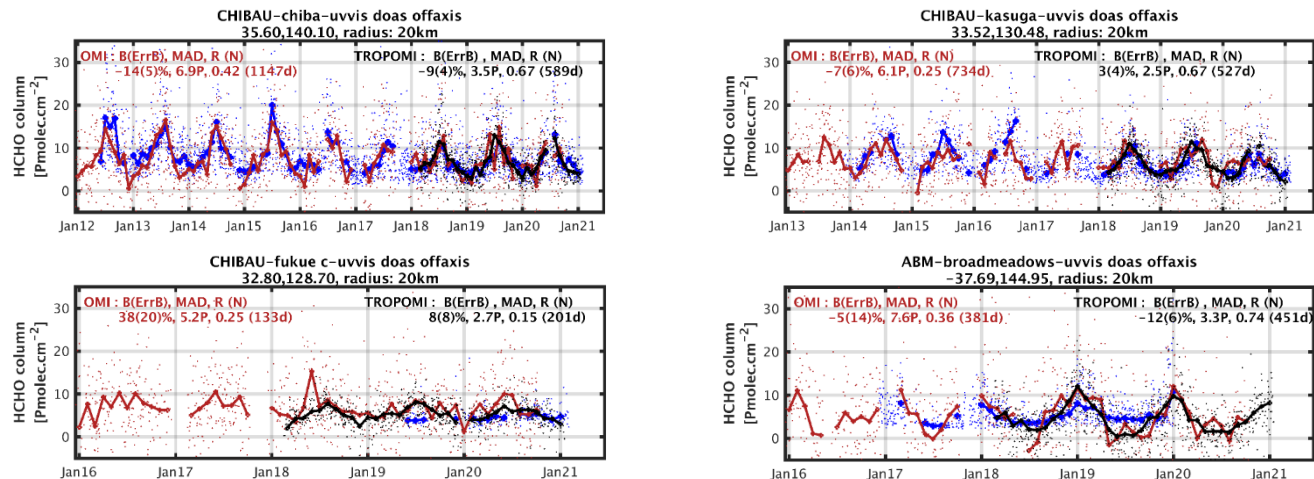
491 Figure 10 and Figure 11 present the absolute and relative biases of the daily averaged columns as a function of the  
492 median MAX-DOAS HCHO column, respectively, for TROPOMI and OMI. A more detailed description for each  
493 station and for individual time series is presented afterwards. The values of the biases are similar for OMI and  
494 TROPOMI, except for the lowest columns in Uccle and Fukue, where OMI presents larger positive biases exceeding  
495 +20%. In agreement with Vigouroux et al. (2020), TROPOMI columns do not present a significant bias for the range  
496 of HCHO levels from 4 to  $8 \times 10^{15}$  molec.cm<sup>-2</sup>. Note that, in contrast to FTIR data, the range of values covered by our  
497 MAX-DOAS network does not extend to columns lower than  $4 \times 10^{15}$  molec.cm<sup>-2</sup>. We observe that the stations in De  
498 Bilt and Cabauw tend to show somewhat stronger negative biases even for medium levels of HCHO, which might  
499 point to a network inhomogeneity. For larger HCHO columns ( $>8 \times 10^{15}$  molec.cm<sup>-2</sup>), and in agreement with the FTIR  
500 results, we observe that negative biases tend to increase for large HCHO columns such that the underestimation of the  
501 satellite columns reaches about -40% for the largest columns. On the upper plot, the error bars represent the median  
502 absolute deviations of the columns and of their differences. It appears clearly that the MADs obtained with TROPOMI  
503 are substantially lower than those obtained with OMI. Note that the type of MAX-DOAS instrument (in particular its  
504 signal-to-noise ratio) may also influence the observed MAD at the different stations.

505 Figure 12, Figure 13 and Figure 14 present more detailed results for the stations in Europe, Japan and Australia, and  
506 China, India, Thailand and Mexico, respectively. On each plot, the time series of the MAX-DOAS, OMI and  
507 TROPOMI data are displayed together. Results of the daily statistical analysis are given as inset. At European stations,  
508 which show medium range HCHO levels, we obtain contrasted results. With a mean HCHO column of  $4.5 \times 10^{15}$   
509 molec.cm<sup>-2</sup>, Uccle is one of the stations with the lowest columns of the network presented in this paper. While OMI  
510 values show a positive bias ( $13 \pm 15\%$ ) and a poor correlation (0.3) with the MAX-DOAS, TROPOMI appears to be  
511 biased low ( $-10 \pm 6\%$ ) but much better correlated (0.82) with the MAX-DOAS data. As opposed to Uccle, the observed  
512 biases in De Bilt, Cabauw, and Mainz are largely negative (from -40% to -50%). The correlations found with  
513 TROPOMI are nevertheless much better than with OMI. Note that the median MAX-DOAS HCHO value in Mainz is  
514 larger than  $10 \times 10^{15}$  molec.cm<sup>-2</sup>, which is quite high for an European site. The results in Munich have been presented  
515 in details in Chan et al. (2020). They are closer to what is found in Uccle, with a small positive bias for TROPOMI  
516 ( $1 \pm 3\%$ ) and for OMI ( $6 \pm 13\%$ ). Similarly in Madrid, OMI and TROPOMI results are very consistent with a mean bias  
517 of respectively  $8 \pm 16\%$  and  $10 \pm 6\%$ . In Thessaloniki, the negative bias is  $-12 \pm 5\%$ , but the correlation is poorer than in  
518 Madrid.



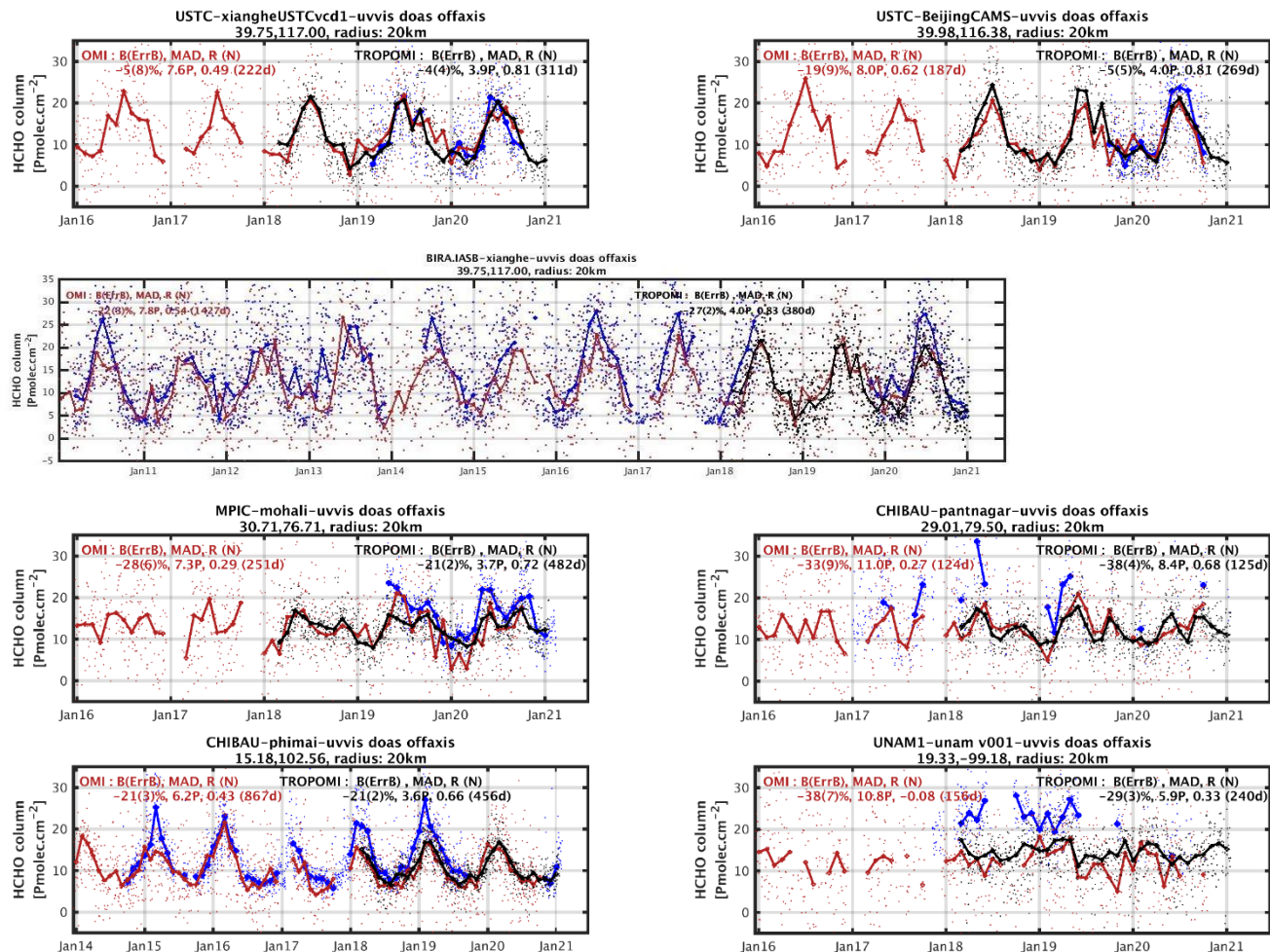
519 **Figure 12: Time series of MAX-DOAS HCHO columns (blue), OMI  $N_{v,clear}$  (red) and TROPOMI  $N_{v,clear}$  (black) at**  
 520 **European sites. Thick lines show monthly median values and dots represent daily median values. Mean relative bias, median**  
 521 **absolute deviations and correlations between the time series are provided for the daily averaged data. [ $\text{Pmolec.cm}^{-2}=10^{15}$**   
 522  **$\text{molec.cm}^{-2}$ ].**

523 In Figure 13, we show three Japanese stations operated by the CHIBA University. Mean HCHO levels in Japan are  
 524 comparable to values found at European sites. In Chiba and Kasuga, TROPOMI and MAX-DOAS columns are  
 525 strongly correlated (about 0.7), but on the island of Fukue the correlation is poor due to a lack of variability at this  
 526 site. At all these sites, TROPOMI shows small biases relative to MAX-DOAS data ( $-9\pm 4\%$  in Chiba,  $3\pm 4\%$  in Kasuga,  
 527  $8\pm 8\%$  in Fukue). The HCHO observations in Broadmeadows, in Northern Melbourne, have been published by Ryan  
 528 et al. (2020). We find a bias of  $-12\pm 6\%$  for TROPOMI and a good correlation of about 0.7. Quite unusually, the  
 529 seasonal amplitude of the MAX-DOAS time series at this station is smaller than observed with OMI and TROPOMI.



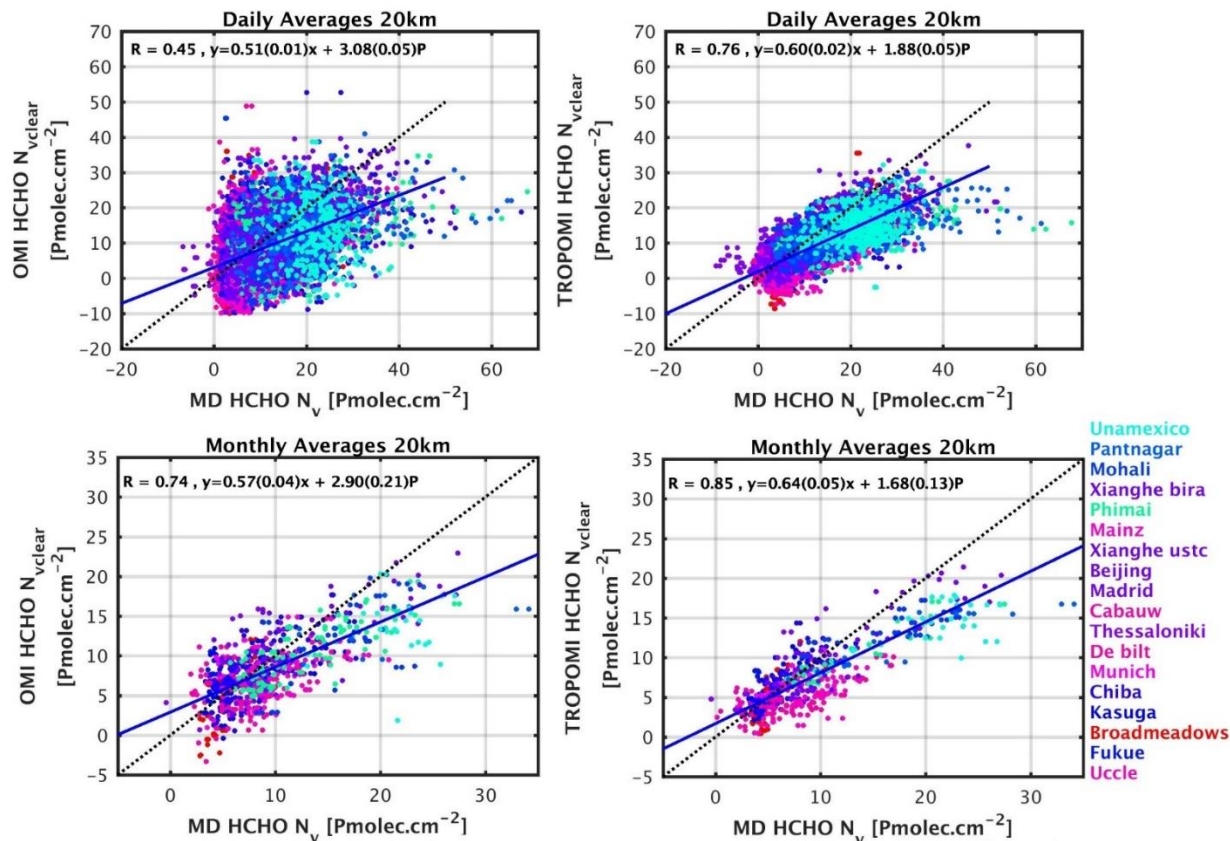
530 **Figure 13: Same as Figure 12 in Japan and Australia.**

531 Stations with large HCHO levels in China, India, Thailand and Mexico are presented in Figure 14. In China, we show  
 532 the results of two instruments in Xianghe, and one instrument in Beijing. With the USTC instruments, we find small  
 533 biases of  $-4\pm 4\%$  and  $-5\pm 5\%$  and correlations larger than 0.8. With the BIRA-IASB instrument in Xianghe, the  
 534 correlation is also excellent. The MAX-DOAS columns are larger than the ones obtained with the USTC instrument,  
 535 and we find a significant negative bias of the TROPOMI data of  $-27\pm 2\%$ . However, this larger bias is in better  
 536 agreement with the results found for equivalent stations in India and with FTIR validation results in Xianghe  
 537 (Vigouroux et al., 2018). This result illustrates the actual uncertainty related to the ground-based measurements  
 538 themselves and the need for further harmonisation of the MAX-DOAS network. Correlations in India and Thailand  
 539 are of about 0.7, while the biases are consistently negative ( $-21\pm 2\%$  in Mohali,  $-38\pm 4\%$  in Pantnagar,  $-21\pm 2\%$  in  
 540 Phimae). The situation is more complex at the UNAM site in Mexico. There, the correlation is poor (0.3), and a  
 541 negative bias of  $-29\pm 3\%$  is found. These results are however more dependent on the radius considered around the  
 542 station, and on the selection of the MAX-DOAS observations (Rivera Cárdenas et al., 2021) (see sect. 5.4).



543 **Figure 14: Same as Figure 12 at Chinese, Indian, Thailand and Mexican sites.**

544 Finally, Figure 15 presents scatter plots of the satellite against MAX-DOAS columns, considering all the stations and  
 545 for daily and monthly comparisons. Table 3 summarizes the validation results. The best agreement is found with  
 546 monthly TROPOMI columns, for which we find a slope of 0.64 and a positive offset of  $1.7 \times 10^{15}$  molec.cm<sup>-2</sup> compared  
 547 to the MAX-DOAS columns. Slopes and biases for the large columns are found to be close for OMI and TROPOMI  
 548 datasets. The improvement with TROPOMI can be seen in the correlation, offset, and bias values obtained for the  
 549 lower columns, as well as in the precision of the daily validation results. On average, the OMI biases are found to be  
 550 statistically non-significant for the lowest columns. When considering monthly averaged data, the correlation between  
 551 MAX-DOAS and satellite columns improves from 0.74 with OMI to 0.85 with TROPOMI (+15%). More importantly,  
 552 it improves from 0.45 to 0.76 when considering daily observations (+68%). The daily offset is reduced by 60% from  
 553 OMI to TROPOMI ( $3.1$  to  $1.9 \times 10^{15}$  molec.cm<sup>-2</sup>). In low-emission conditions, the MADs of the differences provide an  
 554 upper limit of the precision of the satellite measurements. If we consider HCHO levels below  $8 \times 10^{15}$  molec.cm<sup>-2</sup>  
 555 (medium level, but the low range is not represented here), the precision of the daily TROPOMI HCHO observations  
 556 is estimated to be  $3 \times 10^{15}$  molec.cm<sup>-2</sup>, which represents an improvement of more than a factor 2 compared to OMI. The  
 557 precision of monthly TROPOMI observations reaches  $1.4 \times 10^{15}$  molec.cm<sup>-2</sup>, which is close to the Copernicus user  
 558 requirements.



559  
 560 **Figure 15:** Scatter plots of OMI (left) and TROPOMI (right) versus MAX-DOAS data for the daily (top) and monthly  
 561 (bottom) medians of collocated data. The correlation, slope and intercept of a linear regression using the robust Teil-Shein  
 562 estimator is given as inset and plotted as a blue line. The black dotted line is the 1:1 line. The color indicates the latitude of the  
 563 station. . [Pmolec.cm<sup>-2</sup>=10<sup>15</sup> molec.cm<sup>-2</sup>].

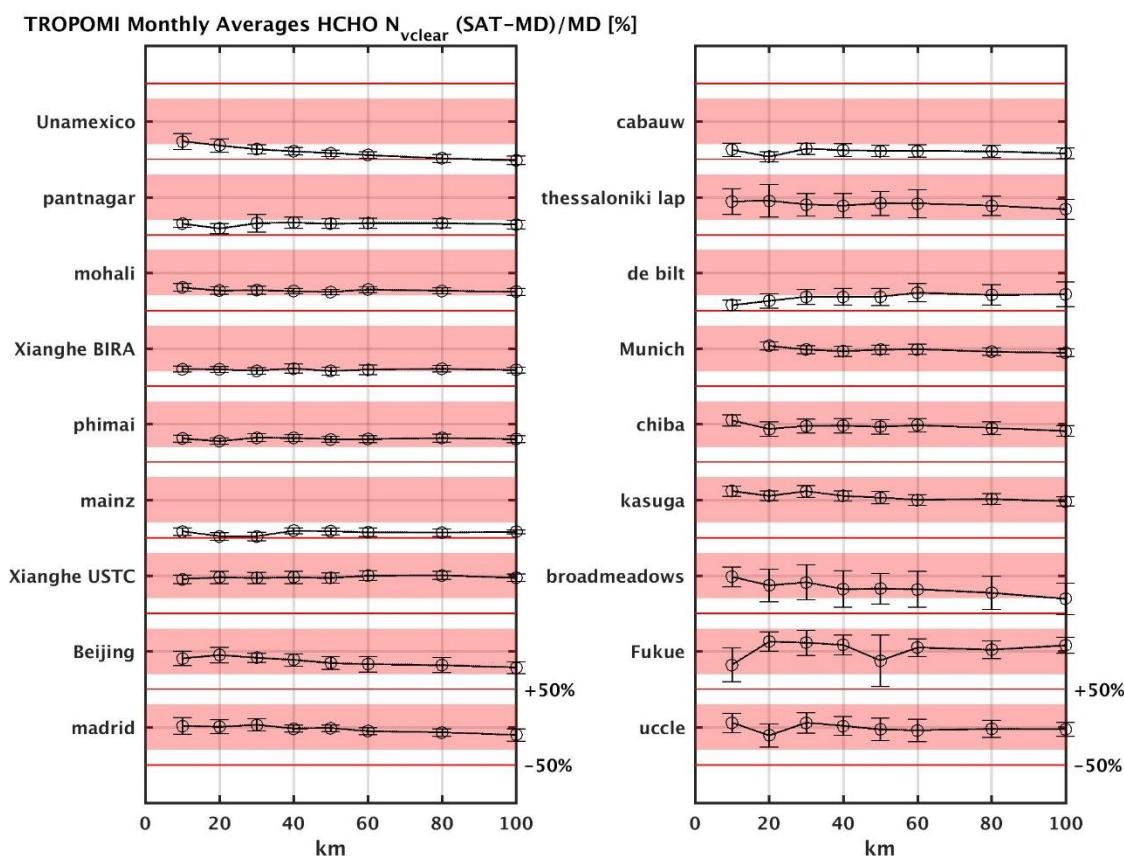
564 **Table 3:** Summary of validation results for OMI and TROPOMI when considering all collocated pairs (daily or monthly  
 565 means) together. Values for HCHO columns lower or larger than 8x10<sup>15</sup> molec.cm<sup>-2</sup> are given in brackets.

	OMI (<, >8x10 <sup>15</sup> molec.cm <sup>-2</sup> )	TROPOMI (<, >8x10 <sup>15</sup> molec.cm <sup>-2</sup> )
<b>Daily</b>		
MAD [10 <sup>15</sup> molec.cm <sup>-2</sup> ]	7.3 (6.7, 7.9)	3.8 (3, 4)
Bias+-ErrB [%]	-18±7.5 (-7±12,-21±6.9)	-11±3.6 (-10±4.6, -25±2.8)
Offset [10 <sup>15</sup> molec.cm <sup>-2</sup> ]	3.1	1.9
Slope	0.51	0.6
Correlation	0.45	0.76
<b>Monthly</b>		
MAD [10 <sup>15</sup> molec.cm <sup>-2</sup> ]	2.6 (2.5, 3.2)	2.3 (1.4, 2.7)
Bias+-ErrB [%]	-9±13 (9±16.6, -24±12)	-12±8.6 (-5±10, -25±5.7)
Offset [10 <sup>15</sup> molec.cm <sup>-2</sup> ]	2.9	1.7
Slope	0.57	0.64
Correlation	0.74	0.85

566 **5.2 Sensitivity tests**

567 We performed a few sensitivity tests, in order to evaluate the robustness of the validation results. First, we have used  
 568 different radii around the stations (from 10 to 100km), in order to detect possible spatial resolution effects. Results are  
 569 presented in Figure 16, for the TROPOMI case. At most stations, the bias shows marginally small dependency on the  
 570 radius. Again, this points to the large natural dispersion of the HCHO columns. We find an important exception at the

571 UNAM station in Mexico, where the bias clearly increases with the radius (-30% at 10km, -50% at 100km). At this  
 572 location, the correlation and MADs are also improved at 10km (not shown). In Beijing and Broadmeadows, we do  
 573 observe an increase of the bias at 100km resolution, but the values at 10 and 20km are mostly equivalent. We  
 574 performed the same test with OMI, and found consistent results, except that the lower sampling does not allow using  
 575 a 10km-radius area.



576  
 577 **Figure 16: Median monthly bias as a function of the radius taken around the validation sites. Pink areas indicate 40%**  
 578 **bias.**

579 We also evaluated the impact of clouds using two further tests: (1) compare the daily TROPOMI validation results for  
 580  $N_v$  and  $N_{v\_clear}$ , (2) use a much stricter cloud filter on cloud radiance fractions (CRF) of 20% instead of 60%  
 581 (equivalent to an effective cloud fraction of 10% instead of 40%). With this strict cloud filter, there is no difference  
 582 between  $N_v$  and  $N_{v\_clear}$ . Results are summarized in Table 4. These tests indicate that the TROPOMI HCHO  
 583 validation results do not change significantly when a cloud correction is applied, although the  $N_{v\_clear}$  results are  
 584 slightly better. Using a more stringent cloud filter reduces the number of observations. The bias for the lowest columns  
 585 becomes positive (from -10 to +3%), and the offset is increased (from  $1.9$  to  $2.6 \times 10^{15}$  molec. $\text{cm}^{-2}$ ), while the negative  
 586 bias for the largest columns remains equivalent. These numbers will have to be re-evaluated using only the version 2  
 587 of the TROPOMI level 2 products available since July 2020, when enough data will be available. However, we note  
 588 that this limited impact of the cloud correction on the HCHO columns appears to be consistent with previous satellite

589 datasets, independently of the cloud product, as already observed with GOME-2 and OMI, using version 1 of the O2–  
 590 O2 cloud product (De Smedt et al., 2015).

591 **Table 4: Summary of daily validation results for TROPOMI when considering all collocated pairs when using  $N_{v\_clear}$**   
 592 **(first column), (1) when using  $N_v$  (second column) or (2) when using a strict cloud filter (third column).**

	<b>TROPOMI <math>N_{v\_clear}</math></b> ( $<, >8 \times 10^{15}$ molec.cm $^{-2}$ )	<b>TROPOMI <math>N_v</math></b> ( $<, >8 \times 10^{15}$ molec.cm $^{-2}$ )	<b>TROPOMI <math>N_{v\_clear}</math> CRF&lt;20%</b> ( $<, >8 \times 10^{15}$ molec.cm $^{-2}$ )
<b>Daily</b>			
MAD [10 $^{15}$ molec.cm $^{-2}$ ]	3.8 (3, 4)	3.9 (3, 4.4)	3.3 (2.6, 3.9)
Bias+-ErrB [%]	-11±3.6 (-10+-4.6, -25±2.8)	-14±-3.9 (-12±4.4,-29±2.9)	-3±4.6 (3±6.1, -27±3.8)
Offset [10 $^{15}$ molec.cm $^{-2}$ ]	1.9	1.8	2.6
Slope	0.6	0.56	0.57
Correlation	0.76	0.74	0.75

### 593 5.3 Effect of vertical smoothing

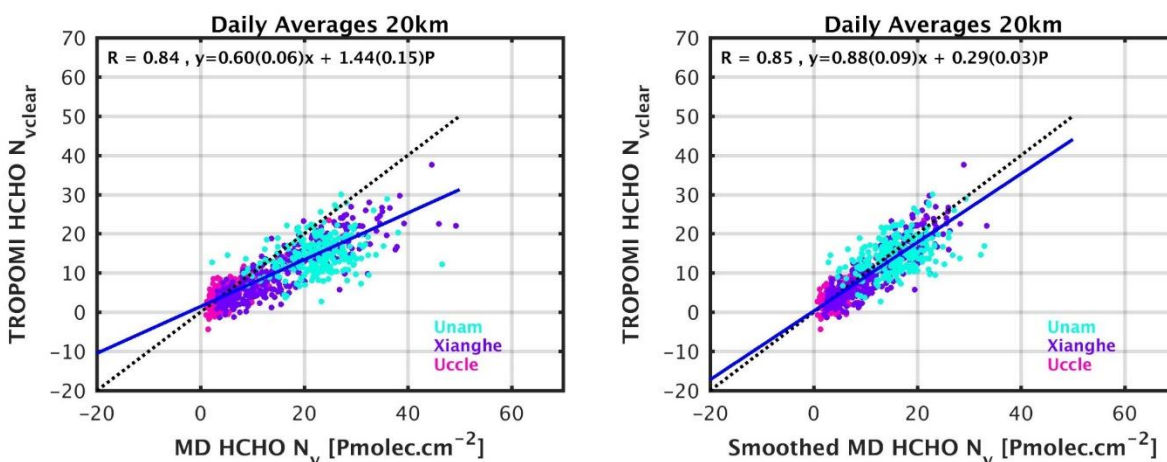
594 Three MAX-DOAS stations (Uccle, Xianghe BIRA-IASB, and UNAM) provide retrieved and a priori vertical profiles  
 595 together with corresponding averaging kernels (GEOMS format). This allows taking into account the different vertical  
 596 sensitivity of MAX-DOAS and TROPOMI measurements when making comparisons. We follow the methodology  
 597 from Rodgers and Connor (2003) described in detail in Vigouroux et al. (2020). It consists of two steps: first taking  
 598 into account the different a priori profiles used to retrieve these two data sets (Eq. 2 of Vigouroux et al., 2020), then  
 599 smoothing the ground-based profiles using TROPOMI averaging kernels (Eq. 3 of Vigouroux et al., 2020).

600 We give in Table 5 the MAD and biases obtained before and after application of the methodology, for the daily mean  
 601 comparisons. Note that the numbers at each site are slightly different than the ones obtained in sect. 5.1 (Figs. 5.3 and  
 602 5.5) because the collocated pairs are constructed slightly differently: each collocated pixel of the satellite must be  
 603 compared to MAX-DOAS before the daily average because the TROPOMI averaging kernel differs for each pixel.

604 We see in Table 5 that at the cleanest site (Uccle) the effect of the smoothing is small, while at the more polluted sites  
 605 Xianghe and UNAM, the biases are strongly reduced by about 20%. This result is in agreement with previous MAX-  
 606 DOAS validation studies (De Smedt et al., 2015; Wang et al., 2019b), but also with aircraft and regional model  
 607 comparisons (Zhu et al., 2020; Su et al., 2020). The effect of the smoothing is also clearly seen in Figure 17 where the  
 608 scatter plots of daily comparisons between TROPOMI and MAX-DOAS are shown before and after vertical  
 609 smoothing. The strong effect of the smoothing is usually not observed with FTIR comparisons because TROPOMI  
 610 and FTIR measurements have similar vertical sensitivity, which rapidly drops in the atmospheric layers lower than  
 611 3km (Vigouroux et al., 2020), while the MAX-DOAS shows an opposite sensitivity that is maximum at the surface  
 612 and generally becomes negligible above 3km (Vigouroux et al., 2008; De Smedt et al., 2015; Wang et al., 2019a). An  
 613 illustration of typical averaging kernels for OMI, TROPOMI and the MAX\_DOAS instrument in Xianghe is provided  
 614 in Figure S6. As the observation angles and overpass times are very close for OMI and TROPOMI, their measurements  
 615 come with a similar vertical sensitivity. This highlights the importance of taking into account the different a priori  
 616 profiles and averaging kernels when comparing techniques having different vertical sensitivity.

617 **Table 5: Effect of a priori substitution and vertical smoothing on the daily comparisons of TROPOMI and MAX-DOAS**  
 618 **data.**

Daily	Direct comparisons		Rodgers and Connor (2003) applied (a priori substitution and smoothing)	
	MAD [10 <sup>15</sup> molec.cm <sup>-2</sup> ]	BIAS ± Err_B [%]	MAD [10 <sup>15</sup> molec.cm <sup>-2</sup> ]	BIAS ± Err_B [%]
Uccle	2.4	-9.4 ± 5.8	2.4	-10.6 ± 5.5
Xianghe, BIRA	3.9	-32.2 ± 2.5	2.7	-9.1 ± 3.0
UNAM	6.1	-34.3 ± 3.2	5.8	-5.8 ± 5.7
	Scatter plot 3 sites		Scatter plot 3 sites	
Offset [10 <sup>15</sup> molec.cm <sup>-2</sup> ]	1.44		0.29	
Slope	0.60		0.88	
Correlation	0.84		0.85	

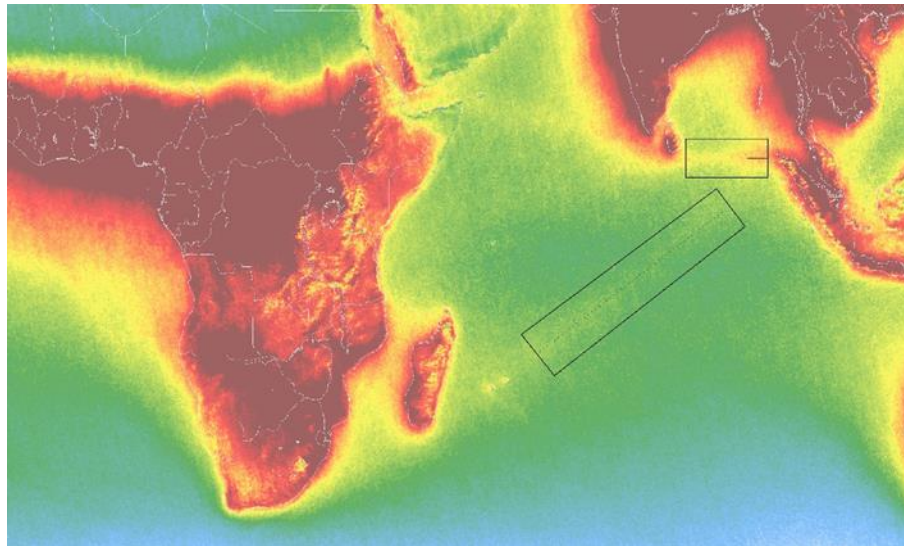


619

620 Figure 17: Scatter plots of TROPOMI versus MAX-DOAS data for the daily means of collocated data before (left) and  
621 (right) vertical smoothing of the MAX-DOAS profile in Uccle, Xianghe and UNAM/Mexico. The correlation, slope and  
622 intercept of a linear regression using the robust Teil-Shein estimator is given inset and plotted as a blue line. The black  
623 dotted line is the 1:1 line. [Pmolec.cm<sup>-2</sup>=10<sup>15</sup> molec.cm<sup>-2</sup>].

## 624 6 Detection of weak HCHO columns over shipping lanes

625 As shown above, TROPOMI HCHO observations feature an unprecedented level of precision allowing for an  
626 improved detection of small columns at short time scales. Here, we present a case study to illustrate the ability of  
627 TROPOMI to detect small HCHO signals related to shipping emissions. When inspecting TROPOMI maps averaged  
628 over several months, weak lines of HCHO columns become visible over the background, especially in the Indian  
629 Ocean (see e.g. Figure 5). This becomes even clearer when saturating the continental HCHO columns by setting a  
630 lower maximum scale, as in Figure 18, which shows HCHO columns seasonally averaged over the months December,  
631 January and February between 2018 and 2021.



632

633

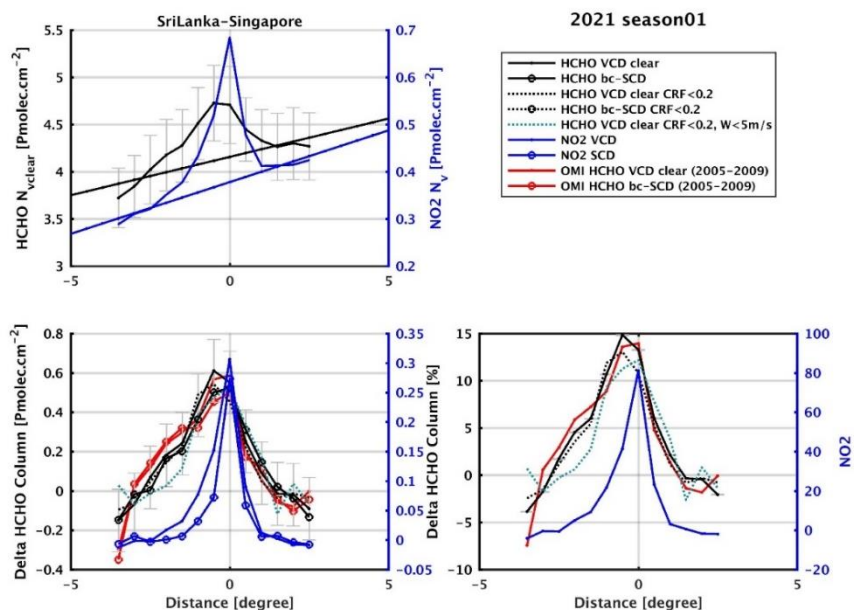
634 **Figure 18: Seasonal DJF map of TROPOMI HCHO tropospheric columns between Dec. 2018 and Feb.2021, on a spatial**  
 635 **grid of  $0.05^\circ$  in latitude and longitude. Observations are only filtered using the provided  $qa\_values > 0.5$ . (max.scale:  $8 \times 10^{15}$**   
 636 **molec.cm<sup>-2</sup>).**

637 The detection of shipping emissions with satellite observations has often been reported for  $NO_2$  (see for example  
 638 Beirle et al., 2004; Richter et al., 2004; 2011; Boersma et al., 2015; Georgoulias et al., 2020), and more recently also  
 639 for  $SO_2$  based on OMI measurements (Theys et al., 2015). In the case of HCHO, however, only one study pointed to  
 640 the identification of a shipping lane signal detected in a 7-year average of ERS-2 GOME data in the ship track corridor  
 641 from Sri Lanka to Singapore (Marbach et al., 2009).

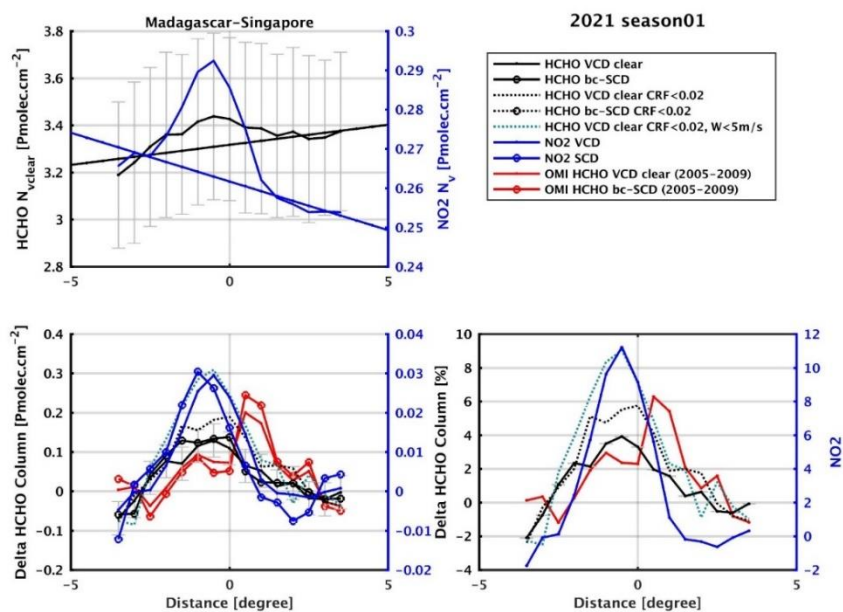
642 Here, we study two lines (1) from Sri Lanka to Singapore and (2) from Madagascar to Singapore. We perform an  
 643 analysis and several sensitivity tests in order to gain confidence and information on the enhanced HCHO. As illustrated  
 644 in the first panel of Figure 19 (line 1) and Figure 20 (line 2), in each box, we average the HCHO columns along the  
 645 ship track to obtain a spatial cross section, and we bin the data as a function of the distance from the line (distances  
 646 are expressed in degrees per  $0.5^\circ$  bin). The background level is not constant, for example due to continental outflow  
 647 in the Bay of Bengal, and needs to be removed. To do so, we fit a straight line through the column values at the edges  
 648 of the box and subtract this line from the signal. This allows to isolate a differential column and to evaluate its absolute  
 649 and relative magnitude compared to the background (respectively shown in the second and third panels of Figure 19  
 650 and Figure 20). For comparison, we perform the same analysis using TROPOMI  $NO_2$  tropospheric columns from the  
 651 operational product ( $NO_2$  ATBD, Van Geffen et al., 2020). Although only about half as wide, the localisation of the  
 652  $NO_2$  peak is found to be well aligned with the HCHO signal. Along the line from Sri Lanka to Singapore, we find a  
 653 similar column enhancement and plume width as in Marbach et al. (2009).

654 In order to exclude a possible indirect AMF effect caused by the TM5 a priori profiles, the same analysis is done based  
 655 on background-corrected slant columns (bc-SCD). We also restrict the analysis to clear sky observations, by using a  
 656 strict cloud filtering of  $CRF < 20\%$ . Furthermore, we use the wind vector information provided in the TROPOMI L2  
 657 product from version 2 onwards (from August 2020), to select only clear-sky observations with low wind conditions

658 (qa>0.5, CRF<20%, W<5m/s). Finally, we add to the analysis a climatology of HCHO observations based on OMI  
 659 measurements (2005-2009).

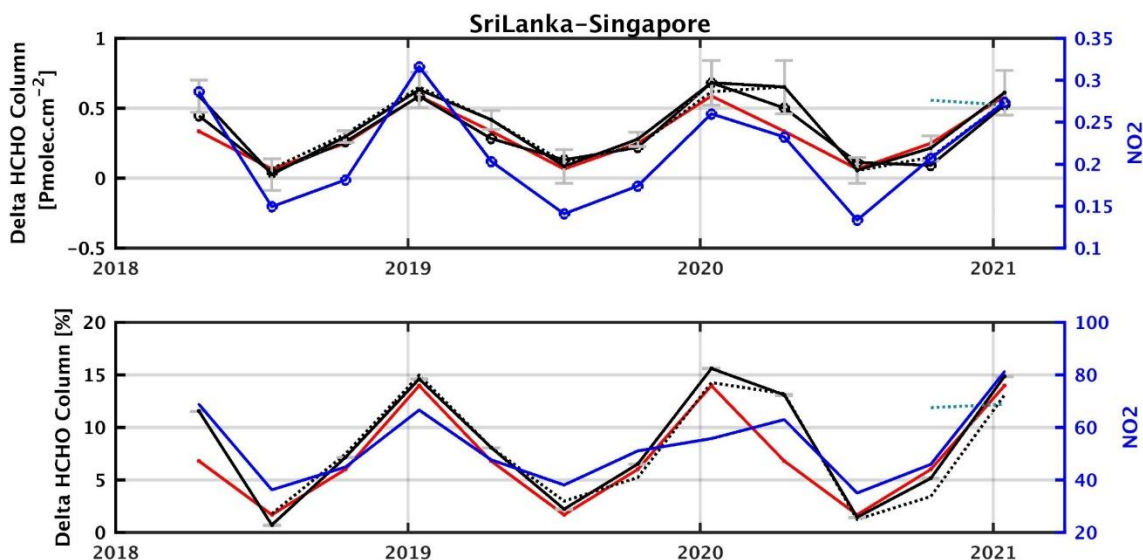


660  
 661 **Figure 19: Box average for the first selected line between Sri Lanka and Singapore between Dec. 2020 and Feb. 2021. The**  
 662 **x-axis represents the distance (south-north) in degrees from the shipping lane. The first panel shows the HCHO (in black)**  
 663 **and NO<sub>2</sub> (in blue) tropospheric columns, binned per distance from the line center. The fitted lines are used to remove the**  
 664 **background contribution. The two bottom panels present the absolute (left) and relative (right) column deviations from**  
 665 **the background line. The analysis is performed on the slant and the vertical columns (circles/lines), using a stricter cloud**  
 666 **filtering (CRF<20%, black dotted line), an additional filter on the wind velocity (W<5m/s, green dotted line), and finally on**  
 667 **OMI observations averaged between 2005 and 2009 (red). [Pmolec.cm<sup>-2</sup> = 1x10<sup>15</sup> molec.cm<sup>-2</sup>].**

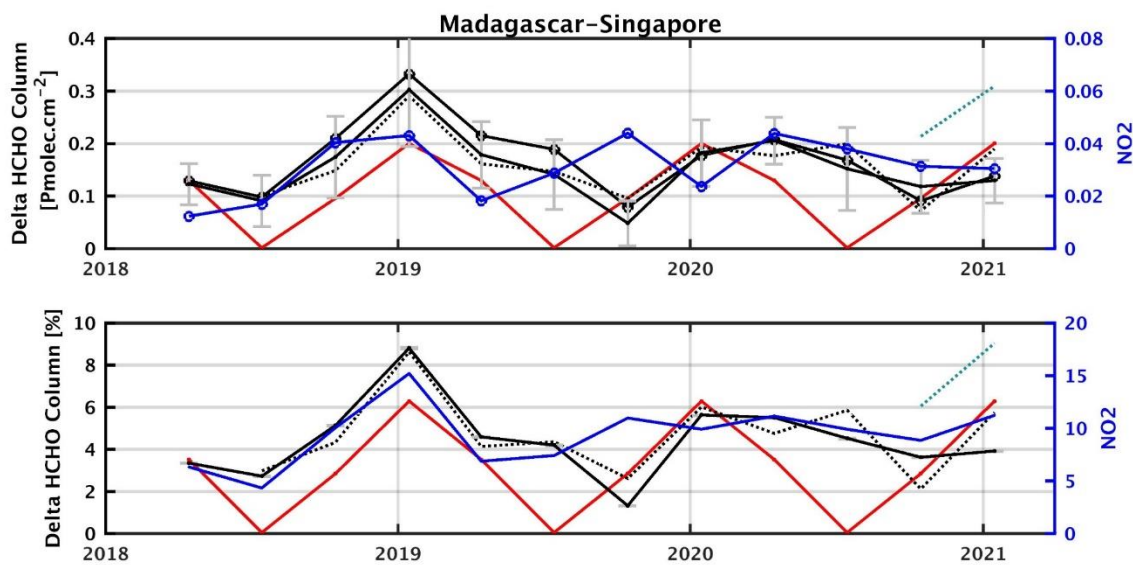


668  
 669 **Figure 20: Same as Figure 19 for the second selected line between Madagascar and Singapore.**

670 Using this approach, we analysed HCHO datasets for each season between MAM 2018 and DJF 2021. The absolute  
 671 and relative magnitude of the largest detected signal is plotted as a function of the season in Figure 21 and Figure 22.  
 672 Along the two lines, the signal is detected in the slant columns of HCHO and NO<sub>2</sub> as well. This excludes the possibility  
 673 of an artefact coming from the TM5 a priori profiles. The signal remains detectable in clear-sky observations, and is  
 674 even increased along the second line. We observe a similar effect of the wind speed filtering (last two seasons).  
 675 Selecting only low-wind conditions clearly enhances the signal along line 2, and during SON along line 1. The  
 676 magnitude of the detected HCHO signal is larger along line 1 (from 0.2 to 0.7x10<sup>15</sup> molec.cm<sup>-2</sup>, 15%) compared to  
 677 line 2 (from 0.1 to 0.3x10<sup>15</sup> molec.cm<sup>-2</sup>, 8%). We find that the absolute magnitude of the HCHO signal is larger than  
 678 the NO<sub>2</sub> signal by a factor of 3 to 10, but the relative increase of the NO<sub>2</sub> columns is significantly larger: 60% along  
 679 line 1 and 15% along line 2. Both lines show a clear seasonality, particularly in the HCHO columns, with a maximum  
 680 during the DJF seasons seen in the OMI climatology and in the TROPOMI 3-months averages. The HCHO signal  
 681 presents a clear drop in JJA along line 1. This is related to the wind direction and strength, which bring the line signal  
 682 closer to the HCHO continental outflow, making its detection more difficult. The OMI data need to be averaged over  
 683 several years in order to detect a significant signal. While the first line is well detected in the 5-year OMI climatology,  
 684 the second line presents a smaller magnitude, a larger variability, and cannot be detected in the most recent years of  
 685 OMI measurements.



686  
 687 **Figure 21: Seasonal variation of the absolute (top panel) and relative (center panel) column deviations of the TROPOMI**  
 688 **HCHO (black), OMI 2005-2009 climatology HCHO (red) and TROPOMI NO<sub>2</sub> (blue) tropospheric columns along the Sri**  
 689 **Lanka – Singapore line. For each season, the maximum deviation compared to the background is provided. The results of**  
 690 **the analysis are given for the slant and the vertical columns (circles/lines), using a stricter cloud filtering (CRF<20%, black**  
 691 **dotted line), an additional filter on the wind velocity (W<5m/s, green dotted line). [Pmolec.cm<sup>-2</sup> = 1x10<sup>15</sup> molec.cm<sup>-2</sup>].**



692

693 **Figure 22: Same as Figure 21 along the Madagascar – Singapore line.**

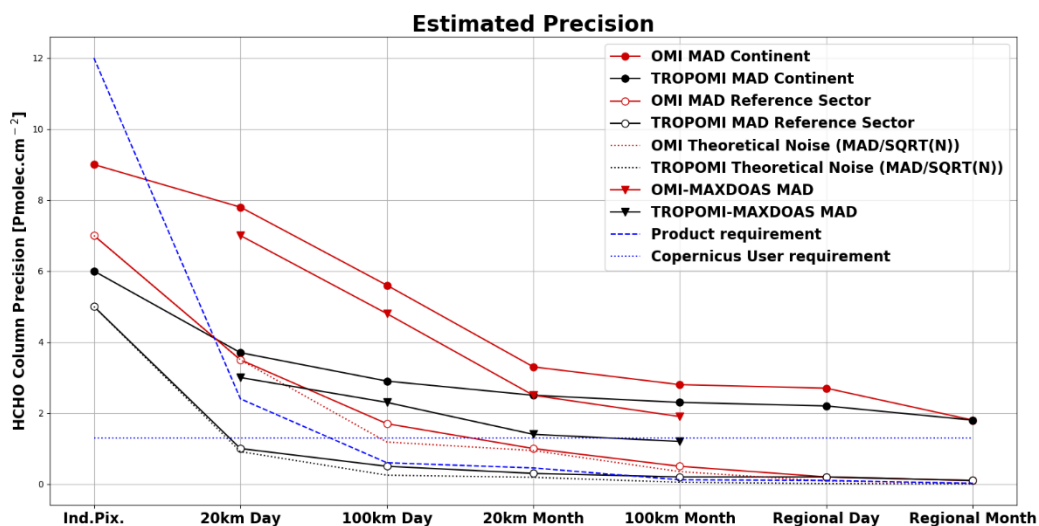
694 Using TROPOMI HCHO observations averaged over 3 months, it is therefore possible to detect a signal as small as  
 695  $0.1 \times 10^{15} \text{ molec.cm}^{-2}$  (with a median deviation of  $0.03 \times 10^{15} \text{ molec.cm}^{-2}$ ), after removal of the background contribution.  
 696 Note that along the first line a similar analysis can also be performed on a monthly basis. While we show several  
 697 evidences that the signal is related to shipping emissions, its source is not studied here. As discussed in Marbach et al.  
 698 (2009) it could be due to secondary HCHO production via the atmospheric oxidation of NMVOCs emitted from ship  
 699 engines but also to enhanced  $\text{CH}_4$  oxidation by elevated levels of OH radicals within the ship plumes. Model analysis  
 700 suggests that the second hypothesis is the main factor responsible for the elevated HCHO levels (Song et al., 2010).  
 701 Other HCHO lines can be detected as well in the Tropics, although weaker in magnitude or closer to the continental  
 702 outflow (in the South-West of Africa or in the West of India). More advanced techniques to separate the signal from  
 703 the background and to account for wind dispersion effects could help in detecting more shipping lanes but also weak  
 704 continental emissions (Beirle et al., 2004).

705 **7 Conclusions**

706 Owing to its high spatial resolution resulting in many measurement points, coupled with an improved signal to noise  
 707 ratio at single pixel level, TROPOMI allows to monitor HCHO tropospheric columns from space with an  
 708 unprecedented definition. The global and regional maps show a clear reduction of the noise compared to previous  
 709 sensors, allowing for the detection of weaker HCHO signals, and the monitoring of HCHO variations on a much  
 710 shorter time scale.

711 We have evaluated the TROPOMI HCHO operational product against the QA4ECV OMI HCHO dataset, and against  
 712 a network of 18 ground-based MAX-DOAS instruments. The gain in precision at different spatial and temporal scales  
 713 was estimated by (1) comparing the median deviation of the averaged columns, and (2) validating the data using  
 714 MAX-DOAS column network measurements. Both methods include additional noise components from temporal

715 variation, spatial variation and ground-based column precision. Results are summarized in Figure 23 where precision  
 716 estimates are provided for observations over regions with enhanced continental emissions and for background  
 717 conditions, as a function of the time resolution (daily or monthly averages) and of the spatial resolution (from 20km  
 718 to regional scale). At 20 and 100km resolution, both the median deviation approach and the validation results lead to  
 719 very consistent estimates of the precision. The theoretical noise is also represented in the figure; it decreases as the  
 720 squared root of the number of observations included in the averages. In remote conditions, the median deviation of  
 721 the averaged columns follows closely the theoretical noise until reaching a threshold. If we consider a large region in  
 722 the reference sector, all estimates converge towards a limit of about  $0.2 \times 10^{15} \text{ molec.cm}^{-2}$  (day) to  $0.1 \times 10^{15} \text{ molec.cm}^{-2}$   
 723 (month) both for OMI and TROPOMI. Over continental emission sources, the reduction of the noise is  
 724 counterbalanced by the HCHO natural variability and by other sources of pseudo-noise which depend on the spatial  
 725 and temporal scales of the observations. The largest improvement brought by TROPOMI is found for daily  
 726 observations at 20km resolution, for which a gain in precision by a factor of 3 is obtained compared to OMI. The  
 727 product and COPERNICUS user requirements for precision are also represented in the figure. Both are reached with  
 728 TROPOMI using daily averaged data at the resolution of 20km if we consider the dispersion in remote regions.  
 729 However, over continental emissions, local variability effects added up to the estimated precision that reaches a  
 730 threshold of about  $2 \times 10^{15} \text{ molec.cm}^{-2}$ .



731  
 732 **Figure 23: Estimated precision of OMI (in red) and TROPOMI (in black) HCHO columns at different spatial and temporal**  
 733 **scales (20km, 100km, regions, day/month). The median deviation of the satellite HCHO columns are provided for**  
 734 **continental emissions (plain circles) and in the remote reference sector (white circles). Validation estimates are plotted at**  
 735 **20km and 100km (MAD of differences between satellite and MAX-DOAS columns, triangles). The theoretical noise (dotted**  
 736 **lines) corresponds to single measurement precision divided by the square root of observations. The dashed blue line is the**  
 737 **TROPOMI product requirement, based on a single measurement precision of  $12 \times 10^{15} \text{ molec.cm}^{-2}$ . The horizontal blue line**  
 738 **at  $1.3 \times 10^{15} \text{ molec.cm}^{-2}$  represents the COPERNICUS user requirement. [ $\text{Pmolec.cm}^{-2} = 1 \times 10^{15} \text{ molec.cm}^{-2}$ ].**

739 For the HCHO absolute values, we show that OMI and TROPOMI observations agree very well for moderate to large  
 740 HCHO levels (columns larger than  $5 \times 10^{15} \text{ molec.cm}^{-2}$ ) for which the bias between both datasets is smaller than 10%.  
 741 For lower columns however, OMI observations present a remaining bias of about +20% compared to TROPOMI. This  
 742 good agreement is obtained by considering vertical columns calculated with air mass factors not corrected for cloud

743 effects (clear VCD). This allows to avoid biases related to differences in the cloud products. For all applications that  
744 require combining the OMI and TROPOMI observations for low to moderate cloud fractions, we therefore advise to  
745 use clear VCDs. Validation results confirm the good agreement between the OMI and TROPOMI datasets and a  
746 similar underestimation of both products in the highest range of the HCHO levels (-25% in average for columns larger  
747 than  $8 \times 10^{15}$  molec.cm<sup>-2</sup>). For medium columns, OMI presents a slight overestimation compared to MAX-DOAS data,  
748 which is not observed for TROPOMI. Sensitivity tests show that validation results obtained with the TROPOMI  
749 HCHO columns are weakly dependent on the cloud correction. They also depend weakly on the radius considered  
750 around the station, with a few exceptions such as Mexico city or coastal stations. On the contrary, the vertical  
751 smoothing (tested at three stations) has a strong effect on the comparison with MAX-DOAS. After taking into account  
752 the different a priori profiles and averaging kernels, the bias for large HCHO columns is strongly reduced by about  
753 20%.

754 Comparing OMI and TROPOMI monthly averaged HCHO columns, we do not observe significant differences related  
755 to the spatial resolution, except in regions surrounded by natural boundaries where the benefit of the finer spatial  
756 resolution of TROPOMI is clearly apparent. The weak sensitivity to the spatial resolution of HCHO measurements  
757 can be understood when considering that HCHO is a secondary product from the degradation of NMOVCs with  
758 various lifetimes, which results in a general spread of the HCHO spatial distributions. The large number of TROPOMI  
759 observations allows to perform validation at a resolution as small as 10km on a daily basis with a sufficient precision,  
760 which is not possible with OMI. It is clear that TROPOMI brings a significant improvement in the temporal resolution  
761 of the observations. At most of the validation sites, TROPOMI allows for daily validation results as robust as those  
762 obtained with OMI on a monthly basis.

763 The number of ground-based stations providing MAX-DOAS HCHO observations is constantly growing, providing  
764 a large range of observation conditions, and for some of them, over several years allowing the comparisons of the  
765 performances of several satellite datasets. Note however that the lower range of HCHO levels is under-represented,  
766 as well as some of the largest emission regions such as South America or Africa. Following the validation study of  
767 Vigouroux et al. (2020) based on a FTIR network of instruments, this study illustrates again the added value of using  
768 a large network of instruments to draw more robust conclusions. FTIR and MAX-DOAS networks are complementary  
769 to each other and could be combined to cover as many conditions as possible. Similarly to what was achieved for the  
770 FTIR network, the MAX-DOAS HCHO datasets would benefit from further homogenisation efforts.

771 Finally, to illustrate the benefit of TROPOMI for the detection of small HCHO signals, we present a case study  
772 addressing the detection of shipping lanes in the Indian Ocean. Using simultaneous observations of tropospheric NO<sub>2</sub>  
773 and meteorological wind field data, we present strong evidences for an HCHO production in regions affected by  
774 shipping emissions. Owing to the fine spatial resolution and high spatial sampling of TROPOMI, such small signals  
775 can now be observed from space on a seasonal basis.

## 776 **Code and data availability**

777 The S5p HCHO data are available at <https://scihub.copernicus.eu>. The access and use of any Copernicus Sentinel data available  
778 through the Copernicus Sentinel Data Hub is governed by the Legal Notice on the use of Copernicus Sentinel Data and Service  
779 Information and is given here: [https://sentinels.copernicus.eu/documents/247904/690755/Sentinel\\_Data\\_Legal\\_Notice](https://sentinels.copernicus.eu/documents/247904/690755/Sentinel_Data_Legal_Notice).  
780 The QA4ECV OMI HCHO product is available at <https://doi.org/10.18758/71021031> (De Smedt et al., 2017). The MAX-DOAS  
781 datasets can be requested from the individual PIs of each station.

## 782 **Author contributions**

783 IDS coordinated the paper and carried out the analysis. GP and CV are PIs of the NIDFORVAL S5PVT project, SC ensures the  
784 MPC routine validation. IDS, PH, YH, CL, DL, FR, NT, JV, MVR developed the TROPOMI HCHO product. FB, IDS, YH, AR,  
785 MVR, TW developed the QA4ECV OMI HCHO product. AB, NB, KLC, SD, FH, HI, VK, CL, AP, CRC, RGR, MVR, TW are  
786 PIs for the QA4ECV MAX-DOAS measurements. BL, SC, GP, CV performed MAX-DOAS data collection and format  
787 harmonization and carried out the validation analysis. SC, KUE and JCL are responsible of the MPC routine validation. MVR is  
788 the coordinator of this research. All co-authors revised and commented on the paper.

## 789 **Acknowledgements**

790 This work contains modified Copernicus Sentinel-5 Precursor satellite data (2018-2020) post-processed by BIRA-IASB. Part of  
791 the reported work was carried out in the framework of the Copernicus Sentinel-5 Precursor Mission Performance Centre (S5p  
792 MPC), contracted by the European Space Agency (ESA/ESRIN, Contract No. 4000117151/16/I-LG) and supported by the Belgian  
793 Federal Science Policy Office (BELSPO), the Royal Belgian Institute for Space Aeronomy (BIRA-IASB) and the German  
794 Aerospace Centre (DLR). BIRA-IASB acknowledges national funding from BELSPO and ESA through the ProDEX projects  
795 TRACE-S5P (TRACE-S5P project) and TROVA. Part of this work was carried out also in the framework of the S5p Validation  
796 Team (S5PVT) AO projects NIDFORVAL (ID #28607, PI G. Pinardi, C. Vigouroux, BIRA-IASB). Multi-sensor HCHO  
797 developments have been funded by the EU FP7 QA4ECV project (grant no. 607405), in close cooperation with KNMI, University  
798 of Bremen, MPIC-Mainz and WUR. Work by H. Irie was supported by the Environment Research and Technology Development  
799 Fund (JPMEERF20192001 and JPMEERF20215005) of the Environmental Restoration and Conservation Agency of Japan, JSPS  
800 KAKENHI (grant numbers JP19H04235 and JP20H04320), and the JAXA 2nd research announcement on the Earth Observations  
801 (grant number 19RT000351). We acknowledge Mark Wenig from LMU for supporting the MAX-DOAS operations in Munich,  
802 Caroline Fayt and Christian Herman from BIRA-IASB for the Uccle and Xianghe instruments, as well as Pucai Wang from  
803 IAP/CAS for maintaining the BIRA-IASB instrument in Xianghe. We thank Alejandro Bezanilla from CCA-UNAM, Manish Naia  
804 from ARIES for the MAX-DOAS instrument operation in Pantnager and Thanawat Jarupongsakul from Chulalongkorn University  
805 for the Phimai station. We acknowledge IISER Mohali Atmospheric Chemistry Facility for supporting the MAX-DOAS operations  
806 in Mohali.

## 807 **References**

808 Alvarado, L. M. A., Richter, A., Vrekoussis, M., Hilboll, A., Kalisz Hedegaard, A. B., Schneising, O., and Burrows,  
809 J. P.: Unexpected long-range transport of glyoxal and formaldehyde observed from the Copernicus Sentinel-5

810 Precursor satellite during the 2018 Canadian wildfires, *Atmos. Chem. Phys.*, 20, 2057–2072,  
811 <https://doi.org/10.5194/acp-20-2057-2020>, 2020.

812 Arellano, J., Krüger, A., Rivera, C., Stremme, W., Friedrich, M., Bezanilla, A., and Grutter, M.: The MAX-DOAS  
813 network in Mexico City to measure atmospheric pollutants, *Atmosfera*, 29,157–167,  
814 <https://doi.org/10.20937/ATM.2016.29.02.05>, 2016.

815 Barkley, M. P., González Abad, G., Kurosu, P. T., Spurr, R., Torbatian, S. and Lerot, C.: OMI air-quality monitoring  
816 over the Middle East, *Atmos. Chem. Phys.*, 17(7), 4687–4709, doi:10.5194/acp-17-4687-2017, 2017.

817 Bauwens, M., Stavrou, T., Müller, J.-F., De Smedt, I., Van Roozendaal, M., van der Werf, G. R., Wiedinmyer, C.,  
818 Kaiser, J. W., Sindelarova, K., and Guenther, A.: Nine years of global hydrocarbon emissions based on source  
819 inversion of OMI formaldehyde observations, *Atmos. Chem. Phys.*, 16, 10133–10158, [https://doi.org/10.5194/acp-](https://doi.org/10.5194/acp-16-10133-2016)  
820 16-10133-2016, 2016.

821 Beirle, S., Platt, U., von Glasow, R., Wenig, M., and Wagner, T. : Estimate of nitrogen oxide emissions from shipping  
822 by satellite remote sensing, *Geophys. Res. Lett.*, 31, L18102, doi:10.1029/2004GL020312, 2004.

823 Beirle, S., Borger, C., Dörner, S., Li, A., Hu, Z., Liu, F., Wang, Y. and Wagner, T.: Pinpointing nitrogen oxide  
824 emissions from space, *Sci. Adv.*, 5(11), eaax9800, doi:10.1126/sciadv.aax9800, 2019.

825 Benavent, N., Garcia-Nieto, D., Wang, S. and Saiz-Lopez, A.: MAX-DOAS measurements and vertical profiles of  
826 glyoxal and formaldehyde in Madrid, Spain, *Atmos. Environ.*, 199, 357–367,  
827 doi:<https://doi.org/10.1016/j.atmosenv.2018.11.047>, 2019.

828 Boersma, K. F., Eskes, H. J., and Brinksma, E. J.: Error analysis for tropospheric NO<sub>2</sub> retrieval from space, *J.*  
829 *Geophys. Res.*, 109, <https://doi.org/10.1029/2003JD003962>, 2004.

830 Boersma, K. F., Vinken, G. C. M. and Tournadre, J.: Ships going slow in reducing their NO<sub>x</sub> emissions: changes in  
831 2005–2012 ship exhaust inferred from satellite measurements over Europe, *Environ. Res. Lett.*, 10(7), 074007,  
832 doi:10.1088/1748-9326/10/7/074007, 2015.

833 Boersma, K. F., Eskes, H. J., Richter, A., Smedt, I. De, Lorente, A., Beirle, S., Van Geffen, J. H. G. M., Zara, M.,  
834 Peters, E., Roozendaal, M. Van and others: Improving algorithms and uncertainty estimates for satellite NO<sub>2</sub>  
835 retrievals: results from the quality assurance for the essential climate variables (QA4ECV) project, *Atmos. Meas.*  
836 *Tech.*, 11(12), 6651–6678, 2018.

837 Bösch, T., Rozanov, V., Richter, A., Peters, E., Rozanov, A., Wittrock, F., Merlaud, A., Lampel, J., Schmitt, S., de  
838 Haij, M., 20Berkhout, S., Henzing, B., Apituley, A., den Hoed, M., Vonk, J., Tiefengraber, M., Müller, M.,  
839 and Burrows, J. P.: BOREAS –a new MAX-DOAS profile retrieval algorithm for aerosols and trace gases, *Atmos.*  
840 *Meas. Tech.*, 11, 6833–6859, <https://doi.org/10.5194/amt-11-6833-2018>, 2018.

841 Bovensmann, H., Peuch, V.-H., van Weele, M., Erbetseder, T., and Veihelmann, B.: Report Of The Review Of User  
842 Requirements For Sentinels-4/-5, ESA, EOP-SM/2281/BV-bv, issue: 1.2, 2011.

843 Brinkma, E. J., Pinardi, G., Volten, H., Braak, R., Richter, A., Scho, A., Van Roozendaal, M., Fayt, C., Hermans, C.,  
844 Dirksen, R. J., Vlemmix, T., Berkhout, A. J. C., Swart, D. P. J., Oetjen, H., Wittrock, F., Wagner, T., Ibrahim, O. W.,  
845 Leeuw, G. De, Moerman, M., Curier, R. L., Celarier, E. A., Cede, A., Knap, W. H., Veeffkind, J. P., Eskes, H. J.,  
846 Allaart, M., Rothe, R., PETERS, A. and Levelt, P. F.: The 2005 and 2006 DANDELIONS NO<sub>2</sub> and aerosol  
847 intercomparison campaigns, *J. Geophys. Res.*, 113(D16), 1–18, doi:10.1029/2007JD008808, 2008.

848 Cao, H., Fu, T.-M., Zhang, L., Henze, D. K., Miller, C. C., Lerot, C., Abad, G. G., Smedt, I. De, Zhang, Q.,  
849 Roozendaal, M. van and others: Adjoint inversion of Chinese non-methane volatile organic compound emissions using  
850 space-based observations of formaldehyde and glyoxal, *Atmos. Chem. Phys.*, 18(20), 15017–15046, 2018.

851 Chan, K. L., Wang, Z., Ding, A., Heue, K.-P., Shen, Y., Wang, J., Zhang, F., Shi, Y., Hao, N., and Wenig, M.: MAX-  
852 DOAS measurements of tropospheric NO<sub>2</sub> and HCHO in Nanjing and a comparison to ozone monitoring instrument  
853 observations, *Atmos. Chem. Phys.*, 19, 10051–10071, <https://doi.org/10.5194/acp-19-10051-2019>, 2019.

854 Chan, K. L., Wiegner, M., van Geffen, J., De Smedt, I., Alberti, C., Cheng, Z., Ye, S., and Wenig, M.: MAX-DOAS  
855 measurements of tropospheric NO<sub>2</sub> and HCHO in Munich and the comparison to OMI and TROPOMI satellite  
856 observations, *Atmos. Meas. Tech.*, 13, 4499–4520, <https://doi.org/10.5194/amt-13-4499-2020>, 2020.

857 Chance, K. V., Palmer, P. I., Martin, R. V., Spurr, R. J. D., Kurosu, T. P. and Jacob, D. J.: Satellite observations of  
858 formaldehyde over North America from GOME, *Geophysical Research Letters*, 27(21), 3461-3464,  
859 doi:10.1029/2000GL011857, 2000.

860 Chan Miller, C., Jacob, D. J., Marais, E. A., Yu, K., Travis, K. R., Kim, P. S., Fisher, J. A., Zhu, L., Wolfe, G. M.,  
861 Hanisco, T. F., Keutsch, F. N., Kaiser, J., Min, K.-E., Brown, S. S., Washenfelder, R. A., González Abad, G., and  
862 Chance, K.: Glyoxal yield from isoprene oxidation and relation to formaldehyde: chemical mechanism, constraints  
863 from SENEX aircraft observations, and interpretation of OMI satellite data, *Atmos. Chem. Phys.*, 17, 8725–8738,  
864 <https://doi.org/10.5194/acp-17-8725-2017>, 2017.

865 Choi, Y. and Souri, A. H.: Seasonal behavior and long-term trends of tropospheric ozone, its precursors and chemical  
866 conditions over Iran: A view from space, *Atmos. Environ.*, 106, 232–240,  
867 doi:<https://doi.org/10.1016/j.atmosenv.2015.02.012>, 2015.

868 Clémer, K., Van Roozendaal, M., Fayt, C., Hendrick, F., Hermans, C., Pinardi, G., Spurr, R., Wang, P. and De  
869 Mazière, M.: Multiple wavelength retrieval of tropospheric aerosol optical properties from MAX-DOAS  
870 measurements in Beijing, *Atmos. Meas. Tech.*, 3, 863–878 [online] Available from: doi:10.5194/amt-3-863-2010,  
871 2010.

872 Compernelle, S., Argyrouli, A., Lutz, R., Sneep, M., Lambert, J.-C., Fjæraa, A. M., Hubert, D., Keppens, A., Loyola,  
873 D., O'Connor, E., Romahn, F., Stammes, P., Verhoelst, T. and Wang, P.: Validation of the Sentinel-5 Precursor  
874 TROPOMI cloud data with Cloudnet, Aura OMI O<sub>2</sub>-O<sub>2</sub>, MODIS and Suomi-NPP VIIRS, *Atmos. Meas. Tech.*  
875 *Discuss.*, (June), 1–33, doi:10.5194/amt-2020-122, 2020.

876 De Smedt, I., Müller, J.-F., Stavrakou, T., van der A, R., Eskes, H. and Van Roozendael, M.: Twelve years of global  
877 observations of formaldehyde in the troposphere using GOME and SCIAMACHY sensors, *Atmos. Chem. Phys.*,  
878 8(16), 4947-4963, 2008.

879 De Smedt, I., Stavrakou, T., Müller, J. F., van Der A, R. J. and Van Roozendael, M.: Trend detection in satellite  
880 observations of formaldehyde tropospheric columns, *Geophys. Res. Lett.*, 37(18), L18808,  
881 doi:10.1029/2010GL044245, 2010.

882 De Smedt, I., Van Roozendael, M., Stavrakou, T., Müller, J.-F., Lerot, C., Theys, N., Valks, P., Hao, N., and van der  
883 A, R.: Improved retrieval of global tropospheric formaldehyde columns from GOME-2/MetOp-A addressing noise  
884 reduction and instrumental degradation issues, *Atmos. Meas. Tech.*, 5, 2933–2949, [https://doi.org/10.5194/amt-5-](https://doi.org/10.5194/amt-5-2933-2012)  
885 2933-2012, 2012. De Smedt, I., Stavrakou, T., Hendrick, F., Danckaert, T., Vlemmix, T., Pinardi, G., Theys, N., Lerot,  
886 C., Gielen, C., Vigouroux, C., Hermans, C., Fayt, C., Veefkind, P., Müller, J.-F., and Van Roozendael, M.: Diurnal,  
887 seasonal and long-term variations of global formaldehyde columns inferred from combined OMI and GOME-2  
888 observations, *Atmos. Chem. Phys.*, 15, 12519-12545, doi:10.5194/acp-15-12519-2015, 2015

889 De Smedt, I., Yu, H., Richter, A., Beirle, S., Eskes, H., Boersma, K.F., Van Roozendael, M., Van Geffen, J., Lorente,  
890 A. and Peters, E.: QA4ECV HCHO tropospheric column data from OMI (Version 1.1) [Data set], 2017.

891 De Smedt, I., Theys, N., Yu, H., Danckaert, T., Lerot, C., Compernelle, S., Van Roozendael, M., Richter, A., Hilboll,  
892 A., Peters, E., Pedergnana, M., Loyola, D., Beirle, S., Wagner, T., Eskes, H., van Geffen, J., Boersma, K. F., and  
893 Veefkind, P.: Algorithm theoretical baseline for formaldehyde retrievals from S5P TROPOMI and from the QA4ECV  
894 project, *Atmos. Meas. Tech.*, 11, 2395–2426, <https://doi.org/10.5194/amt-11-2395-2018>, 2018.

895 Dimitropoulou, E., Hendrick, F., Pinardi, G., Friedrich, M. M., Merlaud, A., Tack, F., De Longueville, H., Fayt, C.,  
896 Hermans, C., Laffineur, Q., Fierens, F., and Van Roozendael, M.: Validation of TROPOMI tropospheric NO<sub>2</sub> columns  
897 using dual-scan multi-axis differential optical absorption spectroscopy (MAX-DOAS) measurements in Uccle,  
898 Brussels, *Atmos. Meas. Tech.*, 13, 5165–5191, <https://doi.org/10.5194/amt-13-5165-2020>, 2020.

899 Drosoglou, T., Bais, A. F., Zyrichidou, I., Kouremeti, N., Poupkou, A., Liora, N., Giannaros, C., Koukouli, M. E.,  
900 Balis, D., and Melas, D.: Comparisons of ground-based tropospheric NO<sub>2</sub> MAX-DOAS measurements to satellite  
901 observations with the aid of an air quality model over the Thessaloniki area, Greece, *Atmos. Chem. Phys.*, 17, 5829-  
902 5849, <https://doi.org/10.5194/acp-17-5829-2017>, 2017.

903 ESA: Sentinel-5 Precursor Calibration and Validation Plan for the Operational Phase, ref: ESA-EOPG-CSCOP-PL-  
904 0073, issue:1.1, 06/11/2017 ([https://sentinel.esa.int/documents/247904/2474724/Sentinel-5P-Calibration-and-](https://sentinel.esa.int/documents/247904/2474724/Sentinel-5P-Calibration-and-Validation-Plan.pdf)  
905 [Validation-Plan.pdf](https://sentinel.esa.int/documents/247904/2474724/Sentinel-5P-Calibration-and-Validation-Plan.pdf)).

906 Fortems-Cheiney, A., Chevallier, F., Pison, I., Bousquet, P., Sauniois, M., Szopa, S., Cressot, C., Kurosu, T. P., Chance,  
907 K., and Fried, A.: The formaldehyde budget as seen by a global-scale multi-constraint and multi-species inversion  
908 system, *Atmos. Chem. Phys.*, 12, 6699–6721, <https://doi.org/10.5194/acp-12-6699-2012>, 2012.

909 Franco, B., Hendrick, F., Van Roozendael, M., Müller, J.-F., Stavrou, T., Marais, E. A., Bovy, B., Bader, W., Fayt,  
910 C., Hermans, C., Lejeune, B., Pinardi, G., Servais, C., and Mahieu, E.: Retrievals of formaldehyde from ground-based  
911 FTIR and MAX-DOAS observations at the Jungfraujoch station and comparisons with GEOS-Chem and IMAGES  
912 model simulations, *Atmos. Meas. Tech.*, 8, 1733-1756, doi:10.5194/amt-8-1733-2015, 2015.

913 Franco, B., Blumenstock, T., Cho, C., Clarisse, L., Clerbaux, C., Coheur, P.-F., De Mazière, M., De Smedt, I., Dorn,  
914 H.-P., Emmerichs, T., Fuchs, H., Gkatzelis, G., Griffith, D., et al.: Ubiquitous atmospheric production of organic acids  
915 mediated by warm clouds, *Nature*, 2017-10-14339, 2021.

916 Friedrich, M. M., Rivera, C., Stremme, W., Ojeda, Z., Arellano, J., Bezanilla, A., García-Reynoso, J. A., and Grutter,  
917 M.: NO<sub>2</sub> vertical profiles and column densities from MAX-DOAS measurements in Mexico City, *Atmos. Meas.*  
918 *Tech.*, 12, 2545–2565, <https://doi.org/10.5194/amt-12-2545-2019>, 2019.

919 Frieß, U., Monks, P. S., Remedios, J. J., Rozanov, A., Sinreich, R., Wagner, T. and Platt, U.: MAX-DOAS O<sub>4</sub>  
920 measurements: A new technique to derive information on atmospheric aerosols: 2. Modeling studies, *J. Geophys. Res.*,  
921 111(D14), doi:10.1029/2005JD006618, 2006.

922 Frieß, U., Klein Baltink, H., Beirle, S., Clèmer, K., Hendrick, F., Henzing, B., Irie, H., Leeuw, G. de, Li, A., Moerman,  
923 M. M., Roozendael, M. van, Shaiganfar, R., Wagner, T., Wang, Y., Xie, P., Yilmaz, S. and Zieger, P.: Intercomparison  
924 of aerosol extinction profiles retrieved from MAX-DOAS measurements, *Atmos. Meas. Tech.*, 9, 3205–3222,  
925 <https://doi.org/10.5194/amt-9-3205-2016>, 2016.

926 Frieß, U., Beirle, S., Alvarado Bonilla, L., Bösch, T., Friedrich, M. M., Hendrick, F., Piders, A., Richter, A., van  
927 Roozendael, M., Rozanov, V. V., Spinei, E., Tirpitz, J.-L., Vlemmix, T., Wagner, T., and Wang, Y.: Intercomparison  
928 of MAX-DOAS vertical profile retrieval algorithms: studies using synthetic data, *Atmos. Meas. Tech.*, 12, 2155-2181,  
929 <https://doi.org/10.5194/amt-12-2155-2019>, 2019.

930 Georgoulias, A. K., Boersma, K. F., van Vliet, J., Zhang, X., van der A, R., Zanis, P. and de Laat, J.: Detection of NO  
931 2 pollution plumes from individual ships with the TROPOMI/S5P satellite sensor, *Environ. Res. Lett.*, 15(12), 124037,  
932 doi:10.1088/1748-9326/abc445, 2020.

933 Gielen, C., Hendrick, F., Pinardi, G., De Smedt, I., Fayt, C., Hermans, C., Stavrou, T., Bauwens, M., Müller, J.,  
934 Ndenzako, E., Nzohabonayo, P., Akimana, R., Niyonzima, S., Van Roozendael, M. and De Mazière, M.:  
935 Characterisation of Central-African aerosol and trace-gas emissions based on MAX-DOAS measurements and model  
936 simulations over, *Atmos. Chem. Phys. Discuss.*, (2), 1–41, doi:10.5194/acp-2016-1104, 2017.

937 González Abad, G., Liu, X., Chance, K., Wang, H., Kurosu, T. P. and Suleiman, R.: Updated Smithsonian  
938 Astrophysical Observatory Ozone Monitoring Instrument (SAO OMI) formaldehyde retrieval, *Atmos. Meas. Tech.*,  
939 8(1), 19–32, doi:10.5194/amt-8-19-2015, 2015.

940 González Abad, G., Vasilkov, A., Seftor, C., Liu, X., and Chance, K.: Smithsonian Astrophysical Observatory Ozone  
941 Mapping and Profiler Suite (SAO OMPS) formaldehyde retrieval, *Atmos. Meas. Tech.*, 9, 2797–2812,  
942 <https://doi.org/10.5194/amt-9-2797-2016>, 2016.

943 Gonzalez Abad, G., Souri, A. H., Bak, J., Chance, K., Flynn, L. E., Krotkov, N. A., Lamsal, L., Li, C., Liu, X., Miller,  
944 C. C., Nowlan, C. R., Suleiman, R. and Wang, H.: Five decades observing Earth's atmospheric trace gases using  
945 ultraviolet and visible backscatter solar radiation from space, *J. Quant. Spectrosc. Radiat. Transf.*, 238, 106478,  
946 doi:<https://doi.org/10.1016/j.jqsrt.2019.04.030>, 2019.

947 Hassinen, S., Balis, D., Bauer, H., Begoin, M., Delcloo, A., Eleftheratos, K., Gimeno Garcia, S., Granville, J., Grossi,  
948 M., Hao, N., Hedelt, P., Hendrick, F., Hess, M., Heue, K.-P., Hovila, J., Jönch-Sørensen, H., Kalakoski, N., Kauppi,  
949 A., Kiemle, S., Kins, L., Koukouli, M. E., Kujanpää, J., Lambert, J.-C., Lang, R., Lerot, C., Loyola, D., Pedernana,  
950 M., Pinardi, G., Romahn, F., Van Roozendael, M., Lutz, R., De Smedt, I., Stammes, P., Steinbrecht, W., Tamminen,  
951 J., Theys, N., Tilstra, L. G., Tuinder, O. N. E., Valks, P., Zerefos, C., Zimmer, W. and Zyrrichidou, I.: Overview of the  
952 O3M SAF GOME-2 operational atmospheric composition and UV radiation data products and data availability,  
953 *Atmos. Meas. Tech.*, 9(2), 383–407, doi:10.5194/amt-9-383-2016, 2016.

954 Heckel, A., Richter, A., Tarsu, T., Wittrock, F., Hak, C., Pundt, I., Junkermann, W., and Burrows, J. P.: MAX-DOAS  
955 measurements of formaldehyde in the Po-Valley, *Atmos. Chem. Phys.*, 5, 909–918, [http://www.atmos-chem-](http://www.atmos-chem-phys.net/5/909/2005)  
956 [phys.net/5/909/2005](http://www.atmos-chem-phys.net/5/909/2005), 2005.

957 Hewson, W., Bösch, H., Barkley, M. P. and De Smedt, I.: Characterisation of GOME-2 formaldehyde retrieval  
958 sensitivity, *Atmospheric Measurement Techniques*, 6(2), 371–386, doi:10.5194/amt-6-371-2013, 2013.

959 Hendrick, F., Müller, J.-F., Clémer, K., Wang, P., De Mazière, M., Fayt, C., Gielen, C., Hermans, C., Ma, J. Z.,  
960 Pinardi, G., Stavrou, T., Vlemmix, T. and Van Roozendael, M.: Four years of ground-based MAX-DOAS  
961 observations of HONO and NO<sub>2</sub> in the Beijing area, *Atmos. Chem. Phys.*, 14(2), 765–781, doi:10.5194/acp-14-765-  
962 2014, 2014.

963 Honninger, G., von Friedeburg, C. and Platt, U.: Multi axis differential optical absorption spectroscopy (MAX-  
964 DOAS), *Atmos. Chem. Phys.*, 4, 231–254, [www.atmos-chem-phys.org/acp/4/231/](http://www.atmos-chem-phys.org/acp/4/231/), 2004.

965 Hoque, H. M. S., Irie, H., & Damiani, A. : First MAX-DOAS observations of formaldehyde and glyoxal in Phimai,  
966 Thailand, *Journal of Geophysical Research: Atmospheres*, 123, 9957–9975, <https://doi.org/10.1029/2018JD028480>,  
967 2018.

968 Irie, H., Kanaya, Y., Akimoto, H., Iwabuchi, H., Shimizu, a. and Aoki, K.: Dual-wavelength aerosol vertical profile  
969 measurements by MAX-DOAS at Tsukuba , Japan, *Atmos. Chem. Phys.*, 9(2), 2741–2749, doi:10.5194/acp-8-341-  
970 2008, 2009.

971 Irie, H., Takashima, H., Kanaya, Y., Boersma, K. F., Gast, L., Wittrock, F., Brunner, D., Zhou, Y. and Van  
972 Roozendael, M.: Eight-component retrievals from ground-based MAX-DOAS observations, *Atmos. Meas. Tech.*,  
973 4(1), 1027–1044, doi:10.5194/amtd-4-639-2011, 2011.

974 Irie, H., Boersma, K. F., Kanaya, Y., Takashima, H., Pan, X., and Wang, Z. F.: Quantitative bias estimates for  
975 tropospheric NO<sub>2</sub> columns retrieved from SCIAMACHY, OMI, and GOME-2 using a common standard for East  
976 Asia, *Atmos. Meas. Tech.*, 5, 2403-2411, doi:10.5194/amt-5-2403-2012, 2012.

977 Irie, H., T. Nakayama, A. Shimizu, A. Yamazaki, T. Nagai, A. Uchiyama, Y. Zaizen, S. Kagamitani, and Y. Matsumi,  
978 Evaluation of MAX-DOAS aerosol retrievals by coincident observations using CRDS, lidar, and sky radiometer in  
979 Tsukuba, Japan, *Atmospheric Measurement Techniques*, 8, 2775–2788, doi:10.5194/amt-8-2775-2015, 2015.

980 Irie, H., Hoque, H. M. S., Damiani, A., Okamoto, H., Fatmi, A. M., Khatri, P., Takamura, T., and Jarupongsakul, T.:  
981 Simultaneous observations by sky radiometer and MAX-DOAS for characterization of biomass burning plumes in  
982 central Thailand in January–April 2016, *Atmos. Meas. Tech.*, 12, 599–606, <https://doi.org/10.5194/amt-12-599-2019>,  
983 2019.

984 Jin, X., Fiore, A. M. A. M. A. M., Murray, L. T. L. T., Valin, L. C. L. C., Lamsal, L. N. L. N. L. N., Duncan, B.,  
985 Folkert Boersma, K., De Smedt, I., Abad, G. G. G. G., Chance, K., others and Tonnesen, G. S. G. S.: Evaluating a  
986 space-based indicator of surface ozone-NO<sub>x</sub>-VOC sensitivity over mid-latitude source regions and application to  
987 decadal trends, *J. Geophys. Res. Atmos.*, 122(19), 439–461, doi:10.1002/2017JD026720, 2017.

988 Jin, X., Fiore, A., Boersma, K. F., De Smedt, I. & Valin, L. Inferring changes in summertime surface ozone–NO<sub>x</sub>–  
989 VOC chemistry over U.S. urban areas from two decades of satellite and ground-based observations. *Environ. Sci.*  
990 *Technol.* 54, 6518–6529, 2020.

991 Jung, Y, González Abad, G., Nowlan, C. R., Chance, K., Liu, X., Torres, O., & Ahn, C.: Explicit aerosol correction  
992 of OMI formaldehyde retrievals. *Earth and Space Science*, 6, 2087–2105, <https://doi.org/10.1029/2019EA000702>,  
993 2019.

994 Kaiser, J., Jacob, D. J., Zhu, L., Travis, K. R., Fisher, J. A., González Abad, G., Zhang, L., Zhang, X., Fried, A.,  
995 Crounse, J. D., St. Clair, J. M., and Wisthaler, A.: High-resolution inversion of OMI formaldehyde columns to quantify  
996 isoprene emission on ecosystem-relevant scales: application to the southeast US, *Atmos. Chem. Phys.*, 18, 5483–5497,  
997 <https://doi.org/10.5194/acp-18-5483-2018>, 2018.

998 Khan, W. A., Khokhar, M. F., Shoaib, A. and Nawaz, R.: Monitoring and analysis of formaldehyde columns over  
999 Rawalpindi-Islamabad, Pakistan using MAX-DOAS and satellite observation, *Atmos. Pollut. Res.*, (November 2017),  
1000 0–1, doi:10.1016/j.apr.2017.12.008, 2018.

1001 Kleipool, Q. L., Dobber, M. R., de Haan, J. F., and Levelt, P. F.: Earth surface reflectance climatology from 3 years  
1002 of OMI data, *J. Geophys. Res.*, 113, D18308, <https://doi.org/10.1029/2008JD010290>, 2008.

1003 Kleipool, Q., Ludewig, A., Babić, L., Bartstra, R., Braak, R., Dierssen, W., Dewitte, P.-J., Kenter, P., Landzaat, R.,  
1004 Leloux, J., Loots, E., Meijering, P., van der Plas, E., Rozemeijer, N., Schepers, D., Schiavini, D., Smeets, J., Vacanti,  
1005 G., Vonk, F., and Veeffkind, P.: Pre-launch calibration results of the TROPOMI payload on-board the Sentinel-5  
1006 Precursor satellite, *Atmos. Meas. Tech.*, 11, 6439–6479, <https://doi.org/10.5194/amt-11-6439-2018>, 2018.

1007 Kreher, K., Van Roozendaal, M., Hendrick, F., Apituley, A., Dimitropoulou, E., Frieß, U., Richter, A., Wagner, T.,  
1008 Lampel, J., Abuhassan, N., Ang, L., Anguas, M., Bais, A., Benavent, N., Bösch, T., Bogner, K., Borovski, A.,  
1009 Bruchkouski, I., Cede, A., Chan, K. L., Donner, S., Drosoglou, T., Fayt, C., Finkenzeller, H., Garcia-Nieto, D., Gielen,  
1010 C., Gómez-Martín, L., Hao, N., Henzing, B., Herman, J. R., Hermans, C., Hoque, S., Irie, H., Jin, J., Johnston, P.,

1011 Khayyam Butt, J., Khokhar, F., Koenig, T. K., Kuhn, J., Kumar, V., Liu, C., Ma, J., Merlaud, A., Mishra, A. K.,  
1012 Müller, M., Navarro-Comas, M., Ostendorf, M., Pazmino, A., Peters, E., Pinardi, G., Pinharanda, M., Piders, A., Platt,  
1013 U., Postlyakov, O., Prados-Roman, C., Puentedura, O., Querel, R., Saiz-Lopez, A., Schönhardt, A., Schreier, S. F.,  
1014 Seyler, A., Sinha, V., Spinei, E., Strong, K., Tack, F., Tian, X., Tiefengraber, M., Tirpitz, J.-L., van Gent, J., Volkamer,  
1015 R., Vrekoussis, M., Wang, S., Wang, Z., Wenig, M., Wittrock, F., Xie, P. H., Xu, J., Yela, M., Zhang, C., and Zhao,  
1016 X.: Intercomparison of NO<sub>2</sub>, O<sub>4</sub>, O<sub>3</sub> and HCHO slant column measurements by MAX-DOAS and zenith-sky UV-  
1017 visible spectrometers during CINDI-2, *Atmos. Meas. Tech.*, 13, 2169–2208, [https://doi.org/10.5194/amt-13-2169-](https://doi.org/10.5194/amt-13-2169-2020)  
1018 2020, 2020.

1019 Kumar, V., Beirle, S., Dörner, S., Mishra, A. K., Donner, S., Wang, Y., Sinha, V., and Wagner, T.: Long-term MAX-  
1020 DOAS measurements of NO<sub>2</sub>, HCHO, and aerosols and evaluation of corresponding satellite data products over  
1021 Mohali in the Indo-Gangetic Plain, *Atmos. Chem. Phys.*, 20, 14183–14235, [https://doi.org/10.5194/acp-20-14183-](https://doi.org/10.5194/acp-20-14183-2020)  
1022 2020, 2020.

1023 Kwon, H.-A., Park, R. J., González Abad, G., Chance, K., Kurosu, T. P., Kim, J., Smedt, I. De, Roozendael, M. Van,  
1024 Peters, E. and Burrows, J.: Description of a formaldehyde retrieval algorithm for the Geostationary Environment  
1025 Monitoring Spectrometer (GEMS), *Atmos. Meas. Tech.*, 12(7), 3551–3571, 2019.

1026 Langen, J., Meijer, Y., Brinksma, E., Veihelmann, B., and Ingmann, P.: Copernicus Sentinels 4 and 5 Mission  
1027 Requirements Traceability Document (MRTD), ESA, EOP-SM/2413/BV-bv , issue: 2, 2017.

1028 Levelt, P. F., van den Oord, G. H. ., Dobber, M. R., Malkki, A., Visser, H., de Vries, J., Stammes, P., Lundell, J. O. .  
1029 and Saari, H.: The ozone monitoring instrument, *IEEE Trans. on Geosc. and Rem. Sens.*, 44(5), 1093–1101, 2006.

1030 Levelt, P. F., Joiner, J., Tamminen, J., Veefkind, J. P., Bhartia, P. K., Fioletov, V., Carn, S., Laat, J. De, Deland, M.,  
1031 Marchenko, S. and Mcpeters, R.: The Ozone Monitoring Instrument : overview of 14 years in space, *Atmos. Chem.*  
1032 *Phys.*, (18), 5699–5745, 2018.

1033 Levelt, P.F., Stein Zweers, Aben, Bauwens, Borsdorff, De Smedt, J. Eskes, Lerot, Loyola, Romahn, Stavrakou, Theys,  
1034 Van Roozendael, Veefkind, Verhoels: Air Quality Impacts of COVID-19 Lockdown Measures detected from space  
1035 using high spatial resolution observations of multiple trace gases from Sentinel-5P/TROPOMI, to be submitted to  
1036 ACP, 2021.

1037 Li, X., Brauers, T., Shao, M., Garland, R. M., Wagner, T., Deutschmann, T. and Wahner, A.: MAX-DOAS  
1038 measurements in southern China: retrieval of aerosol extinctions and validation using ground-based in-situ data,  
1039 *Atmos. Chem. Phys.*, 10(5), 2079–2089, doi:10.5194/acp-10-2079-2010, 2010.

1040 Li, C., Joiner, J., Krotkov, N. A., and Dunlap, L.: A new method for global retrievals of HCHO total columns from  
1041 the Suomi National Polar-orbiting Partnership Ozone Mapping and Profiler Suite. *Geophys. Res. Lett.*, 42, 2515–  
1042 2522. doi: 10.1002/2015GL063204, 2015.

1043 Li, K., Jacob, D. J., Shen, L., Lu, X., De Smedt, I., and Liao, H.: Increases in surface ozone pollution in China from  
1044 2013 to 2019: anthropogenic and meteorological influences, *Atmos. Chem. Phys.*, 20, 11423–11433,  
1045 <https://doi.org/10.5194/acp-20-11423-2020>, 2020.

1046 Lorente, A., Folkert Boersma, K., Yu, H., Dörner, S., Hilboll, A., Richter, A., Liu, M., Lamsal, L. N., Barkley, M.,  
1047 De Smedt, I., Van Roozendael, M., Wang, Y., Wagner, T., Beirle, S., Lin, J.-T., Krotkov, N., Stammes, P., Wang, P.,  
1048 Eskes, H. J., and Krol, M.: Structural uncertainty in air mass factor calculation for NO<sub>2</sub> and HCHO satellite retrievals,  
1049 *Atmos. Meas. Tech.*, 10, 759–782, <https://doi.org/10.5194/amt-10-759-2017>, 2017.

1050 Loyola, D. G., Xu, J., Heue, K.-P., and Zimmer, W.: Applying FP\_ILM to the retrieval of geometry-dependent  
1051 effective Lambertian equivalent reflectivity (GE\_LER) daily maps from UVN satellite measurements, *Atmos. Meas.*  
1052 *Tech.*, 13, 985–999, <https://doi.org/10.5194/amt-13-985-2020>, 2020.

1053 Eskes, H. J., and Krol, M.: Structural uncertainty in air mass factor calculation for NO<sub>2</sub> and HCHO satellite retrievals,  
1054 *Atmos. Meas. Tech.*, 10, 759–782, <https://doi.org/10.5194/amt-10-759-2017>, 2017.

1055 Loyola, D. G., Gimeno García, S., Lutz, R., Argyrouli, A., Romahn, F., Spurr, R. J. D., Pedernana, M., Doicu, A.,  
1056 Molina García, V., and Schüssler, O.: The operational cloud retrieval algorithms from TROPOMI on board Sentinel-  
1057 5 Precursor, *Atmos. Meas. Tech.*, 11, 409–427, <https://doi.org/10.5194/amt-11-409-2018>, 2018.

1058 Ludewig, A., Kleipool, Q., Bartstra, R., Landzaat, R., Leloux, J., Loots, E., Meijering, P., van der Plas, E., Rozemeijer,  
1059 N., Vonk, F., and Veeffkind, P.: In-flight calibration results of the TROPOMI payload on board the Sentinel-5  
1060 Precursor satellite, *Atmos. Meas. Tech.*, 13, 3561–3580, <https://doi.org/10.5194/amt-13-3561-2020>, 2020.

1061 Ma, J. Z., Beirle, S., Jin, J. L., Shaiganfar, R., Yan, P., and Wagner, T.: Tropospheric NO<sub>2</sub> vertical column densities  
1062 over Beijing: results of the first three years of ground-based MAX-DOAS measurements (2008–2011) and satellite  
1063 validation, *Atmos. Chem. Phys.*, 13, 1547–1567, doi:10.5194/acp-13-1547-2013, 2013.

1064 Mahajan, A. S., De Smedt, I., Biswas, M. S., Ghude, S., Fadnavis, S., Roy, C. and van Roozendael, M.: Inter-annual  
1065 variations in satellite observations of nitrogen dioxide and formaldehyde over India, *Atmos. Environ.*, 116, 194–201,  
1066 doi:10.1016/j.atmosenv.2015.06.004, 2015.

1067 Marais, E. A., Jacob, D. J., Kurosu, T. P., Chance, K., Murphy, J. G., Reeves, C., Mills, G., Casadio, S., Millet, D. B.,  
1068 Barkley, M. P., Paulot, F., and Mao, J.: Isoprene emissions in Africa inferred from OMI observations of formaldehyde  
1069 columns, *Atmos. Chem. Phys.*, 12, 6219–6235, <https://doi.org/10.5194/acp-12-6219-2012>, 2012.

1070 Marbach, T., Beirle, S., Platt, U., Hoor, P., Wittrock, F., Richter, A., Vrekoussis, M., Grzegorski, M., Burrows, J. P.  
1071 and Wagner, T.: Satellite measurements of formaldehyde linked to shipping emissions, *Atmos. Chem. Phys.*, 9(21),  
1072 8223–8234, doi:10.5194/acp-9-8223-2009, 2009.

1073 Meller, R. and Moortgat, G. K.: Temperature dependence of the absorption cross section of HCHO between 223 and  
1074 323 K in the wavelength range 225–375 nm, *J. Geophys. Res.*, 105, 7089–7102,  
1075 <https://doi.org/10.1029/1999JD901074>, 2000.

1076 Millet, D. B., Jacob, D. J., Boersma, K. F., Fu, T.-M., Kurosu, T. P., Chance, K. V., Heald, C. L. and Guenther, A.:  
1077 Spatial distribution of isoprene emissions from North America derived from formaldehyde column measurements by  
1078 the OMI satellite sensor, *Journal of Geophysical Research*, 113(D2), 1-18, doi:10.1029/2007JD008950, 2008.

1079 Nightingale, J., Boersma, K., Muller, J.-P., Compernelle, S., Lambert, J.-C., Blessing, S., Giering, R., Gobron, N., De  
1080 Smedt, I., Coheur, P. and others: Quality assurance framework development based on six new ECV data products to  
1081 enhance user confidence for climate applications, *Remote Sens.*, 10(8), 1254, 2018.

1082 Opacka, B., Müller, J.-F., Stavrakou, T., Bauwens, M., Sindelarova, K., Markova, J., and Guenther, A. B.: Global and  
1083 regional impacts of land cover changes on isoprene emissions derived from spaceborne data and the MEGAN model,  
1084 *Atmos. Chem. Phys.*, 21, 8413–8436, <https://doi.org/10.5194/acp-21-8413-2021>, 2021 .

1085 Palmer, P. I., Jacob, D. J., Chance, K. V., Martin, R. V., D, R. J., Kurosu, T. P., Bey, I., Yantosca, R. and Fiore, A.:  
1086 Air mass factor formulation for spectroscopic measurements from satellites: Application to formaldehyde retrievals  
1087 from the Global Ozone Monitoring Experiment, *Journal of Geophysical Research*, 106(D13), 14539-14550,  
1088 doi:10.1029/2000JD900772, 2001.

1089 Pinardi, G., Van Roozendaal, M., Abuhassan, N., Adams, C., Cede, A., Clémer, K., Fayt, C., Frieß, U., Gil, M.,  
1090 Herman, J., Hermans, C., Hendrick, F., Irie, H., Merlaud, A., Navarro Comas, M., Peters, E., Piters, A. J. M.,  
1091 Puentedura, O., Richter, A., Schönhardt, A., Shaiganfar, R., Spinei, E., Strong, K., Takashima, H., Vrekoussis, M.,  
1092 Wagner, T., Wittrock, F., and Yilmaz, S.: MAX-DOAS formaldehyde slant column measurements during CINDI:  
1093 inter-comparison and analysis improvement, *Atmos. Meas. Tech.*, 6, 167-185, doi:10.5194/amt-6-167-2013, 2013.

1094 Platt, U and Stutz, J.: *Differential Optical Absorption Spectroscopy: Principles and Applications (Physics of Earth and*  
1095 *Space Environments)*, Springer-Verlag, Berlin, Heidelberg, ISBN 978-3540211938, 2008.

1096 Richter, A., Eyring, V., Burrows, J. P., Bovensmann, H., Lauer, A., Sierk, B., and Crutzen, P. J., Satellite  
1097 measurements of NO<sub>2</sub> from international shipping emissions, *Geophys. Res. Lett.*, 31, L23110,  
1098 doi:10.1029/2004GL020822, 2004.

1099 Richter, A., Begoin, M., Hilboll, A. and Burrows, J.P.: An improved NO<sub>2</sub> retrieval for the GOME-2 satellite  
1100 instrument, *Atmos. Meas. Tech.*, 4(1), 1147–1159, doi:10.5194/amtd-4-213-2011, 2011.

1101 Richter, A., Hilboll, A., Sanders, A., Peters, E. and Burrows, J.P.: Inhomogeneous scene effects in OMI NO<sub>2</sub>  
1102 observations, *Geophysical Research Abstracts*, EGU General Assembly 2018, Vol. 20, EGU2018-9630-3,  
1103 <https://meetingorganizer.copernicus.org/EGU2018/EGU2018-9630-3.pdf>, 2018. Richter, A., Hilboll, A., Sanders, A.  
1104 and Burrows, J.P.: Inhomogeneous scene effects in TROPOMI satellite data, 9th DOAS Workshop, 13-15 July 2020,  
1105 Utrecht, 2020.

1106 Rivera Cárdenas, C., Guarín, C., Stremme, W., Friedrich, M. M., Bezanilla, A., Rivera Ramos, D., Mendoza-  
1107 Rodríguez, C. A., Grutter, M., Blumenstock, T., and Hase, F.: Formaldehyde total column densities over Mexico City:  
1108 comparison between multi-axis differential optical absorption spectroscopy and solar-absorption Fourier transform  
1109 infrared measurements, *Atmos. Meas. Tech.*, 14, 595–613, <https://doi.org/10.5194/amt-14-595-2021>, 2021.

1110 Rodgers, C. D.: Inverse Methods for Atmospheric Sounding, Theory and Practice, World Scientific Publishing,  
1111 Singapore-New-Jersey-London-Hong Kong, 2000.

1112 Rodgers, C. D., and B. J. Connor: Intercomparison of remote sounding instruments, *J. Geophys. Res.*, 108,  
1113 doi:10.1029/2002JD002299, 2003.

1114 Ryan, R. G., Silver, J. D., Querel, R., Smale, D., Rhodes, S., Tully, M., Jones, N., and Schofield, R.: Comparison of  
1115 formaldehyde tropospheric columns in Australia and New Zealand using MAX-DOAS, FTIR and TROPOMI, *Atmos.*  
1116 *Meas. Tech.*, 13, 6501–6519, <https://doi.org/10.5194/amt-13-6501-2020>, 2020.

1117 Sen, P. K.: Estimates of the regression coefficient based on Kendall's tau, *J. Am. Stat. Assoc.*, 63, 1379–1389,  
1118 <https://doi.org/10.2307/2285891>, 1968.

1119 Shen, L., Jacob, D. J., Zhu, L., Zhang, Q., Zheng, B., Sulprizio, M. P., Li, K., De Smedt, I., González Abad, G., Cao,  
1120 H. and others: The 2005–2016 trends of formaldehyde columns over China observed by satellites: Increasing  
1121 anthropogenic emissions of volatile organic compounds and decreasing agricultural fire emissions, *Geophys. Res.*  
1122 *Lett.*, 46(8), 4468–4475, 2019.

1123 Sinreich, R., Frieß, U., Wagner, T., and Platt, U.: Multi axis differential optical absorption spectroscopy (MAX-  
1124 DOAS) of gas and aerosol distributions, *Faraday Discuss.*, 130, 153–164, <https://doi.org/10.1039/B419274P>, 2005.

1125 Song, C. H., Kim, H. S., von Glasow, R., Brimblecombe, P., Kim, J., Park, R. J., Woo, J. H., and Kim, Y. H.: Source  
1126 identification and budget analysis on elevated levels of formaldehyde within the ship plumes: a ship-plume  
1127 photochemical/dynamic model analysis, *Atmos. Chem. Phys.*, 10, 11969–11985, [https://doi.org/10.5194/acp-10-](https://doi.org/10.5194/acp-10-11969-2010)  
1128 [11969-2010](https://doi.org/10.5194/acp-10-11969-2010), 2010

1129 Souri, A. H., Nowlan, C. R., Wolfe, G. M., Lamsal, L. N., Chan Miller, C. E., Abad, G. G., Janz, S. J., Fried, A.,  
1130 Blake, D. R., Weinheimer, A. J., Diskin, G. S., Liu, X. and Chance, K.: Revisiting the effectiveness of HCHO/NO<sub>2</sub>  
1131 ratios for inferring ozone sensitivity to its precursors using high resolution airborne remote sensing observations in a  
1132 high ozone episode during the KORUS-AQ campaign, *Atmos. Environ.*, 224, 117341,  
1133 doi:<https://doi.org/10.1016/j.atmosenv.2020.117341>, 2020.

1134 Spurr, R. J. D.: LIDORT and VLIDORT: Linearized pseudo-spherical scalar and vector discrete ordinate radiative  
1135 transfer models for use in remote sensing retrieval problems, in *Light Scattering Reviews*, edited by: Kokhanovsky,  
1136 A., 229–271, Berlin, 2008.

1137 Stavroukou, T., Müller, J.-F., Bauwens, M., De Smedt, I., Van Roozendael, M., Guenther, A., Wild, M. and Xia, X.:  
1138 Isoprene emissions over Asia 1979–2012: impact of climate and land-use changes, *Atmos. Chem. Phys.*, 14(9), 4587–  
1139 4605, 2014.

1140 Stavroukou, T., Müller, J.-F., Bauwens, M., De Smedt, I., Van Roozendael, M., De Mazière, M., Vigouroux, C.,  
1141 Hendrick, F., George, M., Clerbaux, C., Coheur, P.-F., and Guenther, A.: How consistent are top-down hydrocarbon  
1142 emissions based on formaldehyde observations from GOME-2 and OMI?, *Atmos. Chem. Phys.*, 15, 11861–11884,  
1143 <https://doi.org/10.5194/acp-15-11861-2015>, 2015.

1144 Stavrakou, T., Müller, J.-F., Bauwens, M., De Smedt, I., Lerot, C., Van Roozendael, M., Coheur, P.-F., Clerbaux, C.,  
1145 Boersma, K. F., van der A, R. and Song, Y.: Substantial Underestimation of Post-Harvest Burning Emissions in the  
1146 North China Plain Revealed by Multi-Species Space Observations, *Sci. Rep.*, 6(1), 32307, doi:10.1038/srep32307,  
1147 2016.

1148 Stavrakou, T., Müller, J.-F., Bauwens, M., De Smedt, I., Van Roozendael, M. and Guenther, A.: Impact of Short-Term  
1149 Climate Variability on Volatile Organic Compounds Emissions Assessed Using OMI Satellite Formaldehyde  
1150 Observations, *Geophys. Res. Lett.*, 45(16), 8681–8689, 2018.

1151 Su, W., Liu, C., Hu, Q., Zhao, S., Sun, Y., Wang, W., Zhu, Y., Liu, J., and Kim, J.: Primary and secondary sources of  
1152 ambient formaldehyde in the Yangtze River Delta based on Ozone Mapping and Profiler Suite (OMPS) observations,  
1153 *Atmos. Chem. Phys.*, 19, 6717–6736, <https://doi.org/10.5194/acp-19-6717-2019>, 2019.

1154 Su, W., Liu, C., Chan, K. L., Hu, Q., Liu, H., Ji, X., Zhu, Y., Liu, T., Zhang, C., Chen, Y., and Liu, J.: An improved  
1155 TROPOMI tropospheric HCHO retrieval over China, *Atmos. Meas. Tech.*, 13, 6271–6292,  
1156 <https://doi.org/10.5194/amt-13-6271-2020>, 2020.

1157 Sun, W., Zhu, L., De Smedt, I., Bai, B., Pu, D., Chen, Y., et al.: Global significant changes in formaldehyde (HCHO)  
1158 columns observed from space at the early stage of the COVID-19 pandemic. *Geophysical Research Letters*, 48,  
1159 e2020GL091265. <https://doi.org/10.1029/2020GL091265>, 2021.

1160 Surl, L., Palmer, P. I., and González Abad, G.: Which processes drive observed variations of HCHO columns over  
1161 India?, *Atmos. Chem. Phys.*, 18, 4549–4566, <https://doi.org/10.5194/acp-18-4549-2018>, 2018.

1162 Theys, N., De Smedt, I., van Gent, J., Danckaert, T., Wang, T., Hendrick, F., Stavrakou, T., Bauduin, S., Clarisse, L.,  
1163 Li, C., Krotkov, N., Yu, H., Brenot, H. and Van Roozendael, M.: Sulfur dioxide vertical column DOAS retrievals  
1164 from the Ozone Monitoring Instrument: Global observations and comparison to ground-based and satellite data, *J.*  
1165 *Geophys. Res. Atmos.*, 120(6), 2014JD022657, doi:10.1002/2014JD022657, 2015.

1166 Theys, N., Volkamer, R., Müller, J. F., Zarzana, K. J., Kille, N., Clarisse, L., De Smedt, I., Lerot, C., Finkenzeller, H.,  
1167 Hendrick, F., Koenig, T. K., Lee, C. F., Knote, C., Yu, H. and Van Roozendael, M.: Global nitrous acid emissions and  
1168 levels of regional oxidants enhanced by wildfires, *Nat. Geosci.*, 13(10), 681–686, doi:10.1038/s41561-020-0637-7,  
1169 2020.

1170 Tirpitz, J.-L., Frieß, U., Hendrick, F., Alberti, C., Allaart, M., Apituley, A., Bais, A., Beirle, S., Berkhout, S., Bognar,  
1171 K., Bösch, T., Bruchkouski, I., Cede, A., Chan, K. L., den Hoed, M., Donner, S., Drosoglou, T., Fayt, C., Friedrich,  
1172 M. M., Frumau, A., Gast, L., Gielen, C., Gomez-Martín, L., Hao, N., Hensen, A., Henzing, B., Hermans, C., Jin, J.,  
1173 Kreher, K., Kuhn, J., Lampel, J., Li, A., Liu, C., Liu, H., Ma, J., Merlaud, A., Peters, E., Pinardi, G., Piders, A., Platt,  
1174 U., Puentedura, O., Richter, A., Schmitt, S., Spinei, E., Stein Zweers, D., Strong, K., Swart, D., Tack, F., Tiefengraber,  
1175 M., van der Hoff, R., van Roozendael, M., Vlemmix, T., Vonk, J., Wagner, T., Wang, Y., Wang, Z., Wenig, M.,  
1176 Wiegner, M., Wittrock, F., Xie, P., Xing, C., Xu, J., Yela, M., Zhang, C., and Zhao, X.: Intercomparison of MAX-  
1177 DOAS vertical profile retrieval algorithms: studies on field data from the CINDI-2 campaign, *Atmos. Meas. Tech.*,  
1178 14, 1–35, <https://doi.org/10.5194/amt-14-1-2021>, 2021.

1179 van Geffen, J., Boersma, K. F., Eskes, H., Sneep, M., ter Linden, M., Zara, M., and Veefkind, J. P.: S5P TROPOMI  
1180 NO<sub>2</sub> slant column retrieval: method, stability, uncertainties and comparisons with OMI, *Atmos. Meas. Tech.*, 13,  
1181 1315–1335, <https://doi.org/10.5194/amt-13-1315-2020>, 2020.

1182 Veefkind, J. P., Aben, I., McMullan, K., Förster, H., de Vries, J., Otter, G., Claas, J., Eskes, H. J., de Haan, J. F.,  
1183 Kleipool, Q., van Weele, M., et al.: TROPOMI on the ESA Sentinel-5 Precursor: A GMES mission for global  
1184 observations of the atmospheric composition for climate, air quality and ozone layer applications, *Remote Sensing of*  
1185 *Environment*, 120(0), 70-83, 2012.

1186 Veefkind, J. P., de Haan, J. F., Sneep, M., and Levelt, P. F.: Improvements to the OMI O<sub>2</sub>–O<sub>2</sub> operational cloud  
1187 algorithm and comparisons with ground-based radar–lidar observations, *Atmos. Meas. Tech.*, 9, 6035-6049,  
1188 <https://doi.org/10.5194/amt-9-6035-2016>, 2016.

1189 Verhoelst, T., Compernolle, S., Pinardi, G., Lambert, J.-C., Eskes, H. J., Eichmann, K.-U., Fjæraa, A. M., Granville,  
1190 J., Niemeijer, S., Cede, A., Tiefengraber, M., Hendrick, F., Pazmiño, A., Bais, A., Bazureau, A., Boersma, K. F.,  
1191 Bogner, K., Dehn, A., Donner, S., Elokhov, A., Gebetsberger, M., Goutail, F., Grutter de la Mora, M., Gruzdev, A.,  
1192 Gratsea, M., Hansen, G. H., Irie, H., Jepsen, N., Kanaya, Y., Karagkiozidis, D., Kivi, R., Kreher, K., Levelt, P. F.,  
1193 Liu, C., Müller, M., Navarro Comas, M., PETERS, A. J. M., Pommereau, J.-P., Portafaix, T., Prados-Roman, C.,  
1194 Puentedura, O., Querel, R., Remmers, J., Richter, A., Rimmer, J., Rivera Cárdenas, C., Saavedra de Miguel, L.,  
1195 Sinyakov, V. P., Stremme, W., Strong, K., Van Roozendaal, M., Veefkind, J. P., Wagner, T., Wittrock, F., Yela  
1196 González, M., and Zehner, C.: Ground-based validation of the Copernicus Sentinel-5P TROPOMI NO<sub>2</sub> measurements  
1197 with the NDACC ZSL-DOAS, MAX-DOAS and Pandonia global networks, *Atmos. Meas. Tech.*, 14, 481–510,  
1198 <https://doi.org/10.5194/amt-14-481-2021>, 2021.

1199 Vigouroux, C., Hendrick, F., Stavrakou, T., Dils, B., De Smedt, I., Hermans, C., Merlaud, A., Scolas, F., Senten, C.,  
1200 Vanhaelewyn, G., Fally, S., Carleer, M., Metzger, J.-M., Müller, J.-F., Van Roozendaal, M., and De Mazière, M.:  
1201 Ground-based FTIR and MAX-DOAS observations of formaldehyde at Réunion Island and comparisons with satellite  
1202 and model data, *Atmos. Chem. Phys.*, 9, 9523-9544, doi:10.5194/acp-9-9523-2009, 2009.

1203 Vigouroux, C., Bauer Aquino, C. A., Bauwens, M., Becker, C., Blumenstock, T., De Mazière, M., García, O., Grutter,  
1204 M., Guarin, C., Hannigan, J., Hase, F., Jones, N., Kivi, R., Koshelev, D., Langerock, B., Lutsch, E., Makarova, M.,  
1205 Metzger, J.-M., Müller, J.-F., Notholt, J., Ortega, I., Palm, M., Paton-Walsh, C., Poberovskii, A., Rettinger, M.,  
1206 Robinson, J., Smale, D., Stavrakou, T., Stremme, W., Strong, K., Sussmann, R., Té, Y., and Toon, G.: NDACC  
1207 harmonized formaldehyde time series from 21 FTIR stations covering a wide range of column abundances, *Atmos.*  
1208 *Meas. Tech.*, 11, 5049–5073, <https://doi.org/10.5194/amt-11-5049-2018>, 2018.

1209 Vigouroux, C., Langerock, B., Bauer Aquino, C. A., Blumenstock, T., Cheng, Z., De Mazière, M., De Smedt, I.,  
1210 Grutter, M., Hannigan, J. W., Jones, N., Kivi, R., Loyola, D., Lutsch, E., Mahieu, E., Makarova, M., Metzger, J.-M.,  
1211 Morino, I., Murata, I., Nagahama, T., Notholt, J., Ortega, I., Palm, M., Pinardi, G., Röhling, A., Smale, D., Stremme,  
1212 W., Strong, K., Sussmann, R., Té, Y., van Roozendaal, M., Wang, P., and Winkler, H.: TROPOMI–Sentinel-5

1213 Precursor formaldehyde validation using an extensive network of ground-based Fourier-transform infrared stations,  
1214 *Atmos. Meas. Tech.*, 13, 3751–3767, <https://doi.org/10.5194/amt-13-3751-2020>, 2020.

1215 Vlemmix, T., Piters, A., Stammes, P., Wang, P. and Levelt, P. F.: Retrieval of tropospheric NO<sub>2</sub> using the MAX-  
1216 DOAS method combined with relative intensity measurements for aerosol correction, *Atmos. Meas. Tech.*, 3(5),  
1217 1287–1305, doi:10.5194/amt-3-1287-2010, 2010.

1218 Vlemmix, T., Hendrick, F., Pinardi, G., Smedt, I. De, Fayt, C., Hermans, C., Piters, A., Wang, P. and Levelt, P.: MAX-  
1219 DOAS observations of aerosols, formaldehyde and nitrogen dioxide in the Beijing area: comparison of two profile  
1220 retrieval, *Atmos. Meas. Tech.*, (2), 941–963, doi:10.5194/amt-8-941-2015, 2015.

1221 Vrekoussis, M., Wittrock, F., Richter, A. and Burrows, J. P.: GOME-2 observations of oxygenated VOCs: what can  
1222 we learn from the ratio glyoxal to formaldehyde on a global scale?, *Atmos. Chem. Phys.*, 10(21), 10145-10160, 2010.

1223 Wagner, T., Dix, B., Friedeburg, C. Von, Friess, U., Sanghavi, S., Sinreich, R. and Platt, U.: MAX-DOAS O<sub>4</sub>  
1224 measurements: a new technique to derive information on atmospheric aerosols - Principles and information content,  
1225 *J. Geophys. Res.*, 109(D22205), 2004.

1226 Wagner, T., Beirle, S., Brauers, T., Deutschmann, T., Frieß, U., Hak, C., Halla, J. D., Heue, K. P., Junkermann, W.,  
1227 Li, X., Platt, U., and Pundt-Gruber, I.: Inversion of tropospheric profiles of aerosol extinction and HCHO and NO<sub>2</sub>  
1228 mixing ratios from MAX-DOAS observations in Milano during the summer of 2003 and comparison with independent  
1229 data sets, *Atmos. Meas. Tech.*, 4, 2685-2715, doi:10.5194/amt-4-2685-2011, 2011.

1230 Wang, Y., Beirle, S., Hendrick, F., Hilboll, A., Jin, J., Kyuberis, A. A., Lampel, J., Li, A., Luo, Y., Lodi, L., Ma, J.,  
1231 Navarro, M., Ortega, I., Peters, E., Polyansky, O. L., Remmers, J., Richter, A., Puentedura, O., Van Roozendaal, M.,  
1232 Seyler, A., Tennyson, J., Volkamer, R., Xie, P., Zobov, N. F., and Wagner, T.: MAX-DOAS measurements of HONO  
1233 slant column densities during the MAD-CAT campaign: inter-comparison, sensitivity studies on spectral analysis  
1234 settings, and error budget, *Atmos. Meas. Tech.*, 10, 3719–3742, <https://doi.org/10.5194/amt-10-3719-2017>, 2017.

1235 Wang, Y., Dörner, S., Donner, S., Böhnke, S., Smedt, I. De, Dickerson, R. R., Dong, Z., He, H., Li, Z., Li, Z. and  
1236 others: Vertical profiles of NO<sub>2</sub>, SO<sub>2</sub>, HONO, HCHO, CHOCHO and aerosols derived from MAX-DOAS  
1237 measurements at a rural site in the central western North China Plain and their relation to emission sources and effects  
1238 of regional transport, *Atmos. Chem. Phys.*, 19(8), 5417–5449, 2019a.

1239 Wang, Y., Wang, Z., Yu, C., Zhu, S., Cheng, L., Zhang, Y. and Chen, L.: Validation of OMI HCHO Products Using  
1240 MAX-DOAS observations from 2010 to 2016 in Xianghe, Beijing: Investigation of the Effects of Aerosols on Satellite  
1241 Products, *Remote Sens.*, 11(2), 203, doi:10.3390/rs11020203, 2019b.

1242 Wells, K. C., Millet, D. B., Payne, V. H., Deventer, M. J., Bates, K. H., Gouw, J. A., Graus, M., Warneke, C.,  
1243 Wisthaler, A. and Fuentes, J. D.: Satellite isoprene retrievals constrain emissions and atmospheric oxidation, *Nature*,  
1244 585(August 2019), doi:10.1038/s41586-020-2664-3, 2020.

1245 Williams, J. E., Boersma, K. F., Le Sager, P., and Verstraeten, W. W.: The high-resolution version of TM5-MP for  
1246 optimized satellite retrievals: description and validation, *Geosci. Model Dev.*, 10, 721–750,  
1247 <https://doi.org/10.5194/gmd-10-721-2017>, 2017.

1248 Wittrock, F., Oetjen, H., Richter, A., Fietkau, S., Medeke, T., Rozanov, A., and Burrows, J.P.: MAX-DOAS  
1249 measurements of atmospheric trace gases in Ny-Alesund – Radiative transfer studies and their application, *Atmos.*  
1250 *Chem. Phys.*, 4, 955–966, doi:10.5194/acp-4-955-2004, 2004.

1251 Wittrock, F., Richter, A., Oetjen, H., Burrows, J. P., Kanakidou, M., Myriokefalitakis, S., Volkamer, R., Beirle, S.,  
1252 Platt, U. and Wagner, T.: Simultaneous global observations of glyoxal and formaldehyde from space, *Geophysical*  
1253 *Research Letters*, 33(16), 1-5, doi:10.1029/2006GL026310, 2006.

1254 Zara, M., Boersma, K. F., De Smedt, I., Richter, A., Peters, E., van Geffen, J. H. G. M., Beirle, S., Wagner, T., Van  
1255 Roozendaal, M., Marchenko, S., Lamsal, L. N., and Eskes, H. J.: Improved slant column density retrieval of nitrogen  
1256 dioxide and formaldehyde for OMI and GOME-2A from QA4ECV: intercomparison, uncertainty characterisation,  
1257 and trends, *Atmos. Meas. Tech.*, 11, 4033–4058, <https://doi.org/10.5194/amt-11-4033-2018>, 2018.

1258 Zhu, L., Jacob, D. J., Kim, P. S., Fisher, J. A., Yu, K., Travis, K. R., Mickleby, L. J., Yantosca, R. M., Sulprizio, M. P.,  
1259 De Smedt, I., González Abad, G., Chance, K., Li, C., Ferrare, R., Fried, A., Hair, J. W., Hanisco, T. F., Richter, D.,  
1260 Jo Scarino, A., Walega, J., Weibring, P., and Wolfe, G. M.: Observing atmospheric formaldehyde (HCHO) from  
1261 space: validation and intercomparison of six retrievals from four satellites (OMI, GOME2A, GOME2B, OMPS) with  
1262 SEAC4RS aircraft observations over the southeast US, *Atmos. Chem. Phys.*, 16, 13477–13490,  
1263 <https://doi.org/10.5194/acp-16-13477-2016>, 2016.

1264 Zhu, L., González Abad, G., Nowlan, C. R., Chan Miller, C., Chance, K., Apel, E. C., DiGangi, J. P., Fried, A.,  
1265 Hanisco, T. F., Hornbrook, R. S., Hu, L., Kaiser, J., Keutsch, F. N., Permar, W., St. Clair, J. M., and Wolfe, G. M.:  
1266 Validation of satellite formaldehyde (HCHO) retrievals using observations from 12 aircraft campaigns, *Atmos. Chem.*  
1267 *Phys.*, 20, 12329–12345, <https://doi.org/10.5194/acp-20-12329-2020>, 2020.

1268 Zyrichidou, I., Balis, D., Koukouli, M. E., Drosoglou, T., Bais, A., Gratsea, M., Gerasopoulos, E., Liora, N., Poupkou,  
1269 A., Giannaros, C. and others: Adverse results of the economic crisis: A study on the emergence of enhanced  
1270 formaldehyde (HCHO) levels seen from satellites over Greek urban sites, *Atmos. Res.*, 224, 42–51, 2019.